Dissertation

submitted to the
Combined Faculties for the Natural Sciences and for Mathematics
of the Ruperto-Carola University of Heidelberg, Germany
for the degree of
Doctor of Natural Sciences

presented by

Diplom-Physicist Nadine Neumayer, née Häring
born in Spaichingen, Germany

Oral examination: February 7, 2007

The nucleus of Centaurus A

Referees: Prof. Dr. Hans-Walter Rix
Prof. Dr. Max Camenzind

Abstract

At less than 4 Mpc away, Centaurus A (NGC 5128) is the nearest massive elliptical galaxy, the nearest radio galaxy, and the nearest recent merger. It is the ideal laboratory to study the connection between merging, massive black holes, the source of radio jets, and merger-induced star formation in detail.

Using Naos-Conica and SINFONI at the ESO Very Large Telescope (VLT), we obtained adaptive optics (AO) assisted data at unprecedented spatial resolution. We demonstrate that thorough kinematical modelling of AO data is feasible and leads to an accurate measurement of the black hole mass. We find that depending on their ionisation level, different gas species display different flux distributions and velocity structures. In this respect, integral-field-unit data are crucial to identify non-gravitational gas motions.

The H_2 gas kinematics inside the central $r \lesssim 1\farcs5$ of the active galactic nucleus are successfully described by a (warped) gas disk, rotating in the joint gravitational potential of the stars and a black hole of $M_{BH} \sim 7 \times 10^7 M_\odot$. With our revised M_{BH} estimate, that is a factor ~ 3 lower than previous measurements, Cen A is no longer a dramatic outlier in the $M_{BH} - \sigma$ relation.

Near-infrared images in JHK reveal marginally resolved stellar clusters, comparable in their properties to young starburst clusters found close to the Galactic Centre.

Kurzfassung

Mit einer Entfernung von weniger als 4 Mpc ist Centaurus A (NGC 5128) die nächste grosse elliptische Galaxie, die nächste Radiogalaxie, sowie die nächste verschmelzende Galaxie. Sie stellt eine ideale Umgebung dar, um im Detail zu untersuchen, wie Galaxienverschmelzung, massereiche Schwarze Löcher, die Quelle von Radio Jets und die durch Galaxienwechselwirkung ausgelöste Sternentstehung zusammenhängen.

Mit Naos-Conica und SINFONI am ESO Very Large Telescope (VLT) haben wir mit Hilfe von Adaptiver Optik (AO) Beobachtungsdaten von unübertroffener räumlicher Auflösung erhalten. Wir zeigen, dass sorgfältige kinematische Modellierung von AO Daten durchführbar ist und eine genaue Messung der Masse des Schwarzen Loches ermöglicht.

Unsere Beobachtungen zeigen, daß verschiedene Gasarten in Abhängigkeit ihrer Ionisationsenergie unterschiedliche Flußverteilungen und Geschwindigkeitsstrukturen zeigen. In diesem Zusammenhang ist es wichtig, Daten mit Hilfe abbildender Spektroskopie zu gewinnen, um nicht-gravitative Bewegungen des Gases aufzuspüren.

Die Bewegung des H_2 Gases in der zentralen Umgebung ($r \lesssim 1\farcs5$) um den Aktiven Galaktischen Kern wird erfolgreich durch ein (verzerrtes) Scheibenmodell beschrieben. Dieses rotiert im Gesamtschwerefeld der Sterne und des Schwarzen Loches, welches eine Masse von $M_{BH} \sim 7 \times 10^7 M_\odot$ hat. Dieser neu bestimmte Wert für M_{BH} ist um einen Faktor ~ 3 kleiner als vorherige Messwerte und bringt Cen A mit der bekannten $M_{BH} - \sigma$ Beziehung in Einklang.

Nahinfrarot Aufnahmen in JHK zeigen Sternhaufen, die knapp räumlich aufgelöst sind und deren Eigenschaften mit denen von jungen Sternhaufen übereinstimmen, die nahe am Galaktischen Zentrum gefunden wurden.

Meiner Familie

Contents

1. Introduction

One of the drivers of current astrophysical research is understanding the birth and evolution of galaxies and it is becoming increasingly clear that the central supermassive black hole plays a major role in the evolution of its host galaxy.

1.1 Galaxies and black holes

During the last few years it has been realised that most, if not all, nearby luminous galaxies host a supermassive black hole (BH) in their nuclei with masses in the $10^6 - 10^{10} M_{\odot}$ range (e.g. Ferrarese and Ford, 2005, and references therein). The black hole mass ($\mathrm{M_{BH}}$) is tightly related with mass or luminosity of the host stellar spheroid, bulge, (e.g. Kormendy and Richstone 1995; Marconi et al. 2003; Häring and Rix 2004, see Figure 1.1) and with the stellar velocity dispersion, σ, (Ferrarese and Merritt, 2000; Gebhardt et al., 2000). These correlations have an amazingly low scatter, perhaps surprisingly low, since the quantities $\mathrm{M_{BH}}$ and $\mathrm{M_{bulge}}/\sigma$ probe very different scales. These facts indicate that the formation of a massive BH is an essential ingredient in the process of galaxy formation.

The concept of supermassive black holes at the centres of galaxies was first introduced to explain the phenomenon of active galactic nuclei (AGN) (see Hoyle and Fowler, 1963; Lynden-Bell, 1969; Rees, 1977, and Chapter 2). Black holes are found ubiquitous in both active and non-active galaxy centres in the near universe. Quiescent black holes are relics of past AGN activity (Yu and Tremaine, 2002; Marconi et al., 2004), and it is being realised that an accreting supermassive BH may have a major impact on the star formation rate in the host galaxy: the feedback from the AGN is believed to be responsible for setting the close relations between BH and host galaxy properties (e.g. Menci et al., 2003; Granato et al., 2004; Di Matteo et al., 2005).

Black holes are detected and their masses directly measured in nearby galaxies using gas or stars as tracers of the kinematics in the nuclear region. The gas kinematical method has the advantage of being relatively simple, of requiring relatively short observation times and being applicable to AGN. However, non-gravitational or non-circular motions might bias or completely invalidate the method. Moreover, detectable emission lines are not always present in galactic nuclei.

The stellar dynamical method has the advantage that star motions are always gravitational and that stars are present in all galactic nuclei. However, long observation

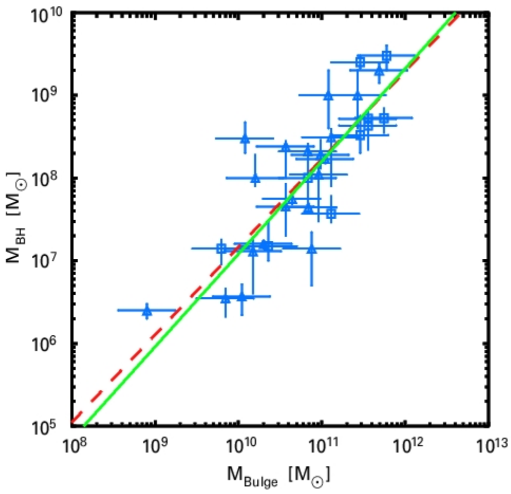

Figure 1.1 Relation between the stellar bulge mass (M_{Bulge}) and the mass of the central black hole (M_{BH}) (from Häring & Rix, 2004). With accurate black hole masses, this relation is as tight as the $M_{BH} - \sigma$ relation.

times are required to obtain high quality observations and stellar dynamical models are very complex leading to potential indeterminacy (e.g. Valluri et al., 2004).

The weakest points of both methods – assumption of circular gravitational motions for gas kinematics, complexity of modelling for stellar dynamics – have shed some doubts on the reliability of M_{BH} estimates (e.g. Tremaine et al., 2002; Cappellari, 2002; Verdoes Kleijn et al., 2002; Valluri et al., 2004; Cretton and Emsellem, 2004). This is a very important issue because the correlations between BH mass and host galaxy properties, which are based mostly on M_{BH} from gas kinematic and stellar dynamics, are pivotal in understanding the co-evolution of galaxies and black holes over cosmic time. It is therefore crucial to test these methods and compare the modelling results from gas and stellar kinematics, for the objects where both are available. Up to now this was only possible in very few cases, as e.g. for IC 1459, where Verdoes Kleijn et al. (2000) and Cappellari (2002) find that the M_{BH} value derived from gas kinematics is almost a factor of 10 lower than measured from stellar kinematics. However in IC 1459 the rotation curve of the gas is not consistent with that of a rotating disk and the M_{BH} measurement cannot be considered reliable. For NGC 3379 Shapiro et al. (2006) find a good agreement between the M_{BH} measurements from gas and stellar kinematics.

The reliability of M_{BH} measurements depends strongly on the spatial resolution of the kinematical measurements. An important quantity in this context is the 'radius of influence' of the black hole, $r_{BH} = GM_{BH}/\sigma^2$, which gives the radius of a sphere where the mass of the central black hole equals the mass of the enclosed stars. Inside this sphere of influence, the dynamics of gas and stars will be dominated by the gravitational influence of the black hole. For larger radii, the (cumulative) mass of the stars will eventually dominate the overall gravitational potential. Dynamical M_{BH} measurements can only be considered reliable if the sphere of influence is well resolved.

1.2 Centaurus A

Centaurus A (NGC 5128) is the closest massive elliptical galaxy (see Figure 1.2). It is the closest galaxy harbouring an active galactic nucleus (AGN). Its central source is powerful in radio and its AGN activity is revealed by the presence of a radio and X-ray jet (see e.g. Israel, 1998; Tingay et al., 1998; Hardcastle et al., 2003). Figure 1.3 shows a composite image of optical, radio, and x-ray images of Centaurus A (Cen A).

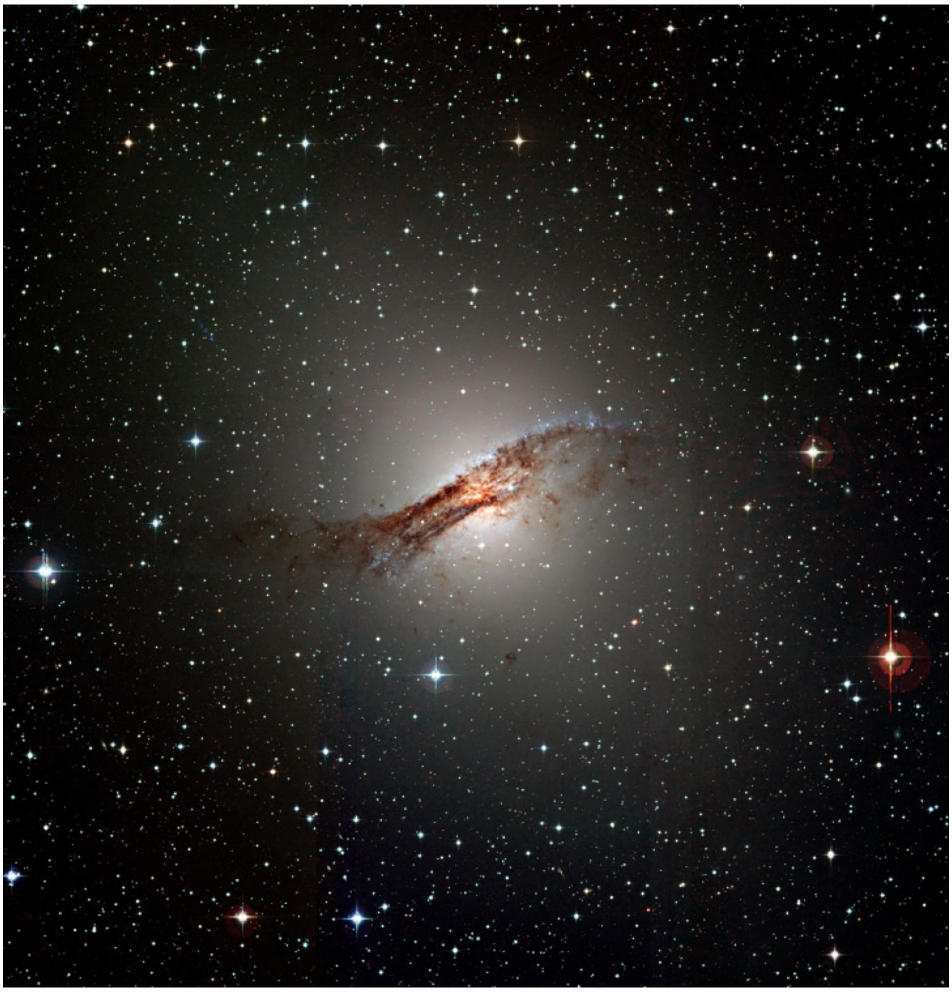

Figure 1.2 Image of NGC 5128 observed with the Wide Field Imager (WFI) on La Silla, Chile. The prominent dust lane, crossing the giant elliptical galaxy, is clearly visible. The whole galaxy is $\sim 15'$ across. In all figures, north is up and east is to the left.

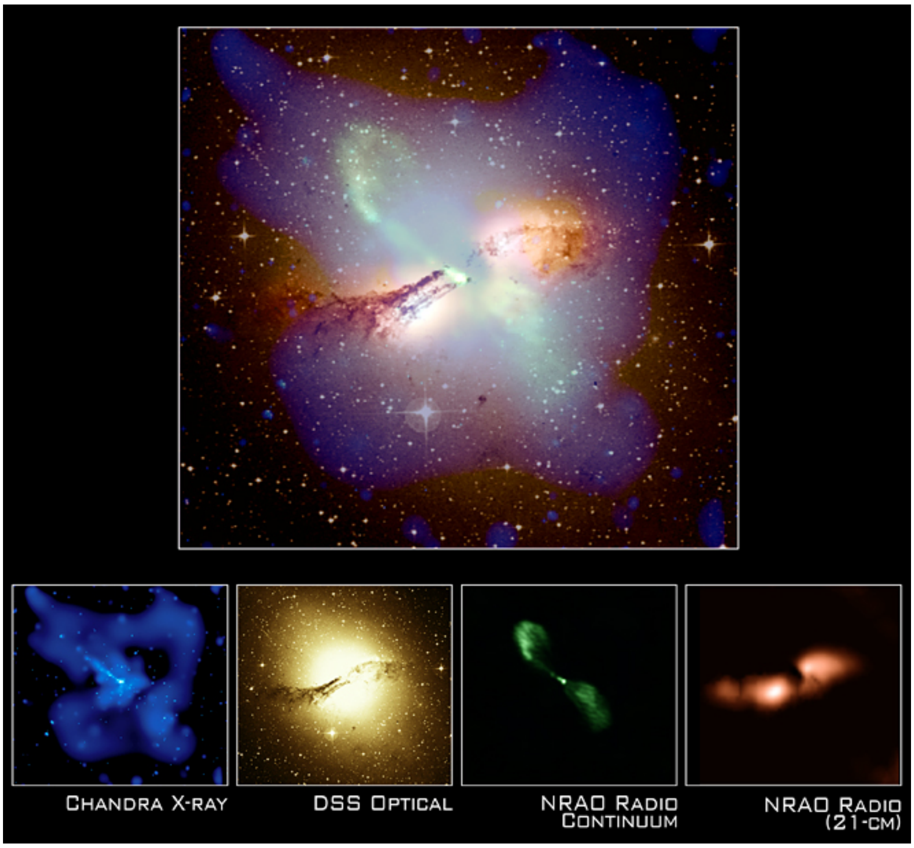

Figure 1.3 Composite image (top panel) of optical, radio, and x-ray images of Centaurus A. The scales of the images are about $18' \times 17'$. Credit:X-ray (NASA/CXC/M. Karovska et al.), Radio 21-cm image (NRAO/VLA/J.Van Gorkom/Schminovich et al.), Radio continuum image (NRAO/VLA/J. Condon et al.), Optical (Digitized Sky Survey U.K. Schmidt Image/STScI)

The most striking feature of Cen A is the dust lane (see Figure. 1.2), rich in molecular and ionised gas (Quillen et al., 1992, 1993, 2006; Mirabel et al., 1999; Leeuw et al., 2002; Karovska et al., 2003), which crosses the whole galaxy hiding the nuclear region under at least 7 mag of extinction in V (Schreier et al., 1996; Marconi et al., 2000, and chapter 6 of this thesis). The unusual morphology of Cen A was first ascribed to a significant and recent merger event by Baade and Minkowski (1954). This merger hypothesis is well supported by the existence of optical and H I shells at large radii (see Figure 1.4 and Malin et al., 1983; Peng et al., 2002), that allow to date the merger to a few times 10^8 years ago (Quillen et al., 1993; Peng et al., 2002). The recent merger and central AGN activity are likely associated with each other and make Cen A an important object for our understanding of central black holes, galaxy mergers, AGN activity, and the relationships among these components of galaxy evolution.

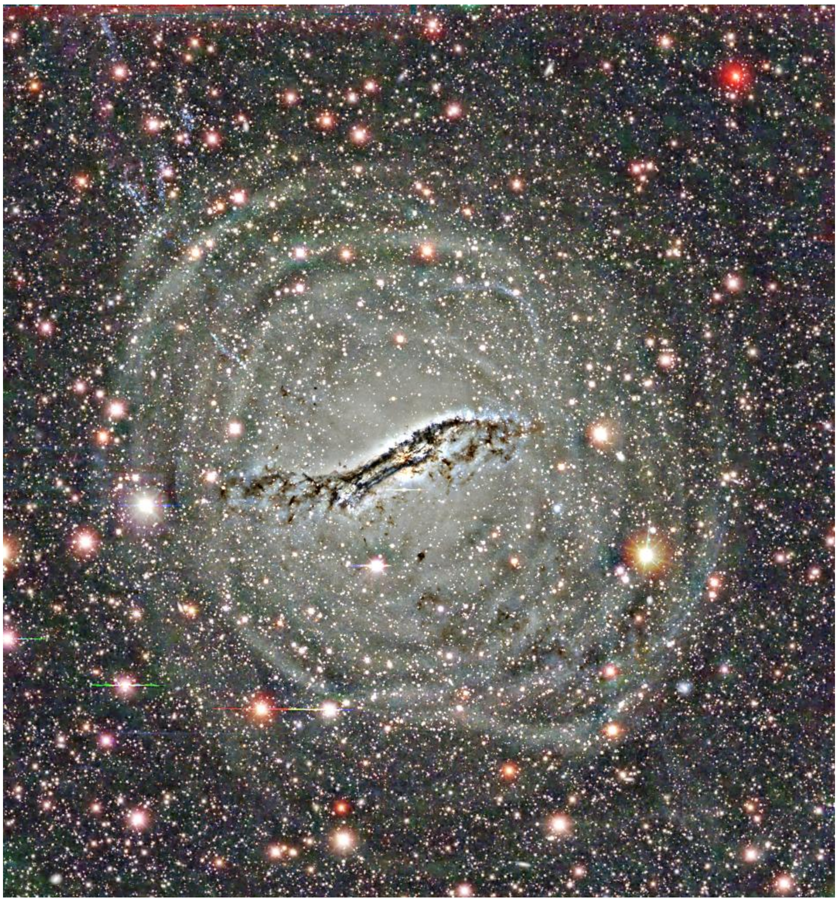

Figure 1.4 Very deep BVR colour image of NGC 5128 taken at the Cerro Tololo Inter-American Observatory (CTIO) (Peng et al., 2002). The complex system of shells, presumably caused by the merger event, is clearly visible.

Cen A's proximity makes it an attractive target, as spatial resolution on the sky translates to small physical scales in the galaxy itself. However, the precise distance to NGC 5128 is a matter of some debate. Israel (1998) compiles and summarises results from globular cluster and planetary nebulae counts, globular cluster surface brightness fluctuations, and Hubble Space Telescope (HST) observations of halo red giant branch stars, he finds good agreement between these sources with a distance of D= 3.4 ± 0.15 Mpc. More recently, the I-band surface brightness fluctuation study of the galaxy itself by Tonry et al. (2001) found D= 4.2 ± 0.3 Mpc. Rejkuba (2004) measured the Mira period-luminosity relation and the luminosity of the tip of the red giant branch to find D= 3.84 ± 0.35 Mpc. Throughout this thesis we will assume D= 3.5 Mpc, to be consistent with previous M_{BH} studies. At this distance, 1" on the sky corresponds to 17 pc.

Peering through the foreground dust by observing in the near-infrared, Schreier et al. (1998) found evidence for a disk-like feature in ionised gas from Paα HST images. Marconi et al. (2001) used near-infrared spectroscopy (at seeing limited resolution of $0\farcs5$) to perform a gas kinematical analysis of such feature finding evidence for a black hole with $\mathrm{M_{BH}} = 2^{+3.0}_{-1.4} 10^8 M_\odot$. The large error associated with $\mathrm{M_{BH}}$ takes into account the degeneracy due to the unknown inclination angle of the gas disk for which Marconi et al. (2001) could only assume $\mathrm{i} > 15^\circ$.

Given a velocity dispersion for Cen A of $\sim$150 km/s, we would expect a BH mass around $3 \times 10^7 \mathrm{M_\odot}$ from the $\mathrm{M_{BH}} - \sigma$ relation. Therefore, this particular $\mathrm{M_{BH}}$ estimate puts Cen A almost a factor 7 above the $\mathrm{M_{BH}} - \sigma$ relation, making it the strongest outlier to this relation. The recent stellar dynamical measurement of Silge et al. (2005) confirmed a fairly high value of $\mathrm{M_{BH}} = 1.8^{+0.9}_{-0.5} 10^8 M_\odot$. These black hole measurements were both conducted using ground-based seeing limited observations and as such, might not be able to disentangle the influence of the black hole and the stars on the overall potential. If we take the $\mathrm{M_{BH}}$ value predicted by the $\mathrm{M_{BH}} - \sigma$ relation, and calculate the radius of influence, it is as low as $0\farcs3$, not resolved in the previous studies.

In order to clarify, whether Cen A is inevitably an outlier to the $\mathrm{M_{BH}} - \sigma$ relation, or whether previous measurements overestimated the black hole mass due to insufficient spatial resolution, we perform a detailed dynamical study of the nucleus of the closest elliptical galaxy, drawing on adaptive optics observations.

Our unique data set obtained with the state-of-the-art instruments Naos-Conica and SINFONI at the ESO very large telescope, enable us to get an accurate measure of Cen A's black hole mass, and study at unprecedented spatial resolution the gas kinematics in the central 3" $\times$ 3" of the closest AGN. We witness interaction of the jet with the surrounding gas on scales of $\lesssim$ 1" from the AGN. Our Naos-Conica images give valuable information on the nuclear star formation and hint towards jet induced star formation on scales of $<$ 200 pc.

This thesis is outlined as follows: Chapter 2 gives a very brief introduction to active galactic nuclei and the current unification scheme. The application of adaptive optics observations to AGN is presented in Chapter 3, while Chapter 4 presents the analysis and dynamical modelling of our Naos-Conica data. In Chapter 5, SINFONI data are presented to study the gas morphology and kinematics of different emission line species for the central 3" $\times$ 3" around the AGN. A detailed dynamical model is constructed to explain the kinematics of molecular hydrogen, from that the black hole mass is deduced.
The circum-nuclear star formation is studied in Chapter 6 via the analysis of our NACO imaging data. Finally, Chapter 7 summarises the main results of the thesis, and Chapter 8 provides an outlook to future work.

2. Active Galactic Nuclei

This chapter is meant as a brief introductory chapter to the concepts of active galactic nuclei that are relevant to this thesis. The interested reader is referred to the book by Robson (1996) for an introduction to the subject, and the book of Osterbrock and Ferland (2006) for a more quantitative discussion. In the following, the term AGN will be used as an abbreviation to both 'active galactic nucleus' and 'active galactic nuclei'.

2.1 The phenomenon of active galactic nuclei

The expression active galactic nuclei (AGN) comes from the observational fact that these types of galaxy centres exhibit special emission line features and very high luminosities concentrated in very small regions. The luminosity of AGN are in the range $10^5 - 10^{13} L_\odot$ and therefore may even outshine the entire galaxy where they reside - the so-called 'host galaxy'. The AGN usually emits radiation over the entire electromagnetic spectrum, ranging from radio to X-ray or even γ-rays. A fair fraction of AGN host galaxies contain radio and sometimes even X-ray jets.

The first galaxies with AGN were identified as an 'unusual class of objects' already in 1943, when Carl Seyfert analysed the spectra of 'extragalactic nebulae' that show strong, fairly broad, high-excitation emission lines localised in their nuclei (Seyfert, 1943). His seminal work gave the name to this type of objects, called **Seyfert galaxies**. There are two type of Seyfert (Sy) galaxies (introduced by Khachikian and Weedman, 1974). The spectra of type 2 Seyfert(Sy2) galaxies contain both permitted and forbidden[1] lines that appear Doppler broadened by velocities of ~ 500 km/s. The spectra of type 1 Seyfert (Sy1) galaxies show very broad line wings of up to $1000 - 5000$ km/s in their permitted lines, while the forbidden lines are of similar width to the lines seen in Sy2 galaxies. Figure 2.1 shows a compilation of spectra for different types of the AGN phenomenon. On the upper right there is an example for a Sy1 and a Sy2 nuclear spectrum. About

---

[1] 'forbidden' means that they have a very small value of transition probability. Under laboratory conditions, the density would be so high that the lines are collisionally de-excited, before they decay radiatively.

one third of all Seyferts are of type 2. Seyferts of both types show strong variable X-ray emission and emit strongly in the infrared (Binney and Merrifield, 1998).

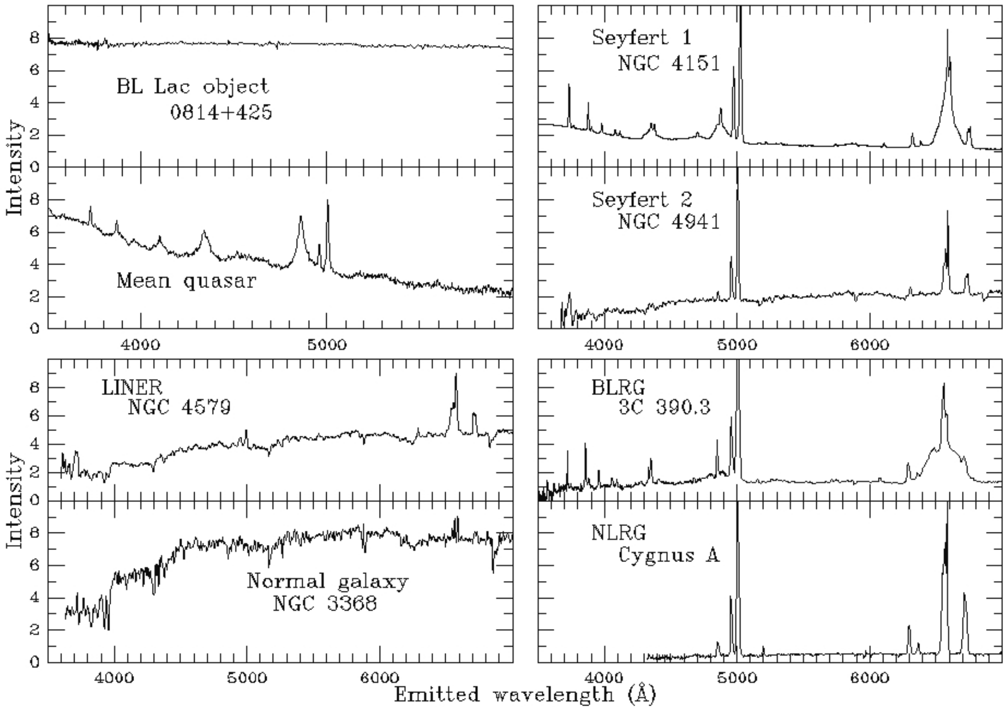

Figure 2.1 Selection of optical spectra of prototypes of seven different types of AGN plus a normal galaxy spectrum for comparison. The spectra have all been shifted to their emitted wavelength scales for ease of comparison. (Compiled by W. Keel)

Many galaxies have nuclei that resemble those of type 2 Seyferts except that their forbidden lines tend to arise in less highly ionised atoms. These **low-ionisation nuclear emission-line regions**, or **LINERs**, were originally treated as a distinct phenomenon, but they are now thought to represent the low-luminosity tail of the Seyfert phenomenon (see Figure 2.1, lower left, for an example spectrum).

The activity in **radio galaxies** is not confined to the galaxy centre. The active nucleus of radio galaxies produces jets of highly relativistic particles which emit synchrotron radiation, predominantly in the radio. The jets terminate in large-scale lobes (as seen e.g. for Centaurus A in Fig. 1.3) and the total structure is typically tens to hundreds of kpc, reaching a few Mpc in some cases. Fanaroff and Riley (1974) noted that the morphology of extragalactic radio sources can be divided into two classes, depending on their luminosity. In Fanaroff & Riley

type I (**FR I**) sources the flux density of the jets and lobes steadily decreases with increasing radius. In **FR II** galaxies the radio emission is enhanced on both sides of the jet, the so-called 'hot spots', located at a distance of more than half the maximum diameter of the source. Centaurus A is often considered the prototype FR I low-luminosity radio galaxy (Israel, 1998).
Like Seyfert galaxies, radio galaxies can be divided on the basis of their optical emission line widths into **narrow-line radio galaxies (NLRG)** and **broad-line radio galaxies (BLRG)** (see Figure 2.1, lower right).

Quasars (quasi-stellar radio sources) are among the most powerful AGN. Their discovery goes back to 1963, when Maarten Schmidt broke the puzzle of the spectrum of 3C 273 by identifying several well-known nebular emission lines with the unusually large redshift of $z = 0.158$ (Schmidt, 1963). It was immediately clear these objects are highly luminous to be observable to such great distances. Corresponding radio-quiet high-luminosity objects are called **'quasistellar objects'**, or **QSOs**. Quasars and QSOs are understood as AGN, so luminous and distant, that their host galaxies could not be detected. Indeed, the distribution of quasars and QSOs as a function of redshift indicates that AGN were much more frequent in the past, with a peak in number density at $z\sim 2-3$ (Schmidt et al., 1995; Boyle et al., 2000).

Finally, **BL Lacertae** objects, or **BL Lacs** are radio-loud objects with a featureless continuum spectrum (Figure 2.1, upper left). Their name was coined by the first member of the class discovered, which was believed to be a highly variable star. The variability of BL Lacs is the most dramatic of all classes of AGN and can be measured on timescales of hours (at the shortest wavelengths) to days and months. The continuum emission is believed to be synchrotron radiation, of relativistic electrons in a magnetic field. It rises steeply from UV through optical and infrared and is strongest in radio wavelengths. It is very difficult to measure the redshift of BL Lacs since their spectra do not exhibit emission lines, and the very bright AGN outshines the underlying host galaxy. The explanation for that is the beaming of the core radiation towards the line-of-sight to the observer in a very narrow cone-angle, i.e. we see the radio jet coming directly towards us (Robson, 1996).

2.2 The source of energy - Accretion onto a black hole

The common characteristics of all classes of AGN is that a huge amount of energy is released from a tiny volume. Luminous quasars have luminosities of $L_{\rm bol} \sim 10^{47}$ erg/s and surpass the light from their stellar hosts often by at least an order of magnitude. Judging from the radio lobes of quasars, these sources of energy must last for at least 10^7 years, to reach the sizes observed today ($\gtrsim 1$ Mpc). The energy output over the lifetime of a quasar is thus $E \gtrsim 10^{47}{\rm erg/s} \times 10^7{\rm yr} \sim 3 \times 10^{61}{\rm erg}$.

The rapid brightness variations in some quasar nuclei indicate that the energy is produced in a region as small as $\sim 10^{13}$ cm, which is the corresponding light-travel distance for variations on timescales of an hour.
Assuming that the energy output comes from nuclear fusion, which has a radiative efficiency of $\epsilon \sim 0.8\%$, one needed a mass input of approximately $2 \times 10^9 \mathrm{M}_\odot$ to release the observed energies. The Schwarzschild radius for this mass, remaining at the centre as the 'ashes' of nuclear fusion, is $\mathrm{R_S} = \frac{2\mathrm{GM}}{\mathrm{c}^2} \sim 6 \times 10^{14}$ cm. This exceeds the size of the nuclear source as derived above. Thus, gravitational energy dominates over the energy output of the nuclear fusion process and excludes it as the possible source of energy.
These arguments for quasars form the basis of the idea that the source of energy for *all* AGN is the transformation of gravitational energy into radiation (Hoyle and Fowler, 1963; Lynden-Bell, 1969; Rees, 1977). Following black hole theory, the radiative efficiency for accretion onto a black hole is in the range of $\sim 6\%$ to 42%, for non-rotating and maximally rotating black holes (Krolik, 1999).
As a summary, the most compelling arguments in favour of accretion onto black holes as the energy source for AGN are:

- **Short variability** with timescales as short as minutes in low power Seyfert galaxies. The associated light travel distance sets the radius of the causally connected region and thus the radius of the source of energy.
- **High efficiency** of conversion of mass into radiation.
- **Stability of jets** over typically $10^6 - 10^7$ yrs, the time the jets need to reach their observed scales.
- **Emission line widths** of up to 5000 km/s in Seyfert galaxies and even 10.000 km/s in quasars.
- **Relativistic bulk motion** in small and large scale jets.
- **Rotation curves** of circum-nuclear gas disks observed in AGN galaxies give a direct dynamical evidence on the existence of a high central mass, of the order a few $10^5 - 10^9 M_\odot$.

2.3 The unification scheme

As seen in Section 2.1 a whole zoo of AGN phenomena has been classified today. However, the source of energy immanent to all of them is the accretion of matter onto a supermassive black hole. Therefore, the different types of AGN are believed to be physically very similar objects. The differences in their observational properties might be explained by the fact that i) some objects are more luminous than others, ii) some objects produce jets while others do not, and iii) a given AGN can have very different observational properties depending on the viewing angle.
The first point is most probably related to the accretion rate and the amount of fuel that is in a reservoir close to the central engine. The second point is still a

Figure 2.2 A schematic diagramme of the current paradigm for (radio-loud) AGN (not to scale) (adapted from Urry and Padovani, 1995). A central black hole is surrounded by a luminous accretion disk. Broad emission lines are produced in high velocity clouds close to the black hole. Narrow lines are produced in clouds much farther from the central source. In radio-loud AGN, large-scale jets emanate from the region near the black hole, initially at relativistic speeds. A thick dusty torus (or warped disk) obscures the broad-line region from line-of-sights roughly perpendicular to the jet; some broad-line emission can be seen in scattered light. The coronal emission lines are produced in the hot corona above the accretion disk.

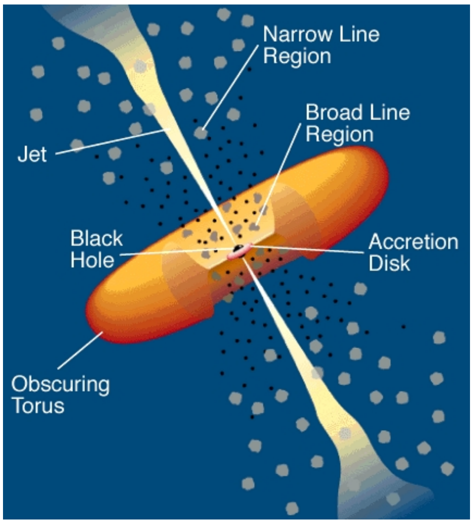

matter of debate, and some people believe that also the launching of jets is coupled to the luminosity and thus the accretion rate of the central engine.
The third factor is mainly motivated by the discrimination of Sy1 and Sy2 objects. Where Sy1 spectra show broad emission lines while Sy2 ones do not. The current unification scheme for the different AGN phenomena is sketched in Figure 2.2 (adapted from Urry and Padovani, 1995), where the main components of (radio-loud) AGN are drawn. Their characteristic sizes are given in Table 2.1.

Table 2.1 Components of AGN and their typical scales

Component	Typical size [pc]
Black hole - Schwarzschild radius	$<< 10^{-5}$
Accretion disk	$<< 10^{-2}$
Broad line region	$0.01 - 0.1$
Molecular torus	$1 - 10$
Black hole - radius of influence	$10 - 500$
Narrow line region	$10 - 1000$
Jet	$0.1 - 1 \times 10^6$

When we see close to face-on to the torus, we classify the system as a type 1 Seyfert or a QSO depending on luminosity because we see dense, fast-moving gas that is located in the **broad-line region (BLR)** close to the AGN. When we cannot see down the vortex tube, we classify the object as a type 2 Seyfert because in this case the object's spectrum is dominated by emission from low-density, relatively slow-moving, photo-excited gas that lies in the **narrow-line region (NLR)** at some distance from the central engine.

This picture is supported by the observations of polarised light in Seyfert 2 galaxies. The directly observed light shows narrow line emission, while the scattered radiation shows broad line wings. The direct evidence for the dusty torus around AGN was accomplished with interferometric mid-infrared observations that spatially resolve these structures in the galaxy NGC 1068 (Jaffe et al., 2004), a classical Sy2 galaxy.

2.4 The cosmological context

It is believed that our universe evolved hierarchically, where large objects are formed by the merging of smaller ones. This conception is supported by observations of interacting galaxies and led to the 'merger hypothesis', according to which elliptical galaxies originate when spiral galaxies collide (Toomre and Toomre, 1972; Toomre, 1977).

It has also been established that supermassive black holes are ubiquitous in the centres of galaxies (e.g. Kormendy and Richstone, 1995; Ferrarese and Ford, 2005, and references therein) and that their masses correlate tightly with global properties of their host spheroids, such as mass (e.g. Häring and Rix, 2004), luminosity (e.g. Marconi et al., 2003), or velocity dispersion (Ferrarese and Merritt, 2000; Gebhardt et al., 2000). These relations argue that supermassive black holes and galaxies are linked in an evolutionary manner, as implied by simulations showing that self-regulated black hole growth in a galaxy merger has a significant impact on the structure of the remnant (Di Matteo et al., 2005).

Observations also indicate that galaxy mergers produce starbursts and fuel black hole growth and that both play roles in structuring elliptical galaxies. Infrared-luminous galaxies appear to be powered at least in part by nuclear starbursts (for a review see Soifer et al., 1987), and the most intense of these, ultraluminous infrared galaxies (ULIRGs), are always associated with mergers (see Sanders and Mirabel, 1996, for a review). Radio observations reveal large quantities of dense gas in the centres of ULIRGs (Scoville et al., 1986, e.g.), providing material to feed black hole growth.

These lines of evidence, as well as the overlap between the bolometric luminosities of ULIRGs and quasars, suggest that quasars originate from an IR-luminous phase of galaxy evolution caused by mergers (Sanders et al., 1988). This proposal is supported by observations of nearby hosts of bright quasars that reveal features characteristic of mergers and starbursts.

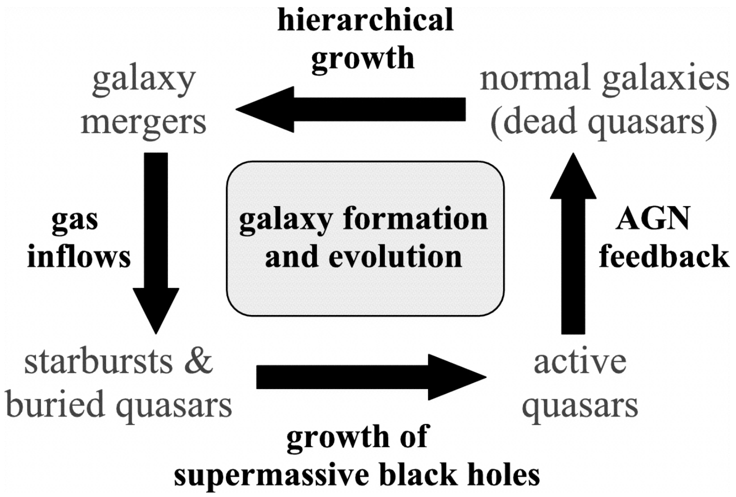

Figure 2.3 Schematic representation of a 'cosmic cycle' for galaxy formation and evolution regulated by black hole growth in mergers (adapted from Hopkins et al., 2006a).

Numerical simulations of galaxy mergers that account for black hole growth, star formation, and stellar and BH feedback (Springel et al., 2005; Di Matteo et al., 2005; Hopkins et al., 2006a,b) are extremely successful in explaining the observed properties of galaxies and their tight correlations to the mass of the central black hole. They show that gas inflows excited by gravitational torques during a merger both trigger starbursts and fuel rapid black hole growth. The growth of the black hole is determined by the gas supply and terminates as gas is expelled by feedback, halting accretion, leaving a dead quasar in an ordinary galaxy. This 'cosmic cycle' for galaxy formation and evolution is sketched in Figure 2.3.

Moreover, observations show that the star formation rate in galaxies is not constant throughout the history of the universe, but depends on redshift (Madau et al., 1996; Hopkins and Beacom, 2006). The same is true for the luminosity function of quasars (Chaffee et al., 1991; Hewett et al., 1993), and interestingly, these two functions peak at around the same redshift range of z$\sim$ $1-2$, giving more evidence that the two phenomena of star formation and AGN activity are linked.
Understanding the relation between quasar and merging galaxy luminosity functions and the merger-driven star formation history of the universe is an active field of extragalactic research (e.g. Hopkins et al., 2006b; Bell et al., 2005, 2006).

3. Adaptive optics observations of AGN

Our own Milky Way's centre shows that galaxy centres become increasingly more interesting when observed at higher and higher spatial resolution. The sphere of influence of the black hole is typically in the range $10 - 500$ pc, which corresponds to $\sim 0\farcs1 - 5$", depending on galaxy distance. It is thus only resolvable in the most nearby galaxies that harbour supermassive black holes. High angular resolution is desirable to directly observe and resolve the components that form the current paradigm of AGN: the narrow line region, the dusty torus, the broad line region and eventually the accretion disk.

3.1 The need for adaptive optics observations

Ground based optical telescopes have undergone an increase in mirror size over the last decades, reaching mirror sizes of up to eight or even ten meters today (Very Large Telescope, Large Binocular Telescope, and Keck telescopes). That means that both the light collecting area of the telescopes increased and their view was sharpended due to an increase in resolving power. It is now possible to detect ever fainter and thus more distant objects and resolve smaller and smaller structures.
In theory, the resolving power of a telescope is limited by diffraction, i.e. the light is interfering with itself. This is analogous to the diffraction of light in a single slit experiment, but in the case of a telescope this is a two-dimensional phenomenon, and so the diffraction pattern is a set of concentric rings, the so-called Airy pattern. An empirical diffraction limit is given by the Rayleigh criterion invented by Lord Rayleigh:

$$\sin\theta = 1.22\frac{\lambda}{D}, \tag{3.1}$$

where θ denotes the angular resolution, λ is the wavelength of the observed light, and D gives diameter of the telescopes mirror. For example, the diffraction limit of a single VLT 8.2 m telescope is 39 milliarcseconds (mas) ($0\farcs039$) at J-band wavelengths, $0\farcs055$ in H-, and $0\farcs057$ in K-band.
In practice, the resolution of astronomical observations is limited by the atmospheric conditions at the time they are taken. The light coming from a star passes through the Earth's atmosphere and the initially parallel wavefront will be distorted. This distortion depends on the turbulence of different gas layers in the

Earth's atmosphere. This implies that the star will not appear as a point source at a fixed position on the sky. Its light breaks up in a so called 'speckle pattern' and seems to jitter. In long exposures this causes the starlight to be smeared out over an area of the detector, the 'seeing disc', that is a measure for the atmospheric turbulence. The most common way to express the astronomical seeing is via the full width at half maximum (FWHM) of the seeing disk. At the best sites for observatories, the seeing disk reaches values as small as $0\farcs4$ under the best conditions.

Even the best observing conditions do not allow the observer to use the full resolving power of an 8m class telescope. Already under the best possible conditions, the seeing disk is a factor of seven larger than its theoretical value! This is not satisfactory and motivated scientists to develop a technique to minimise the effects of atmospheric turbulence: adaptive optics.

3.2 Towards the diffraction limit: adaptive optics

The basic idea of adaptive optics instrumentation is to measure the distortion of the observed wavefront and to reconstruct its original shape, i.e. flatten it. An adaptive optics system consists of three main parts: 1) a wavefront sensor (WFS), 2) a real time computer (RTC), and 3) a deformable mirror (DM). The WFS measures the distortion of the light throughout the field-of-view, while the computer calculates the optimal mirror shape to correct the distortions in and the surface of the deformable mirror is reshaped accordingly.

There are different types of WFS used in adaptive optics systems, and their common principle is to measure the shape of the incoming wavefront. More precisely, the 'Shack-Hartmann sensor' subdivides the pupil into small sub-apertures by means of a lenslet array (Hartmann, 1900; Shack and Platt, 1971). The local slope of the abberated wavefront can then be measured via its displacement in each sub-aperture with respect to a reference position. The 'curvature wavefront sensor' (Roddier, 1988) determines the curvature of an incoming wavefront by measuring the change of intensity of two symmetrically out of focus images.

3.2.1 General requirements and limitations

In order to correct the wavefront of the science target, one needs a reference source for which the exact shape and position is known. This is in most of the cases a bright 'guide star' ($m \lesssim 14$ mag) for which precise coordinates are available. Low order corrections, (e.g. 'tip-tilt'), could in principle be achieved on fainter stars as well, but the higher order corrections are only achievable when enough flux reaches each sub-aperture (in the Shack-Hartmann case).

The correction of the wavefront will be optimised for the actual position of the guide star. It is therefore desirable that the science target lies as close as possible, since then their wavefronts pass the same atmospheric turbulence. For angles larger than the 'isoplanatic patch', θ, the atmospheric turbulence pattern becomes decorrelated for the guide star and the science target and the correction becomes meaningless. This effect is know as anisoplanatism.

The availability of natural guide stars thus imposes a severe restriction on the choice of science targest accessible to AO observations. The so-called 'sky-coverage' for observations in K-band is $\lesssim 10\%$. This problem will be partly solved with the advent of laser-guide stars attached to AO systems.

3.2.2 Special case of AGN observations

For adaptive optics observations of AGN one is in the favourable situation of having a bright source right at the centre of interest. During the observations with Naos-Conica (NaCo) at the Very Large Telescope (VLT) of the MPIA nearby AGN sample (Prieto and Meisenheimer, 2004), we could show that this strategy is indeed feasible. In most of the cases, the AGN is actually bright enough in visible wavelengths and it is possible to use the visible WFS for the wavefront correction. The advantage is that one can then use all the light in the near-infrared for the science case.

However, some AGN are heavily obscured by dust - like for instance Cen A - and are not detectable at visible wavelengths. One can then switch to the unique infrared WFS implemented in NaCo, that has an equally good performance.

The guiding on the AGN is unfortunately not as straightforward as for bright stars in the field. The AGN might be as bright and even as point-like as a star, the key difference, however, is that the contrast between the AGN and the underlying stellar body is severely lower than for any star (even in crowded regions like the Galactic Centre). It is therefore crucial to account for that in the set-up of the WFS, in particular when estimating the local background.

The great advantage of using the AGN as the reference source for AO observations is clearly its very central position that guarantees for the best possible correction in its vicinity. The drawback that directly comes with this, is that for obscured AGN one needs to invest a fair amount of light of the science target for the actual wavefront correction.

3.3 Characterisation of AO data

The data (both images and spectra) obtained with an adaptive optics assisted instrument are more complex than for seeing limited observations. The AO correction will always be limited by the number of fitted modes and the residual wavefront error. AO-systems provide only a partial correction of the turbulence degraded point-spread-function (PSF).

3.3.1 Understanding the PSF

Depending on the quality of the performed correction, the AO-PSF may be seen as in-between the seeing disk and the ideal Airy-disk. In order to understand the formation and resulting shape of a long term exposure PSF one may start by considering a short term exposure PSF first (recorded with an integration time of the order of the coherence time, which sets the timescale for atmospheric aberrations). A short exposure PSF is dominated by a characteristic speckle pattern, depending on the size of the telescope mirror D and on the characteristic size of the atmospheric turbulence r_0. According to diffraction theory, for a given wavelength λ, speckles have a size of roughly λ/D and are randomly distributed over an area $\lambda/r0$, which defines the size of the seeing disk. Due to the temporal variability of the phase of the incoming wavefront, the speckle pattern changes in time and results - in the case of a long term exposure - in the seeing disk. When turbulence is compensated by means of adaptive optics, the residual phase error decreases and energy is transferred coherently from the seeing halo to the diffraction limited core of the PSF. Hence, the PSF for AO observations is characterised by two components i) the diffraction limited core plus ii) the seeing limited halo.

$$\mathrm{PSF_{AO}} = \mathrm{C} \cdot \mathrm{PSF_{core}} + (1 - \mathrm{C}) \cdot \mathrm{PSF_{seeing}} \tag{3.2}$$

The quantity C is called ‘coherent energy’, and gives the fraction of light in the coherent diffraction core of the corrected image. The halo is formed by the incoherent summation of speckle noise originating from uncorrected wavefront errors. By increasing the quality of the correction, more and more energy is transferred from the halo into the core.

The total flux of the science target is distributed into the core and the seeing halo according to

$$\mathrm{F_{total}} = \mathrm{F_{core}} + \mathrm{F_{seeing}} = \mathrm{C} \cdot \mathrm{F_{total}} + (1 - \mathrm{C}) \cdot \mathrm{F_{total}} \tag{3.3}$$

3.3.2 Strehl ratio

An important quantity to classify the quality of the partially corrected PSF is the Strehl ratio (Strehl, 1902). As shown above, residual wavefront errors lead to a degradation of the shape of the ideal PSF, since part of the flux of the diffraction limited core remain in the seeing halo, leading to a decrease of the peak intensity. The Strehl ratio is defined as the ratio of the peak intensity of the observed PSF $\mathrm{I_{obs}}$ to the peak intensity of the theoretical PSF of the optical system $\mathrm{I_{Airy}}$ (the peak of the first Airy-disk):

$$S = \frac{\mathrm{I_{obs}}}{\mathrm{I_{Airy}}} \tag{3.4}$$

For seeing limited observations in K-band the Strehl ratio is typically under 1% and can reach up to 70% for adaptive optics observations. The coherent energy tends towards the Strehl ratio if the performance of the AO correction is very good.

3.3.3 Towards a model PSF

For the data analysis and the assessment of the image quality it is desirable to obtain an accurate analytic model of the spatial PSF. To that aim Equation 3.2 serves as a starting point, and we look for the best set of model functions for $\mathrm{PSF}_{\mathrm{core}}$ and $\mathrm{PSF}_{\mathrm{seeing}}$. The coherent energy C, that sets the weight for these two functions, is derived from Equation 3.3, as $\mathrm{C} = \mathrm{F}_{\mathrm{core}}/\mathrm{F}_{\mathrm{total}}$.
For seeing limited observations it is a common technique to measure the point-spread-function on a separate PSF-reference star that is observed immediately after the science target. This is in principle also possible for AO observations. However, the AO correction and thus the AO-PSF does not only depend on the atmospheric conditions at the time of the observations (seeing, coherence time) but also on the observable properties of the reference source (brightness, contrast, size). Experience told us that observations of a separate PSF-star at a different position in time and position on the sky does not guarantee to give a good approximation on the actual on-source PSF. We therefore came to the conclusion that for AGN imaging and spectroscopy it is most suitable to measure the PSF in the science frame on the unresolved nucleus.
The situation for AGN observations is more complex than ‘just’ fitting a two component PSF model, as the light of the underlying stellar body needs to be separated from the PSF model. To remove the contribution of the stellar body we fitted a smooth model to the galaxy light profile as shown in Figure 3.1. We test this approach by comparing the PSF models for subtracted and non-subtracted galaxy light and find very similar results.

The PSF-model is then fitted to the isolated peak, shown in Figure 3.1 as the red line. We find that the simplest approach, of fitting two Gaussians, already leads to a very satisfying result. The normalised PSF can be approximated by a sum of two Gaussians; one narrow component describing the corrected/almost diffraction limited PSF core (σ_{core}) and one broader component corresponding to the seeing halo (σ_{s}):

$$\mathrm{PSF(r)} = \frac{\mathrm{C}}{2\pi\sigma_{\mathrm{core}}^2} \mathrm{e}^{-\mathrm{r}^2/2\sigma_{\mathrm{core}}^2} + \frac{(1-\mathrm{C})}{2\pi\sigma_{\mathrm{s}}^2} \mathrm{e}^{-\mathrm{r}^2/2\sigma_{\mathrm{s}}^2},$$

where C is the coherent energy, or in other words the ratio of the flux of the core component and the total flux of the PSF ($\mathrm{C} = \mathrm{flux}_{\mathrm{core}}/\mathrm{flux}_{\mathrm{total}}$).

The fit to the central ±1” is shown in Figure 3.2. The values that lead to this fit are $\sigma_{\mathrm{core}} = 0\farcs15$, $\sigma_{\mathrm{s}} = 0\farcs53$, and C=0.15. These are observations in H-band where the diffraction limit of the VLT is theoretically $0\farcs055$. Note that we used the largest possible pixelsize of $0\farcs054$/pix in order to enhance the signal-to-noise ratio in our gas emission lines. However, this lead to severe undersampling of our PSF. The estimated error on the coherent energy is $\sim 25\%$. This uncertainty in the determination of the PSF needs to be part of the error analysis, when using adaptive optics observations for modelling black hole masses.

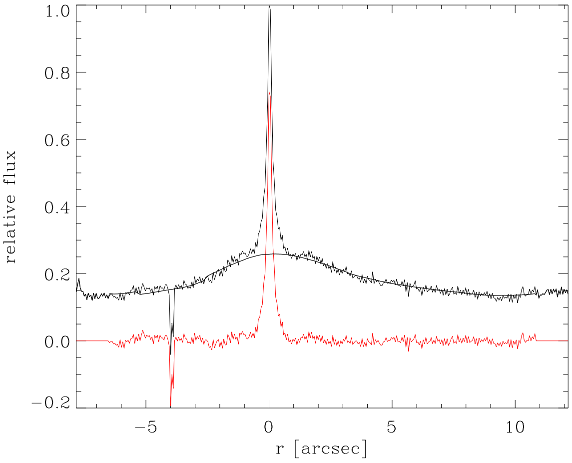

Figure 3.1 Subtraction of a smooth model from the galaxy light profile. The black line shows the light profile across Cen A's nucleus at a position angle of 82°.5. The nucleus clearly peaks out of the underlying stellar body, that is fitted by a smooth model (thick black line), and subtracted to get the nuclear peak only (red line).

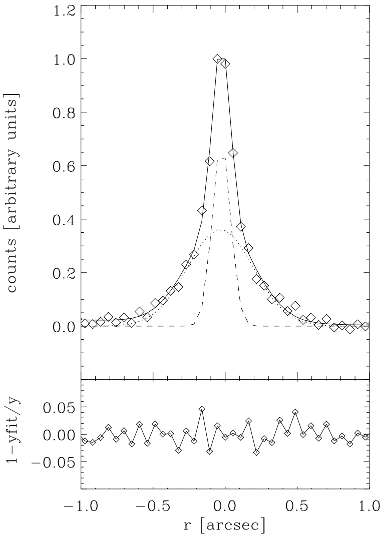

Figure 3.2 Decomposition of the PSF for the NaCo spectroscopy data (slit position angle 82°.5). The data are over plotted by the 2-component PSF-model (solid line), where the dashed line indicates the corrected peak and the dotted line represents the uncorrected seeing halo. The bottom panel shows the residual between model and data.

3.4 Naos-Conica

The Nasmyth Adaptive Optics System (Naos) (Rousset et al., 1998) and the high-resolution Near IR Camera (Conica) (Lenzen et al., 1998) are installed at the Nasmyth B focus of YEPUN (UT4) at the ESO Very Large Telescope (VLT) on Cerro Paranal, Chile. Naos-Conica provides multimode, adaptive optics corrected observations in the range $1-5\,\mu$m. Naos is an adaptive optics system designed to work with natural guide stars and extended objects. Provisions have been made for it to work with a laser guide star. Naos is equipped with both visible and infrared, Shack-Hartmann type, wavefront sensors. Typical magnitude limits for the AO guide star are: V=16.7 and K=12 (13 with the N90C10 dichroic) at a maximal distance of $\theta = 55$".
Conica is an infrared (IR) ($1-5\,\mu$m) imager and spectrograph which is fed by Naos and is equipped with an Aladdin 1024×1024 pixel InSb array detector. It is capable of imaging, long slit spectroscopy, coronographic and polarimetric observations with three different plate scales of 54 mas/pix, 27 mas/pix and 13 mas/pix, leading to field of views on the sky of 55" × 55", 27" × 27", and 13" × 13", respectively.

We obtained data, both imaging and spectroscopy, with NaCo on the nucleus of Cen A. These data, presented in Chapter 4, are used to construct a full dynamical model of the gas kinematics inside the inner $r \sim 1$", in the close vicinity to its active galactic nucleus. Moreover, the imaging data are used to study the circumnuclear star formation in Cen A, as presented in Chapter 6.

3.5 SINFONI

SINFONI is a near-infrared ($1.1-2.45\,\mu$m) integral field spectrograph fed by a curvature sensing adaptive optics module (Eisenhauer et al., 2003b; Bonnet et al., 2004). The spectrograph operates with 4 gratings (J, H, K, H+K) providing a spectral resolution around 2000, 3000, 4000 in J, H, K, respectively, and 1500 in H+K each wavelength band fitting fully on the 2048 pixels of the Hawaii 2RG (2k×2k) detector in the dispersion direction. The SINFONI field of view on the sky is sliced into 32 slitlets. Pre-optics allow to chose the angular size of the slices on the sky. The choices are 250 mas, 100 mas, 25 mas, leading to field of views on the sky of 8" × 8", 3" × 3", or $0\farcs8 \times 0\farcs8$, respectively. Each one of the 32 slitlets is imaged onto 64 pixels of the detector. Thus, one obtains $32 \times 64 = 2048$ spectra of the imaged region of the sky. Typical limiting magnitudes (S/N=10 in 1h on source) are around $17-18$ mag in J, H, K.
For best correction, the guide star should be brighter than R$\sim$ 11 mag. However, the AO will provide a moderate image quality improvement with stars as faint as R$\sim$ 17 mag in the best seeing conditions. Ideally, the AO guide star should be as close as possible to the scientific target (if not the science target itself), and usually closer than 10". Depending on the atmospheric conditions (atmospheric

coherence length) the AO guide star could be chosen as far as 30” for the AO system to still provide a mild improvement of the encircled energy.

The nucleus of Cen A was observed with SINFONI, to get 2D information on the flux distribution of different gas species and especially their kinematical structure, similarities and differences. This data set is presented in Chapter 5.

4. Weighing the black hole in Cen A with NaCo[1]

4.1 Introduction

Galaxy merging, the formation of stellar spheroids, nuclear star-formation and the fueling of nuclear black holes appear to be all linked, forming a central theme in building galaxies. Most galaxies where these processes are currently acting, are so far away that the 'sphere of influence' of the black hole cannot be spatially resolved and that detailed studies of stellar populations are impossible. Yet, our own Galactic Center alone tells us that galaxy centers tend to become increasingly more interesting when observed at higher and higher spatial resolution (e.g. Schödel et al., 2002; Genzel et al., 2003). When zooming into the nucleus of Centaurus A (NGC 5128), recent HST imaging (NICMOS) and ISAAC observations have also revealed smaller and smaller 'sub-systems' (Schreier et al., 1998; Marconi et al., 2000, 2001). Cen A, the closest massive elliptical galaxy, the nearest recent merger, and one of the nearest galaxies with a significantly active nucleus provides a unique laboratory to probe the interconnection between these phenomena on scales that are contained in the central resolution element in any other object of its kind.

The intricate dust lane that hides the center of Cen A has not allowed optical high-resolution spectroscopy with HST. Infrared (IR) spectroscopy is thus increasingly important to open up the regime of dust shrouded nuclei and get accurate black hole mass measurements for these objects.

Cen A is especially interesting since the black hole mass deduced by Marconi et al. (2001) ($\mathrm{M_{BH}} = 2.0^{+3.0}_{-1.4} \times 10^8 \mathrm{M}_\odot$) lies a factor of ten above the $\mathrm{M_{BH}}$-σ relation (Ferrarese and Merritt, 2000; Gebhardt et al., 2000). This is the largest offset from the relation measured to date. It is important to check this value, since it can help us to understand the coevolution of black holes and their surrounding bulges in more detail.

We have initiated a program to study the central parsec of Cen A using Naos-Conica (Rousset et al., 1998; Lenzen et al., 1998) at the Very Large Telescope (VLT). The adaptive-optics assisted imager and spectrograph provides us with near infrared data from 1 to 5 μm at the diffraction limit of a 8m class telescope.

---

[1] Häring-Neumayer et al. 2006, ApJ, 643, 226

The resolution is thus nearly fourfold that of HST in K-band.
The distance to Cen A is still under discussion. In a comprehensive review Israel (1998) gives a value of 3.40±0.15 Mpc. Tonry et al. (2001) finds a value of 4.2±0.3 Mpc from I-band surface brightness fluctuations, and recently, Rejkuba (2004) derived a distance of 3.84±0.35 Mpc from Mira period-luminosity relation and the luminosity of the tip of the red giant branch. Here, we assume a distance of D=3.5 Mpc to be consistent with the black hole mass measurements of Marconi et al. (2001) and Silge et al. (2005) that also used that value.
The paper is structured as follows: in Section 2 we present the observational strategy and the data reduction. Section 3 describes the treatment of the spectral data. Section 4 presents the dynamical modeling and the results for the black hole mass for Centaurus A, and Section 5 discusses the implications of these results.

4.2 Observations and data reduction

4.2.1 Adaptive optics observations

Near infrared observations were performed in 2004 March 28 and 31 with Naos-Conica (NaCo) at the Yepun unit (UT4) of the Very Large Telescope (VLT). NaCo consists of the high-resolution near-infrared imager and spectrograph Conica (Lenzen et al., 1998) and the Nasmyth Adaptive Optics System (Naos) (Rousset et al., 1998). It provides adaptive-optics corrected observations in the range of 1-5 μm with $14''$ to $54''$ fields of view and 13 to 54 mas pixel scales.
The data were taken in visitor mode and seeing during observations was in the range $0\farcs3$-$0\farcs8$ (as measured by the seeing monitor in V-band), with clear/photometric conditions.

Not seen in the visible, the active nucleus at the center of Centaurus A is an unresolved source in K-band of 10.9 mag as detected by Marconi et al. (2000). There are no potential reference stars bright enough ($m_K \leq$14 mag) for the wavefront correction at a distance of $\leq 30''$ to the nucleus, necessary for a good quality of correction at the nucleus. Therefore, we directly guided on the nucleus itself using the unique IR wavefront sensor implemented in Naos. This strategy provides us the best possible wavefront correction in the vicinity of the active galactic nucleus (AGN). In fact we reach the diffraction limit of the VLT in K-band of FWHM $0\farcs057$ and are not far off in H-band with $0\farcs11$. During the observations the atmospheric conditions were stable and the performance of the IR wavefront sensor (WFS) was steadily very good. For observations in H-band we used the K-dichroic, i.e. all the nuclear K-band light for wavefront correction. While observing in K-band itself the only possibility to achieve a good performance of the WFS was to send 90% of the light to Naos and only 10% to Conica (i.e. use the N90C10 dichroic). This increases the exposure times by a factor of 10 and made it effectively impossible to go for spectroscopy in K-band.

4.2.2 K-Band imaging

For the imaging we chose the strategy to jitter the field on five positions at a separation of 4″ and take a sky image at a dark position in the dust lane at a distance of ∼170″ South-East of the nucleus; this cycle was repeated 4 times. The on-chip exposure time was 120 s, yielding a total exposure time on the nucleus of 40 min. The resulting K-band image is shown in Figure 4.1.

The atmospheric conditions were stable and the seeing was 0.″5 at the start and 0.″8 at the end of the observations.

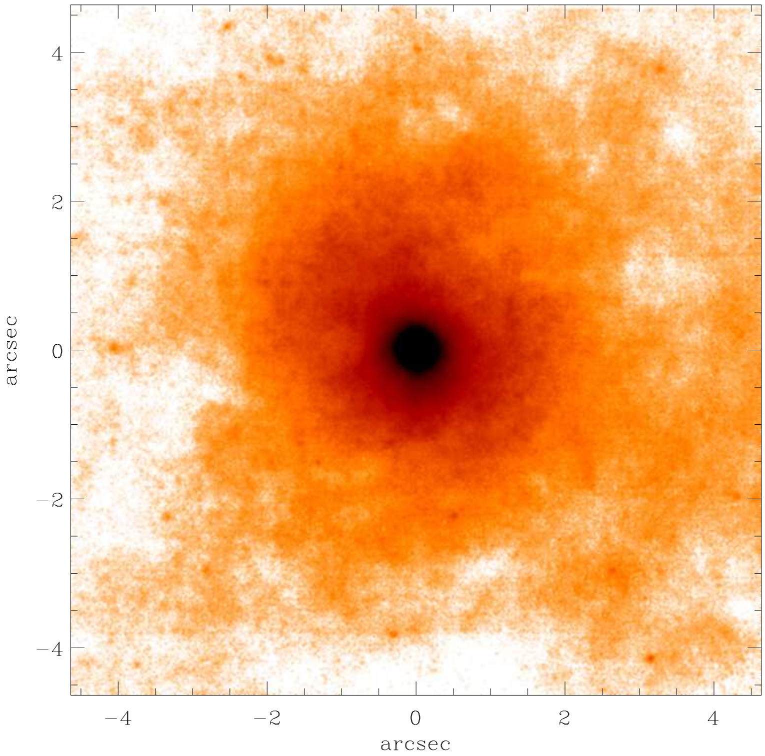

Figure 4.1 K-band image taken with NaCo. The nucleus is clearly visible as the unresolved source (FWHM=0.″06). North is up and East is to the left.

4.2.3 H-band spectroscopy

We took H-band spectra at 4 different position angles and chose three similar to Marconi et al. (2001) (P.A.= -44.°5, 32.°5, and 82.°5) in order to complement their findings with better spatial resolution. The fourth slit position (P.A.=70.°5) was chosen as to observe the nucleus and a foreground star simultaneously to monitor the point spread function (PSF) on a stellar reference. See Figure 4.2 for the positioning of the slits.

The observations were obtained with the 0.″086 slit and a grating with a wavelength range from $\lambda = 1.37\,\mu$m to $1.84\,\mu$m. The pixel scale was $0\farcs054$ leading to a slight under-sampling but shorter exposure times. The dispersion was 7.0 $\AA$ pixel^{-1}, yielding a resolution of R=1500 in H. At a given position angle, the observations went as follows: first, the loop for adaptive optics correction was closed. When a good performance of the WFS was reached, an acquisition image in H-band was taken. The slit was centered on the prominent nuclear peak with an accuracy of ±0.2pixel ($\pm0\farcs011$). The actual observations consisted of two sequences of exposures at 4 positions along the slit. This was done in order to perform sky subtraction and to avoid detector defects. The effective slit length is $14''$. The exposure time per frame was 300 s, leading to a total exposure time of 40 min per slit position angle.

Data reduction was performed using standard IRAF routines. The frames were first bias corrected and flat-fielded with spectroscopic lamp-flats. Then cosmic rays were rejected and the frames were wavelength calibrated and corrected for distortions using spectroscopic arc lamps.

To get the final 2-D spectrum the frames were aligned. This is done by shifting all frames to the same nuclear position. Finally, the frames were sorted by quality of wavefront correction, using both the width of the peak and the level of continuum flux.

4.2.4 PSF-reconstruction

A difficult but crucial part of adaptive optics observations is the assessment of the point spread function (PSF). The PSF is highly dependent on the quality of the wavefront correction, quantified e.g. by the Strehl ratio. The Strehl ratio is set by the observable properties of the reference object (flux, size, contrast) but also by the atmospheric conditions (seeing, coherence time); it is therefore changing with time and needs to be monitored throughout the observations. In case of the K-band image a separate PSF reference star was observed directly after the nucleus with the same WFS setup. This star was chosen from the 2MASS point source catalogue (Cutri et al., 2003) to match Cen A's nucleus as closely as possible: in angular proximity, magnitude and color.

Since the acquisition for NaCo observations takes a non-negligible amount of time, going back and forth to the PSF star is a tedious and time-consuming task. On the other hand the measurement of a separate PSF-star at a given difference in time and position on the sky does not guarantee to give a good approximation on the actual on-source PSF. We therefore came to the conclusion that it is most suitable to measure the PSF in the science frame on the unresolved nucleus.

For emission line spectroscopy the strategy is to have the nucleus in the slit at all position angles and measure the PSF on this unresolved point-source for each frame. We tested this approach by choosing one position angle (P.A.$= 70°$) such that the nucleus plus a foreground star are simultaneously observed, and indeed,

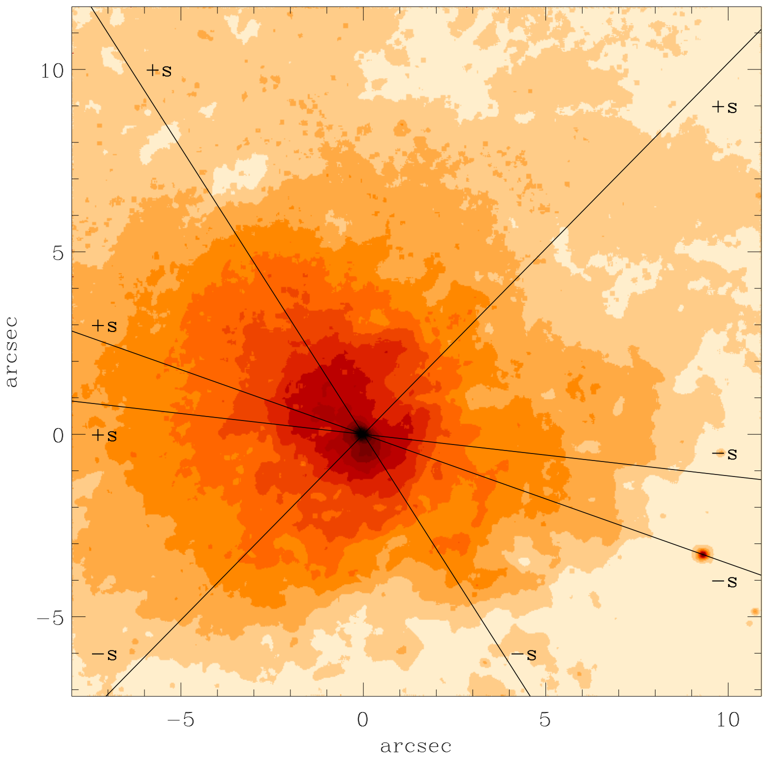

Figure 4.2 Slit positions overlaid onto the H-band acquisition image. North is up and East is to the left. From North to South the slit positions are 32.°5, 70.°5, 82.°5, and -44.°5. The sign of the position along the slit used in the rotation curves is indicated by '+s' and '-s'. Note the foreground star that is in the slit at P.A.=70.5° in the lower right.

the widths of both light profiles are similar (compare Table 4.1).

We describe the normalized PSF empirically by a sum of two Gaussians; one narrow component describing the corrected/almost diffraction limited PSF core ($\sigma_{\rm core}$) and one broader component which we later attribute to the seeing halo ($\sigma_{\rm s}$):

$$\mathrm{PSF(r)} = \frac{\mathrm{F}}{2\pi\sigma_{\rm core}^2} \mathrm{e}^{-\mathrm{r}^2/2\sigma_{\rm core}^2} + \frac{(1-\mathrm{F})}{2\pi\sigma_{\rm s}^2} \mathrm{e}^{-\mathrm{r}^2/2\sigma_{\rm s}^2}, \tag{4.1}$$

where F is the ratio of the flux of the narrow component and the total flux of the PSF ($\mathrm{F} = \mathrm{flux}_{\rm core}/\mathrm{flux}_{\rm total}$). The quantity F provides a rough approximation of the Strehl ratio (S) which gives the quality of an optical system; S is defined as the observed peak flux divided by the theoretically expected peak flux of the Airy disk for the optical system ($\mathrm{S} = \mathrm{peakflux}_{\rm core}/\mathrm{peakflux}_{\rm Airy}$). For the following analysis it is sufficient to measure the quantity F, which also gives an estimate of the quality of the adaptive optics correction.
The width of the fitted broad component can be compared with the seeing that is given in the header for each frame, as measured by the seeing monitor in V-band.

One has to adjust the seeing estimates to the same wavelength, as the resolution θ depends on wavelength λ, as $\theta(\lambda) \sim \lambda^{-1/5}$. The individual components are given in Table 4.1 and are compared to the header information (adapted to H-band). The agreement between σ_s and σ_DIM is satisfactory in all cases. Notice also the good agreement between the width of the nucleus and the star at P.A.=$70\overset{\circ}{.}5$. The adaptive optics correction is optimised for the position of the nucleus and is worse at the position of the star due to anisoplanetism.

Moreover it is obvious that the width of the narrow component depends on the seeing conditions.

Figure 4.3 shows the integrated flux over the two-component model PSF shown already in Chapter 3 in Figure 3.2. Note that 50% of the flux lie within a radius of $0\overset{\prime\prime}{.}1$ and 90% of the flux within $0\overset{\prime\prime}{.}3$.

In the PSF model we did not account for the undersampling of the observed PSF, since the sampling problem is negligible compared to the general uncertainty in adaptive optics observations.

Table 4.1 Reconstruction of the PSF

Object	P.A.	$\mathrm{FWHM}_\mathrm{core}$	FWHM_s	$\mathrm{FWHM}_\mathrm{DIM(H)}$	F
Nuc	$32\overset{\circ}{.}5$	$0\overset{\prime\prime}{.}11$	$0\overset{\prime\prime}{.}37$	$0\overset{\prime\prime}{.}37$	0.23
Nuc	$-44\overset{\circ}{.}5$	$0\overset{\prime\prime}{.}15$	$0\overset{\prime\prime}{.}48$	$0\overset{\prime\prime}{.}48$	0.18
Nuc	$82\overset{\circ}{.}5$	$0\overset{\prime\prime}{.}15$	$0\overset{\prime\prime}{.}53$	$0\overset{\prime\prime}{.}49$	0.15
Nuc	$70\overset{\circ}{.}5$	$0\overset{\prime\prime}{.}11$	$0\overset{\prime\prime}{.}34$	$0\overset{\prime\prime}{.}35$	0.22
Star	$70\overset{\circ}{.}5$	$0\overset{\prime\prime}{.}12$	$0\overset{\prime\prime}{.}36$	$0\overset{\prime\prime}{.}35$	0.31

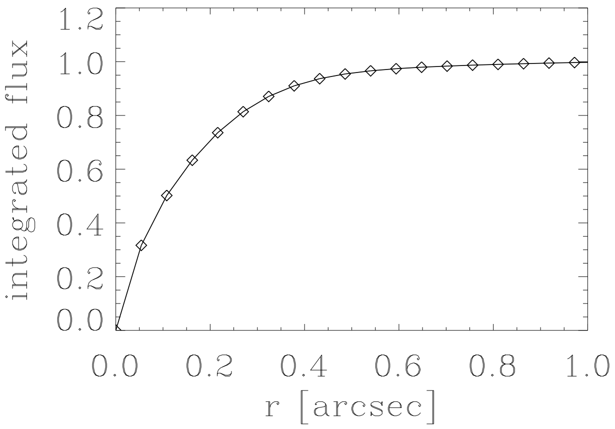

Figure 4.3 Integrated flux over the model PSF is shown for the slit position angle $82\overset{\circ}{.}5$ (to be compared with Figure 3.2).

4.3 Results

4.3.1 Nuclear spectrum

A nuclear H-band spectrum centered on the continuum peak (Fig. 4.2) and extracted from a 0.″054 × 0.″086 aperture is presented in Figure 4.4. The spectrum exhibits a power-law continuum with three [FeII] lines: $\lambda_1 1.534\,\mu$m, $\lambda_2 1.644\,\mu$m, and $\lambda_3 1.677\,\mu$m. We use the strongest line ($\lambda_2 1.644\,\mu$m) for our kinematical studies.

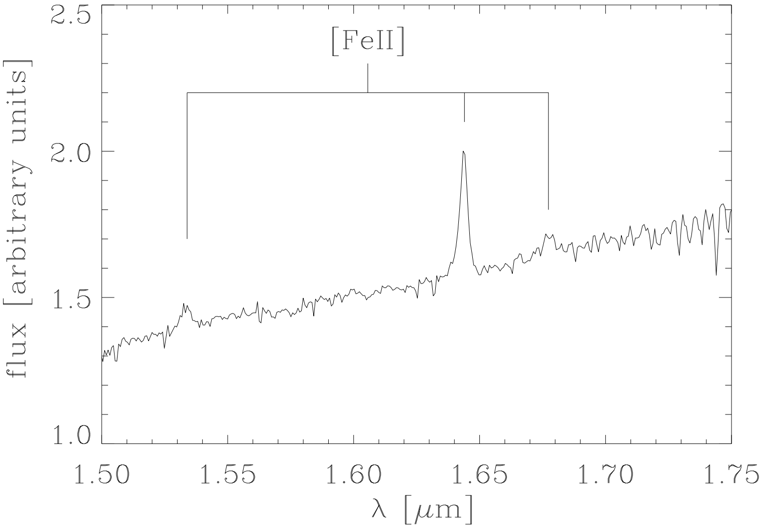

Figure 4.4 Nuclear spectrum in H-band extracted from an aperture of 0.″054 × 0.″086 at a slit position of 32.°5. The three [FeII] emission lines are indicated at the rest-frame wavelengths: $\lambda_1 1.534\,\mu$m, $\lambda_2 1.644\,\mu$m, and $\lambda_3 1.677\,\mu$m.

Line-of-sight velocities, FWHMs, and surface brightnesses along each slit were obtained by fitting single Gaussians to the [FeII] emission line in each row of the continuum-subtracted two-dimensional spectra. The corresponding slit positions are shown in Figure 4.2 and listed in Table 4.1.

4.3.2 Gas kinematics

We measure the gas kinematics on the ionised [FeII] line $\lambda 1.644\,\mu$m out to around ±0.″6. Single Gaussians provide a good fit to the emission lines and are used to measure the position and width of the line. The fit is performed in IDL[2] using a non-linear least squares fit to the line and the errors are the 1-σ error estimates of the fit parameters. The center of the continuum peak is taken as a reference for the systemic velocity. We find a value of v_{sys}=532 km s^{-1}; in good agreement with the value v_{sys}=532±5km s^{-1} measured by Marconi et al. (2001) from their gas kinematical data.

---

[2] See http://www.rsinc.com.

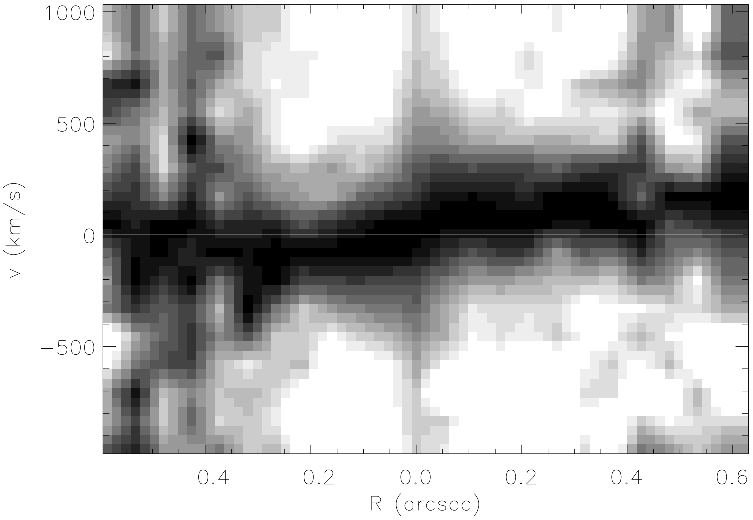

Figure 4.5 Observed [FeII] $\lambda_2 1.644\,\mu$m line on the NaCo H-band spectrum at a slit position of -44°.5. To make the gas velocity curve more visible, each column of the spectrum was divided by the maximum value of the emission line in that column. The spectrum was then resampled on a 3 times finer grid by means of bilinear interpolation. The line indicates the systemic velocity of 532 km s^{-1}, which is shifted to zero for this plot.

For the central 0.″3 only the four highest quality frames are considered in order to make use of the full resolution. The quality of the frames, i.e. their correction quality, is estimated on the basis of the width and the peak value of their continuum peak. Outside 0.″3, when the lineflux drops, all frames are taken into account and three pixels are binned to enhance the signal-to-noise ratio.
The rotation of the gas can be directly seen in Figure 4.5, where the line intensity was normalised by the peak intensity in each column. The rotation curves, velocity dispersion curves and emission-line surface brightness profiles are shown in Figure 4.6 for all slit positions.

The velocity dispersion is directly measured as the width of the lines. We corrected for instrumental broadening of 65 km s^{-1}, measured from the skylines. The excellent spatial resolution of the NaCo data is demonstrated in Figure 4.7 where we compare the NaCo data points to the kinematical data published by Marconi et al. (2001) and Silge et al. (2005). The NaCo velocity dispersions are often considerably smaller than the ISAAC velocity dispersions measured at the same location. The information given in Marconi et al. (2001) is not sufficient to find the reason for this discrepancy and we believe that our data points are correct.

4.3.3 The emission-line surface brightness

The intrinsic surface brightness distribution of emission lines Σ is an important ingredient in the model computations because it is the weight in the averaging of

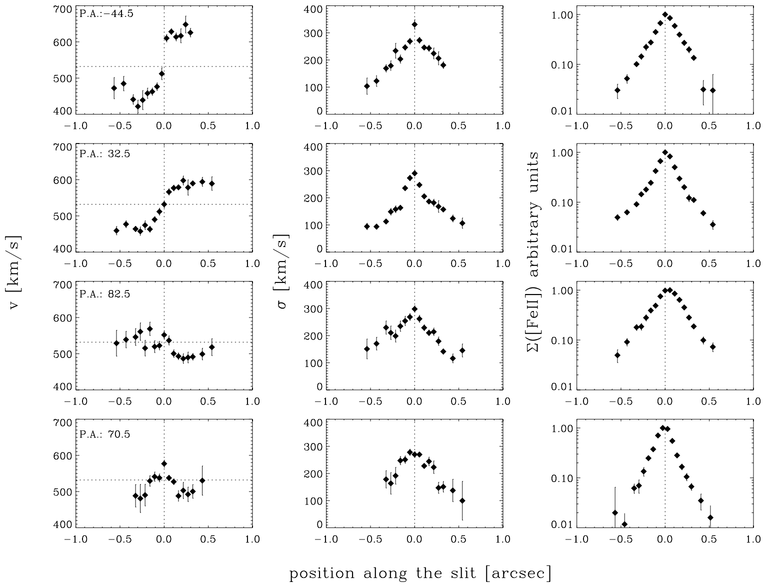

Figure 4.6 Rotation curves (left panel), velocity dispersion profiles (middle panel) and emission line surface brightness profiles (right panel) along the 4 slit positions. For the position angles $-44{.}^{\circ}5$ and $70{.}^{\circ}5$ some of the points shown in the surface brightness profile are missing for the v and σ profiles.

the observed quantities. It would be ideal to have an emission line image with higher spatial resolution than the spectra. Unfortunately, the resolution of the HST [FeII] narrow band image (Marconi et al., 2000) is not good enough to mimic the NaCo data and therefore our approach is to match the emission-line fluxes as observed in the spectra. We extracted the emission line surface brightness from [FeII] directly from the spectra along the four slit positions (see Figure 4.6, right panels).

In order to get a parametrisation for the intrinsic surface brightness, we test different functional forms and convolve them with the PSF of the observations. The two-dimensional gas distribution is assumed to be a circular disk. We find that the intrinsic surface brightness of a disk is well fitted by a double exponential profile

$$\mathrm{I(r) = I_0 e^{-r/r_0} + I_1 e^{-r/r_1}}, \tag{4.2}$$

where $\mathrm{r_0}$ and $\mathrm{r_1}$ are the scale radii, and $\mathrm{I_0}$ and $\mathrm{I_1}$ are the scale factors for the two components. This parametrisation was also used in Marconi et al. (2001). Since the observed emission line surface brightness along the slit at different position angles depends on the inclination of the circular gas disk (with respect to the observer) as well as on the PSF we fit the intrinsic emission-line fluxes for a median disk inclination of 45° given the observational setup and conditions. The projected major axis of the [FeII] disk is at P.A.=$32{.}^{\circ}5$ (Marconi et al., 2000) and gets the highest weight in the fit, since the surface brightness along the major axis

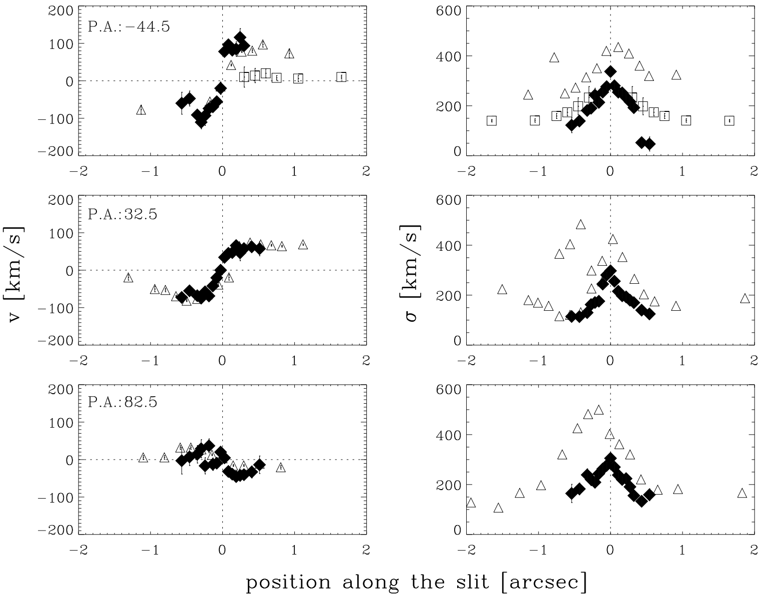

Figure 4.7 Comparison between the spatial resolution of the NaCo data (filled diamonds), the ISAAC data (open triangles) (Marconi et al., 2001), and the GNIRS data (open squares) (Silge et al., 2005). The NaCo and ISAAC data correspond to gas kinematics while the GNIRS data to stellar kinematics. In the left panel the rotational velocity is shown and in the right the velocity dispersion.

stays unchanged when the disk is inclined. The parameters that after PSF convolution best fit the surface brightness distribution along the different slit positions are I_1/I_0=0.018, r_0=0.″02, and r_1=0.″22. This parametrisation for the disk surface brightness is used in the dynamical models at all inclination angles. Compared to the fit values in Marconi et al. (2001) our scale radii are smaller due to higher spatial resolution. Given the shape of the [FeII] emission from the HST narrow-band image (Marconi et al., 2000), the axis ratio of a possible gas disk is ∼1:2 which corresponds to an inclination angle of 60°, given a circular disk structure. However, as found before by Marconi et al. (2001) there is a mismatch between the photometric major axis of the [FeII] gas disk and its kinematical major axis (line-of-nodes), which they find to lie between $-10° > \zeta > -14°$.

4.4 Dynamical model

In this section we outline the models describing the motions of the ionised gas in the combined gravitational potential of the (putative) central black hole and the stars. This modeling also requires a careful discussion of the gas geometry, as well as the physical state of the ionised gas, whose measured velocity dispersion far exceeds the expected thermal broadening.

4.4.1 The stellar mass model

The first step in the dynamical modeling is to estimate the stellar contribution to the central potential from the stellar surface density. For the deprojection of the observed surface brightness distribution into the stellar luminosity density we applied the Multi-Gaussian expansion (MGE) method (Monnet et al., 1992; Emsellem et al., 1994). Specifically, we obtained an MGE fit to a composite set of 2-dimensional K-band images using the method and software of Cappellari (2002). The MGE fit was performed using the NaCo K-band image ($0'' < r < 7''$), the NICMOS F222M image (Schreier et al., 1998) ($2'' < r < 16''$), and the 2MASS Large galaxy atlas (LGA) K-band image (Jarrett et al., 2003) for larger radii ($8'' < r < 365''$).
The sky-subtraction was performed relative to the 2MASS LGA image, which is taken to be the sky-clean reference. The flux calibration of the NaCo and NICMOS data is also referenced to the 2MASS image.

To get a parametrisation of the NaCo K-band PSF we fit a full MGE model to the composite image of NGC 5128 (without giving the code a prior PSF estimate). We then selected the central four Gaussian components, that clearly described the unresolved nucleus, as the PSF. Its parametrisation is

$$\mathrm{PSF(R)} = \sum_{\mathrm{i=1}}^{\mathrm{N}} \mathrm{G_i} \exp[-\mathrm{R}^2/(2\sigma_{\mathrm{i}}^{*2})]/(2\pi\sigma_{\mathrm{i}}^{*2}), \tag{4.3}$$

and the numerical values of the relative weights G_i (normalised such that $\sum_{i=1}^{N} G_i = 1$) and of the dispersions σ_i^* are given in Table 4.2. This PSF was then fixed in the MGE fit to the composite image, where we neglected PSF convolution of the NICMOS and 2MASS images since these are only used at radii $r > 2''$ and the NaCo image has a much higher resolution.

Table 4.2 MGE PSF parametrisation

i	G_i	σ_i^*	FWHM_i^*
1.....	0.0004	$0''.005$	$0''.012$
2.....	0.1590	$0''.031$	$0''.074$
3.....	0.3034	$0''.062$	$0''.145$
4.....	0.5372	$0''.143$	$0''.336$

Figure 4.8 shows a comparison between the observed photometry and the MGE model along four different position angles in the galaxy, while Table 4.3 gives the corresponding numerical values of the analytically deconvolved MGE parametri-

sation of the galaxy surface brightness

$$\Sigma(x', y') = \sum_{i=1}^{N} \frac{L_i}{2\pi\sigma_i^2 q_i'} \exp\left[-\frac{1}{2\sigma_i^2}\left(x'^2 + \frac{y'^2}{q_i'^2}\right)\right], \tag{4.4}$$

where $(x^{'}, y^{'})$ are the coordinates on the plane of the sky and N is the number of the adopted Gaussian components, having total luminosity L_i , dispersion σ_i, and observed axial ratio $0.8 \leq q_i^{'} \leq 1.0$. In Table 4.3 the central unresolved component (which we attribute to the AGN) is removed. We only account for the stellar light distribution in the Multi-Gaussian expansion model.

Table 4.3 MGE parametrisation of the deconvolved K-band surface brightness of Cen A

i	L_i $[\times 10^9 L_{\odot,K}]$	σ_i	$q_i^{'}$
1.....	0.113	0.″45	0.882
2.....	0.297	1.″48	0.812
3.....	1.13	3.″27	1.000
4.....	1.25	6.″68	1.000
5.....	5.07	14.″3	0.879
6.....	15.5	38.″0	1.000
7.....	19.6	78.″6	1.000
8.....	23.7	130.″9	0.807
9.....	5.24	365.″8	0.800

Using this radial profile of K-band (volume) emissivity, we fix the stellar mass-to-light ratio by constructing an isotropic spherical Jeans model and matching it over the radial range $3'' < r < 10''$ to the stellar kinematics ($\sqrt{v_*^2 + \sigma_*^2}$) published recently by Silge et al. (2005). The innermost $3''$ are excluded from the fit to minimise the influence of the black hole. We find a best-fitting central mass-to-light ratio $\mathrm{M/L_K} = (0.72 \pm 0.04)$ $\mathrm{M_\odot/L_\odot}$ in agreement with the best-fitting model of Silge et al. (2005). This agreement of the mass-to-light ratio from Schwarzschild and Jeans modeling is supported by the recent work of Cappellari et al. (2006).

4.4.2 Geometry and kinematics of the [FeII] gas

The central [FeII] velocity curves (Figure 4.6) suggest that we see gas rotating in a flattened geometry around a central mass concentration, presumably dominated by a black hole. The velocity dispersion in the very center is quite high (~300 km s^{-1} in the central pixel), well in excess of the mean rotation seen. In part this high dispersion may be attributed to rapid but spatially unresolved rotation.

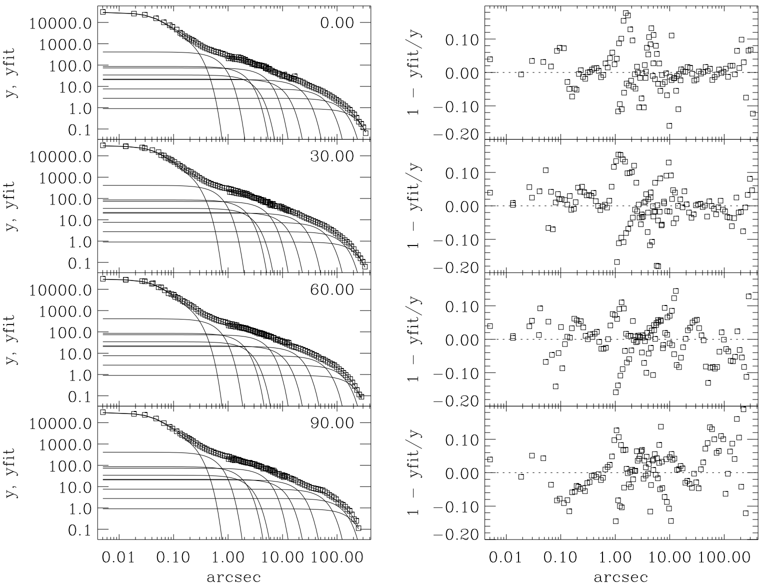

Figure 4.8 Comparison between the NaCo ($0'' < R < 7''$), NICMOS ($2'' < R < 16''$), and 2MASS LGA ($8'' < R < 365''$) K-band surface brightness (open squares) of Centaurus A and the corresponding best-fit MGE model (solid line) as a function of radius R. On the left the MGE fit is shown for inclination angles between 0° and 90°, while the right panels show the corresponding residuals.

As the underlying physical origin of the observed high gas dispersion is not clear a priori, we consider at least three geometric models:

1. the gas lies in a geometrically thin, kinematically cold disk and is in Keplerian motion around the black hole,
2. the gas forms a geometrically thin, kinematically hot disk that is in radial hydrostatic equilibrium,
3. the gas lies in a spherical distribution of collisionless cloudlets and can be modeled through Jeans equation.

Note that cases 1. and 3. are extreme physical assumptions and we consider them as limiting cases. In all three cases the gas is moving in the combined potential of the surrounding stars and of the central black hole; the self gravity of the gas is negligible (given the estimated mass of the ionised gas is $\sim 10^3 \mathrm{M}_\odot$ (Marconi et al., 2001) and the mass of the innermost Gaussian representing the stars is already $\sim 8 \times 10^7 \mathrm{M}_\odot$ (see Table 4.3)). The underlying stellar mass distribution is the same in all models, with M/L fixed by the stellar kinematics at larger radii (see previous section).

The mismatch between the kinematical and photometric major axis of the gas disk, found before by Marconi et al. (2001) introduces a degeneracy between the inclination angle (i) of the gas disk and the position of its line-of-nodes (ζ). We fear that our long-slit data will not be sufficient to constrain both i and ζ. We therefore make use of the inclination angle of the radio jet which sets the lower limit of the disk inclination in the standard picture of an orthogonal disk-jet geometry. Tingay et al. (1998) derived a value of $50^\circ < i < 80^\circ$. Given this prior information, we set up our thin disk models.

4.4.3 Model 1: Thin cold disk model

We follow the widely used approach (e.g. Macchetto et al., 1997) which assumes the gas to lie in a thin disk around the black hole, moving on circular orbits; its observed velocity dispersion is assumed to be solely due to rotation. We constructed a model using the IDL software developed in Cappellari et al. (2002). This modeling can deal with multiple component PSFs, different PSFs for different data-subsets, and a general gas surface brightness distribution. Pixel binning and slit effects are taken into account to generate a two-dimensional model spectrum with the same pixel scale as the observations. Like in the data analysis, the rotational velocity and velocity dispersion is determined by fitting simple Gaussians to each row of the model spectrum. We make no velocity offset correction (van der Marel et al., 1997; Maciejewski and Binney, 2001; Barth et al., 2001), since the slit width ($0\farcs086$) is comparable to the FWHM of the PSF.

The predicted velocity and velocity dispersion profiles of this model depend on the intrinsic surface brightness distribution of the emission lines, the PSF, plus the following parameters:

1. the inclination, i, of the gas disk ($i = 0^\circ$ is face-on, 90° edge-on)
2. the angle between the projected major axis of the disk (line of nodes), ζ, and the slit positions
3. the black hole mass, M_{BH}; the stellar mass profile is fixed.

We describe the 'intrinsic velocity dispersion' of the gas in the model by a double exponential parametrisation of the form

$$\sigma_R = \sigma_0 e^{-r/r_0}(1 + \epsilon e^{-r/r_1}), \tag{4.5}$$

without using it in the dynamics. The parameters σ_0, ϵ, r_0, and r_1 are fixed through comparison of the observed dispersion profile to a flux-weighted convolution of the intrinsic velocity dispersion profile with the PSF and the size of the aperture. The parameters that give a good fit to the velocity dispersion at all slit positions in the cold disk model are, σ_0=140 km s^{-1} , $\epsilon \simeq 0.25$, $r_0 = 0\farcs9$, and $r_1 = 0\farcs2$. We do not know the source for this high velocity dispersion and simply ignore it in the kinematically cold disk model. To reduce the number of free parameters in the model we evaluate the rotation curves for three fixed inclinations (45°, 60°, and 70°) and fixed the intrinsic surface brightness density of the gas disk beforehand (cf. Section 4.3.3).

In Table 4.4 we give the best-fitting black hole masses for each inclination angle individually; we also give the resulting χ^2 values to get the overall best-fitting model. The 1σ, 2σ, and 3σ contours are shown in Figure 4.9 for the two degrees of freedom, black hole mass and line-of-nodes. The three sets of contours correspond to the relevant inclination angles of the gas disk (i=45°,60°, and 70°) where the best-fitting inclination angle, i=45°, is indicated by a solid line.

Table 4.4 Best fit values - cold disk model

i	M_{BH} [$M_\odot$]	ζ	χ^2_{tot}
45°	$(4.0 \pm 0.2) \times 10^7$	$-27° \pm 4°$	46.1
60°	$(3.2 \pm 0.2) \times 10^7$	$-28° \pm 4°$	47.1
70°	$(3.2 \pm 0.1) \times 10^7$	$-36° \pm 2°$	47.1

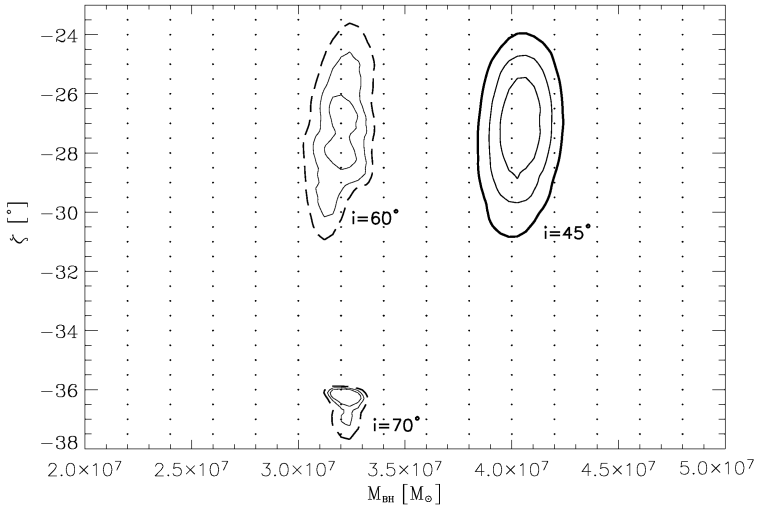

Figure 4.9 Fitting a cold gas disk: the χ^2 contours are shown for the two parameter fit of black hole mass vs. projected major axis ζ for the three inclination angles. The best cold model is at an inclination angle of 45° and the corresponding contours are plotted in solid lines. The best-fitting values are $\zeta = -27° \pm 4°$ and $M_{BH} = (4.0 \pm 0.2) \times 10^7 M_\odot$. The three contours give the formal 68.3%, 95.4%, and 99.73% (thick) confidence levels.

The overall best-fitting cold gas model is obtained at an inclination angle of 45°. Figure 4.10 shows the observational data in comparison to the model. The parametrisation of the surface brightness, shown in the third row, is fixed beforehand and not included in the fit here (compare Section 4.3.3). The parameters that lead to this fit are $\zeta = -27°$ and $M_{BH} = 4.0 \times 10^7 M_\odot$.
However, the minimum χ^2 values are comparable for all three cases, i.e. their

differences are smaller than the 1σ level, and we therefore cannot constrain the inclination angle of the gas disk with our long-slit data. We conclude that the black hole mass for a dynamically cold, geometrically thin disk model is $\mathrm{M_{BH}} = (4.0^{+0.2}_{-1.0}) \times 10^7 \mathrm{M}_\odot$.

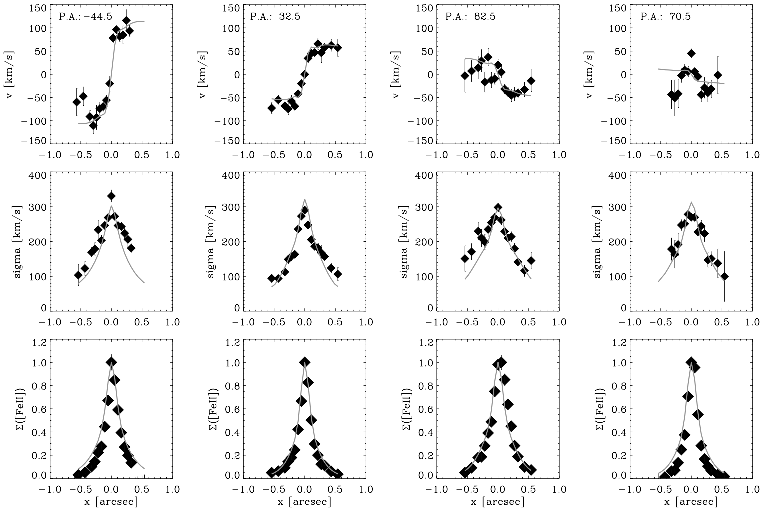

Figure 4.10 The observational data is shown in comparison to the best fitting cold disk model at 45° inclination angle. The best-fitting parameters are $\zeta = -27°$ and $\mathrm{M_{BH}} = 4.0 \times 10^7 \mathrm{M}_\odot$. The velocity dispersion as well as the surface brightness are parametrised by a double exponential function which were fixed beforehand and not fitted here.

4.4.4 Model 2: Thin hot disk model

This model is identical to the previous one except that we now interpret the 'intrinsic velocity dispersion' as a gas pressure component. As mentioned above, we do not know the physical origin of this high velocity dispersion of the gas, nevertheless, we include it in the dynamical analysis.

Any pressure support will require less rotation for dynamical equilibrium at a given black hole mass. In other words, the black hole mass needs to be larger to cause the same mean rotational velocity. The classic approach to account for velocity dispersion is to apply an asymmetric drift correction (e.g Barth et al. (2001)), but the approximate equations are only applicable if σ/v is small. However, in the case of Cen A, σ/v even exceeds unity and we therefore chose another approach: we assume the gas disk to be geometrically flat but with an isotropic pressure; on this basis we construct an axisymmetric Jeans model in hydrostatic equilibrium to model the observations.

We assume that the [FeII] surface brightness of the gas disk $\Sigma_g(x, y)$ reflects the tracer gas density $\rho_g(x, y)$, and that the gas moves in the joint potential Φ of the stars and the central black hole. The Jeans equation for this situation reads (Binney and Tremaine, 1987, Eq.4-64a):

$$\frac{R}{\rho_g}\frac{\partial(\rho_g\sigma_R^2)}{\partial R} + R\frac{\partial\Phi}{\partial R} = \overline{v_\Phi}^2, \tag{4.6}$$

where R is the projected radius, and σ_R and $\overline{v_\Phi}$ are the radial velocity dispersion and the azimuthal velocity of the gas, respectively, and both are functions of R.
We again parametrise the gas dispersion profile by a double exponential function of the form:

$$\sigma_R = \sigma_0 e^{-r/r_0}(1 + \epsilon e^{-r/r_1}), \tag{4.7}$$

and we fit for the best set of parameters (σ_0=140 km s^{-1}, $\epsilon \simeq 0.25$, $r_0 = 0\farcs9$, and $r_1 = 0\farcs2$) to get the intrinsic dispersion profile.
The assumption that the gas disk is infinitesimally thin does most probably not reflect the real physical properties but was chosen to eliminate line-of-sight integrations through a 3-dimensional gas distribution.
Table 4.5 summarises the best fit parameters and the corresponding χ^2 values for the different inclination angles of the 'hot' gas disk model. The 1σ, 2σ, and 3σ contours are plotted in Figure 4.12.

Table 4.5 Best fit values - hot disk model

i	M_{BH} [$M_\odot$]	ζ	χ^2_{tot}
45°	$(6.1 \pm 0.3) \times 10^7$	$-27° \pm 3°$	52.1
60°	$(5.6 \pm 0.3) \times 10^7$	$-25° \pm 2°$	54.0
70°	$(6.4 \pm 0.3) \times 10^7$	$-25° \pm 2°$	53.7

The best-fitting hot disk model favors a black hole mass of $M_{BH} = (6.1 \pm 0.3) \times 10^7 M_\odot$ and $\zeta = -27° \pm 3°$, at an inclination angle of 45°. It is shown in Figure 4.11 for comparison. The increased total χ^2 value (compared to the cold disk model) can be explained by the reduced number of degrees of freedom, since in the hot disk model the velocity dispersion and the rotational velocity are coupled through Jeans equation. However, the difference between the two fits is small ($< 2\sigma$ confidence level) and the large velocity dispersion lead us to consider this model a better description of the physical properties at the center of Centaurus A.

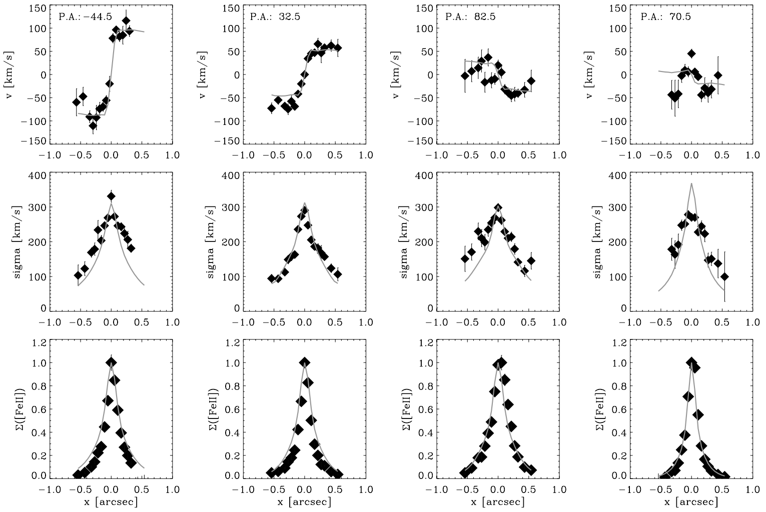

Figure 4.11 The best-fitting hot disk model with parameters $\zeta = -27°$ and $\mathrm{M_{BH}} = 6.1 \times 10^7 \mathrm{M}_\odot$. In this model, v and σ are interwined through Jeans equation. Note that despite the higher black hole mass (compared to the cold disk model), the model curves drop beyond $0\farcs3$ and match the observed data better. The model of the surface brightness is fixed beforehand and not fitted here.

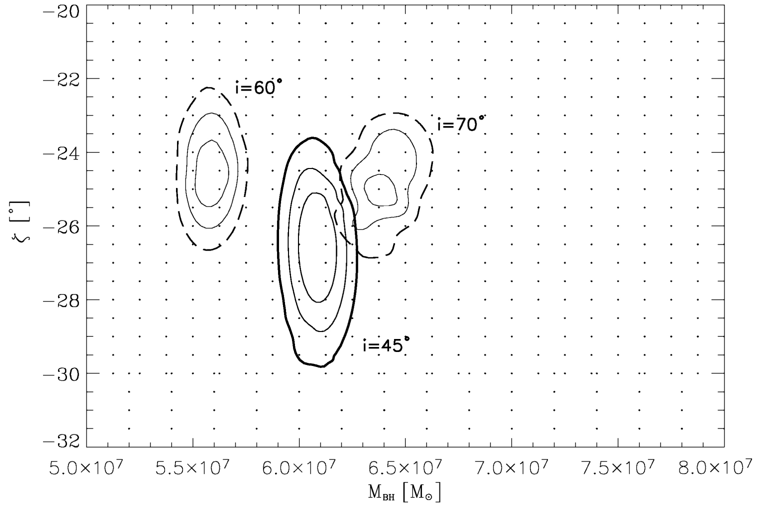

Figure 4.12 Fitting the 'hot' gas disk: the χ^2 contours are shown for the two parameter fit of black hole mass vs. projected major axis ζ for the three inclination angles. The best hot model is at an inclination angle of 45° and the corresponding contours are plotted in solid lines. The best fitting values are $\zeta = -27° \pm 3°$ and $\mathrm{M_{BH}} = (6.1 \pm 0.3) \times 10^7 \mathrm{M}_\odot$. The three contours give the formal 68.3%, 95.4%, and 99.73% (thick) confidence levels.

4.4.5 Model 3: Spherical Jeans model

In this final modeling approach, we account for the fact that the high gas velocity dispersion is not consistent with the assumption of a thin disk. Alternatively, we assume the gas spherically symmetric distributed in individual clouds that move ballistically (i.e. $\mathrm{t_{coll}} >> \mathrm{t_{dyn}}$). Given the observational facts (rotation curves along certain slit positions, gas disk observed by Marconi et al. 2000), this model is not very likely to describe the physical properties of the central region in Cen A. However, it gives an upper limit on the black hole mass, compared with disk models at non-extreme inclinations, and is implemented fairly easily. We construct a spherical Jeans model where we assume the following:

1. the gas density is given by its emissivity
2. the gas cloud distribution is spherical
3. the gas clouds move in the potential given by the stars and the possible central black hole
4. the stellar mass-to-light-ratio is constant throughout the relevant range ($\mathrm{R} < 2''$)
5. the stars are in spherical symmetry.

Here, we construct a model with a Multi-Gaussian-expansion both for the stellar photometry and for the gas distribution. The gas surface brightness is given by the HST [FeII] narrow band image (Marconi et al., 2000) and fitted by an MGE model.

Following Tremaine et al. (1994) in the spherical case the solution of Jeans equation for the projected rms velocity reduces to

$$(\mathrm{v}^2 + \sigma^2)_\mathrm{p}(\mathrm{R}) = \frac{2\mathrm{G}}{\Upsilon \Sigma_\mathrm{g}(\mathrm{R})} \int_\mathrm{R}^\infty \frac{\rho_\mathrm{g}(\mathrm{r}) \mathrm{M_{tot}}(\mathrm{r})}{\mathrm{r}^2} (\mathrm{r}^2 - \mathrm{R}^2)^{1/2} \mathrm{dr}, \tag{4.8}$$

where Υ is the stellar mass-to-light ratio, $\Sigma_g(R)$ is the surface brightness of the gas, $\rho_g(r)$ is the density of the gas and $M_{tot}(r)$ is the mass of the stellar body and the central dark object.

Again, the stellar mass-to-light ratio is fixed at a value of $\Upsilon = 0.72 \mathrm{M}_\odot/\mathrm{L}_\odot$, that we derived in section 4.4.1. The best fitting black hole mass that we find with the spherical Jeans model is $(1.0 \pm 0.5) \times 10^8 \mathrm{M}_\odot$. The comparison between the measured and the modelled rms velocity ($\sqrt{v^2 + \sigma^2}$) is shown in Figure 4.13.

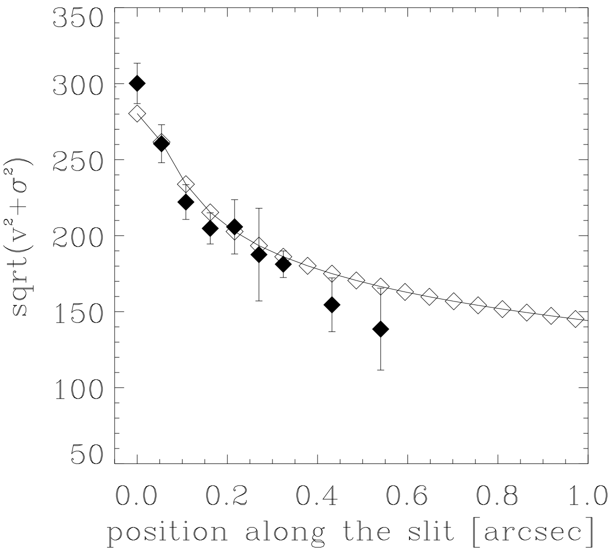

Figure 4.13 Comparison between the measured rms velocity (filled diamonds) and the spherical Jeans model (open diamonds) for the gas. The best fitting black hole mass is $M_{BH} = (1.0 \pm 0.5) \times 10^8 M_{\odot}$.

4.5 Discussion

The availability of adaptive optics instrumentation opens up new realms of ground based observations. Drawing on kinematic data with unprecedented spatial resolution we present a dynamical model of the black hole in the nucleus of Centaurus A. The spatial resolution that we reach in our H-band spectra is $0\farcs11$ (= 1.8 pc at a distance of 3.5 Mpc) that is a factor of 3 to 4 higher than from the previous ground based observations with ISAAC by Marconi et al. (2001). At large radii ($> 0\farcs3$) our data are in agreement with their gas kinematical data, but our high resolution data reveals the steep gradient of the rotation curve in much more detail (see e.g. Figure 4.6). The rotation curves show a smooth behavior and the slit position that shows the fastest rotation (P.A.$=-44\fdg5$) is nearly perpendicular to the jet direction (P.A.$\sim 51^\circ$). This suggests the picture of gas orbiting in a flattened geometry (presumably a disk) around the central black hole, with the jet pointed along the disk angular momentum vector.

4.5.1 Black hole mass

In this paper we present three different dynamical modeling approaches to describe the gas kinematics in the central $\sim 2'' \simeq 33$pc of NGC 5128. Two of the models are clearly conceptually inconsistent with the data, either neglecting the dominant velocity dispersion of the gas (Model 1; cold disk), or the disk-like geometry of the velocity field (Model 3; isotropic, spherical Jeans). We have laid out these extreme models as limiting cases, which would result in a broad mass range, $2.7 \times 10^7 \mathrm{M}_\odot < \mathrm{M}_{\mathrm{BH}} < 1.5 \times 10^8 \mathrm{M}_\odot$, and to demonstrate how important the gas physics is, even in light of high resolution data. Our physically most plausible model is a hot disk model at an inclination angle of 45°; the corresponding black hole mass is $\mathrm{M}_{\mathrm{BH}} = 6.1^{+0.6}_{-0.8} \times 10^7 \mathrm{M}_\odot$ with a line-of-nodes at $\zeta = -27^\circ \pm 4^\circ$. We consider this model the best-fitting since it accounts for the high velocity dispersion of the gas combined with a disk-like gas structure, as suggested by the smooth rotation curves. The assumption of a geometrically thin disk is not physically motivated but was chosen to eliminate line-of-sight integrations through an underconstrained 3-dimensional gas distribution.

Our disk model meshes well with other constraints on the central geometry of NGC 5128: e.g. Tingay et al. (1998) derived a jet position angle of $\sim 51^\circ$. If we assume that the accretion disk and surrounding gas disk is at right angles, we would expect its line-of-nodes to be at $\sim -39^\circ$. Moreover, from the direction of the jet and counter-jet they derived a value for the jet inclination of $50^\circ < i < 80^\circ$ with respect to the line-of-sight. Our best-fitting inclination angle of 45° is close to their lower value, but our long-slit data do not tightly constrain the inclination angle. This was also the main source of uncertainty for the black hole mass in the previous study by Marconi et al. (2001). If we were to consider a gas disk inclination to be as face-on as 25° (inconsistent with the jet inclination), the black hole mass would increase to $\sim 1.2 \times 10^8 \mathrm{M}_\odot$ in the hot disk case.

The unsettled question of inclination will presumably be solved with the analysis of integral field spectroscopy data taken with SINFONI at the VLT. The full 2-D velocity field data provide an excellent means of modelling black hole masses from gas as well as stellar kinematics.

Our best-fit value for the line-of-nodes is only $\sim 12°$ away from the 'expected' value of $\sim -39°$, much closer than the value derived by Marconi et al. (2001), $-10° > \zeta > -14°$. Nonetheless, this confirms that the kinematical line-of-nodes does not coincide with the projected major axis of the gas disk (P.A.$\simeq 33°$) seen in Paα and [FeII] with NICMOS (Schreier et al., 1998; Marconi et al., 2000).
The value that we derived for the black hole mass from the best-fitting hot disk model ($6.1^{+0.6}_{-0.8} \times 10^7 \mathrm{M}_\odot$) is significantly lower than the values both from stellar kinematics presented by Silge et al. (2005) ($\mathrm{M_{BH}} = 1.8^{+0.4}_{-0.4} \times 10^8 \mathrm{M}_\odot$ for i=45°) and the previous gas kinematical study of Marconi et al. (2001) ($\mathrm{M_{BH}} = 2.0^{+3.0}_{-1.4} \times 10^8 \mathrm{M}_\odot$) obtained at 3-4 times lower resolution. This decrease in black hole mass estimate with higher resolution data is in line with the decrease in derived black hole masses when HST data became available. Our limiting case model of a spherical gas distribution modeled through Jeans equation gives a black hole mass of $\mathrm{M_{BH}} = (1.0 \pm 0.5) \times 10^8 \mathrm{M}_\odot$ which agrees both with Silge et al. (2005) and Marconi et al. (2001). However, in their gas dynamical model Marconi et al. (2001) assumed a cold thin disk and did not account for the pressure support of the gas; assuming a cold disk model, we find the best-fitting black hole mass to be $\mathrm{M_{BH}} = (4.0^{+0.2}_{-1.0}) \times 10^7 \mathrm{M}_\odot$, which is almost a factor of 7 lower than their value.

4.5.2 Relation of black hole mass versus galaxy properties

This confirmation of a fairly high black hole mass compared to a fairly low stellar velocity dispersion of $\sigma_* = 138$ km s^{-1} (Silge et al., 2005) quantitatively reduces but qualitatively confirms the offset of Centaurus A from the $\mathrm{M_{BH}}$-σ relation (Ferrarese and Merritt, 2000; Gebhardt et al., 2000). The black hole mass predicted by this relation would be around $3 \times 10^7 \mathrm{M}_\odot$ and our best-fitting black hole mass lies a factor of ~ 2 above this. This offset is close to the observed scatter of the $\mathrm{M_{BH}}$-σ which is a factor of 1.5 (0.2dex) (Ferrarese and Merritt, 2000; Gebhardt et al., 2000). In the case of the lowest black hole mass supported by our cold disk model ($\mathrm{M_{BH}} = (4.0^{+0.2}_{-1.0}) \times 10^7 \mathrm{M}_\odot$) the black hole falls nicely onto this relation.
To compare the black hole mass to the bulge mass of Centaurus A, we applied a spherical Jeans model to the whole galaxy as seen in K-band, using the stellar kinematics (v_* and σ_*) of Silge et al. (2005) out to $\sim 100''$ and derived a total mass of the spheroid of $\mathrm{M_{sph}} = (6.5 \pm 3.) \times 10^{10} \mathrm{M}_\odot$. This mass is in agreement with

the virial bulge mass estimate by Marconi et al. (2003), but somewhat lower than the mass derived by Hui et al. (1993) and Mathieu and Dejonghe (1999). Given this spheroid mass, Cen A is in excellent agreement with the M_{BH}-M_{Bulge} relation (e.g. Häring and Rix, 2004). Taking the larger spheroid masses for granted, Cen A tends to lie below the relation of black hole mass to bulge mass, i.e. it has a fairly high bulge mass compared to its black hole mass, without being a dramatic outlier to this relation.

Taken together, it seems that Cen A foremost has a very high M_{sph}/σ_* ratio among ellipticals (which implies a very low concentration), rather than being an outlier in the relations to M_{BH}. This low concentration may be explained by the fact that Cen A is known to be a $z \simeq 0$ merger (Israel, 1998).

This paper demonstrates that near-IR adaptive optics instrumentation provide excellent data and make it possible to explore the central regions of dust enshrouded galaxies. With a spatial resolution of $\sim 0\farcs06$ in K-band and $\sim 0\farcs11$ in H-band we are now able to resolve the radius of influence of black holes even in more distant galaxies from the ground.

5. SINFONI on the central gas kinematics in Cen A[1]

5.1 Introduction

The mass of the black hole at the centre of NGC 5128 (Centaurus A), the most nearby elliptical galaxy, is still under debate. Recent stellar dynamical measurements and modelling by Silge et al. (2005) result in $1.8\times10^8 M_\odot$, while different gas-dynamical studies found masses in the range of $6.1 \times 10^7 M_\odot$ to $2 \times 10^8 M_\odot$ depending mainly on the inclination angle of the modelled gas disk (Marconi et al., 2001, 2006; Häring-Neumayer et al., 2006; Krajnović et al., 2006b). It is indeed one of the most studied galaxies, since its proximity making it a benchmark for direct black hole mass measurement from both stellar and gas dynamical models. With the availability of integral-field spectroscopy (IFS) in the near infrared (IR) the gas as well as the stars can be mapped in two dimensions even in dust-shrouded galaxy centres. Black hole masses can be derived separately from stars and gas from the same complete data set, and the gas geometry is constrained by two-dimensional data. The star and gas results can then be compared to assess the reliability of the modelling techniques. SINFONI (Eisenhauer et al., 2003b; Bonnet et al., 2004) at the Very Large Telescope (VLT) combines IFS with the resolving power of adaptive optics assisted observations and provides data at a spatial resolution of $\sim 0\farcs1$ in K-band. For Centaurus A (Cen A) the radius of influence of the black hole at the centre should be comfortably resolved.

For our dynamical model we assume a distance to NGC 5128 of 3.5 Mpc to be consistent with all previous mass determinations. Recent distance measurements are in the range 3.4 Mpc to 4.2 Mpc (Israel, 1998; Tonry et al., 2001; Rejkuba, 2004), with typical uncertainties of $\sim 8\%$.

This paper[1] is a follow-on to the work presented in Häring-Neumayer et al. (2006) (hereafter HN+06, or Chapter 4), using high spatial resolution Naos-Conica imaging and spectroscopy data to get an accurate measurement of Cen A's black hole mass.

Here, we study in detail the kinematics of different gas species at the centre of NGC 5128 in 2D. Unsurprisingly, different gas species exhibit different behaviours.

---

[1] Neumayer et al. 2007, to be submitted to ApJ

While the (highly) ionised gas shows (strong) influence by the jet (both in surface brightness and in the kinematic maps), the molecular gas (H_2) seems to "feel" only gravity. This is the reason why we focus on H_2 when we construct a dynamical model to measure the mass of the central supermassive black hole.
SINFONI stellar kinematics and black hole mass modelling will be presented in a separate paper (Cappellari et al., 2006) and complement the gas-dynamical study and black hole mass measurement presented here.

Section 2 describes the observations and the data reduction. Section 3 presents the gas morphology and kinematics and section 4 our dynamical model. The modelling results are given in section 5 and discussed in section 6.

5.2 Observations and data reduction

All observations presented here were taken with SINFONI (Eisenhauer et al., 2003b; Bonnet et al., 2004) on the VLT UT4 on March 23 and April 1, 2005. SINFONI consists of a cryogenic near-infrared integral field spectrometer SPIFFI (Eisenhauer et al., 2003b,a) coupled to the visible curvature adaptive optics (AO) system MACAO (Bonnet et al., 2003). For the Cen A nucleus, the SINFONI AO module was able to correct on a ~15mag star 40"NW of the nucleus in excellent seeing of $0\farcs5$, reaching nearly the diffraction limit of the telescope in the K band. With the appropriate pixel scale selected ($0\farcs05 \times 0\farcs1$ per pixel), the spectrograph was able to obtain spectra across the entire K band (approximately λ1.93-2.47μm) at a spectral resolution of R~4000 and covering a 3" × 3" field of view, in a single shot. A total of 10 sky (S) and 15 on-source (O) exposures of 900 s each followed a sequence OSOOSOO... and were dithered by only a few pixels to allow removal of bad pixels and cosmic rays. The frames were combined to make the final K band data cube with a total on-source exposure of 13500s.
In the same way, we obtained H-band data (λ1.43-1.87μm) with a slightly lower spectral resolution of R~3000 covering the central 3" × 3" with a scale of $0\farcs05 \times 0\farcs1$ per pixel. The overall integration time for H-band was 3600 s.

The data were reduced using the SINFONI data reduction pipeline provided by ESO. The nearest sky exposure was subtracted from the object frames, after which the data was flatfielded and corrected for bad pixels. Distortion correction was done based on the position of OH line edges in sky frames. The wavelength calibration was based on the nightsky OH lines in H-band and on OH lines and arc lamp frames in K-band. Using the slitlet positions derived from the sky frames and the obtained wavelength calibration a three-dimensional data cube were created from each object frame. Finally the slitlet positions were adjusted if necessary based on crosscorrelation with NaCo broadband images. After correcting for telluric features and flux calibration the data cubes were mosaicked together. The stars Hip079775 (B3III) and Hip68359 (B8V) were used both as telluric standards and flux calibrators.

5.2.1 Spatial resolution

To assess the spatial resolution of the data, the point-spread function (PSF) is estimated from the unresolved active galactic nucleus (AGN), as discussed in more detail by HN+06. No additional PSF calibration frames using stars were taken, since the PSF in adaptive optics observations depends on several factors such as atmospheric conditions, brightness of the guide star, contrast of the guide star to the background, and these conditions are difficult to duplicate for the science and calibration observations. The most accurate measure of the science frame PSF in the vicinity of the AGN is therefore achieved directly on the unresolved nucleus.

We describe the normalised PSF empirically by a sum of two Gaussian components; one narrow component describing the corrected PSF core (σ_c) and one broader component (σ_s) which can be attribute to the seeing halo plus extended emission:

$$\mathrm{PSF(r)} = \frac{\mathrm{F}}{2\pi\sigma_\mathrm{c}^2}\mathrm{e}^{-\mathrm{r}^2/2\sigma_\mathrm{c}^2} + \frac{(1-\mathrm{F})}{2\pi\sigma_\mathrm{s}^2}\mathrm{e}^{-\mathrm{r}^2/2\sigma_\mathrm{s}^2}, \tag{5.1}$$

where F is the ratio of the flux of the narrow component and the total flux of the PSF ($\mathrm{F} = \mathrm{flux}_\mathrm{c}/\mathrm{flux}_\mathrm{total}$). The quantity F provides a rough approximation of the Strehl ratio (S) which gives the quality of an optical system; S is defined as the observed peak flux divided by the theoretically expected peak flux of the Airy disk for the optical system ($\mathrm{S} = \mathrm{peakflux}_\mathrm{c}/\mathrm{peakflux}_\mathrm{Airy}$). For the following analysis it is sufficient to measure the quantity F, which also gives an estimate of the quality of the adaptive optics correction.

For the K-band cube, a PSF model of the above form is fitted to the peak in surface brightness in the collapsed wavelength range of $\lambda 2.00$ to $2.10\ \mu$m (just next to the H_2 line). The two components of the PSF model shown in comparison to the data in Fig. 5.1 have a full width at half maximum (FWHM) of $0\farcs12$ and $0\farcs30$, for the narrow and broad component respectively. The width of the broad component compares well to the FWHM of the seeing disk as measured by the seeing monitor during the observations ($\mathrm{FWHM}_V \lesssim 0\farcs5$ transformed to K-band as in HN+06, $\mathrm{FWHM}_K \lesssim 0\farcs38$).

5.2.2 Subtraction of the stellar and non-stellar continuum

The total or averaged spectrum of the central $0\farcs8 \times 0\farcs8$ of Cen A (Fig. 5.2) shows strong CO absorption lines at $\lambda 2.3 - 2.4\,\mu$m indicating the stellar continuum. We use the penalised pixel fitting method (pPXF) Cappellari and Emsellem (2004) to fit the stellar continuum with a set of stellar templates. As template stars serve six late type stars that were observed with SINFONI in the same setup that we used for the nucleus of Cen A. This ensures that the instrumental spectral broadening is the same for the template stars and the galaxy spectrum, and we need not know the underlying instrumental line profile.

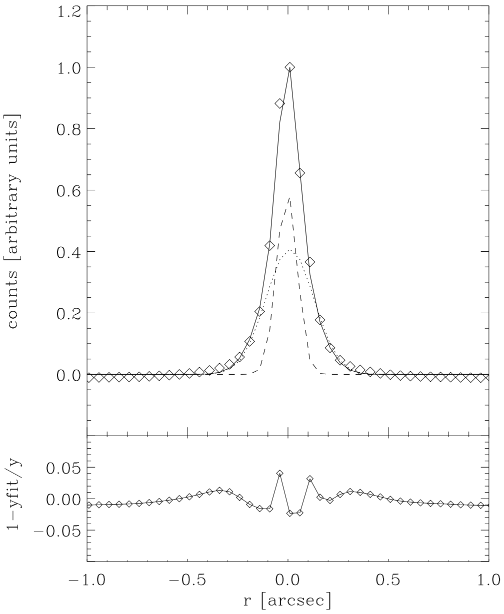

Figure 5.1 Double Gaussian fit of the K-band SINFONI PSF on the continuum just next to the H_2 line, $\sigma_c = 0\farcs12$, $\sigma_s = 0\farcs3$, F=0.21 (see Section 5.2.1) for a definition of these quantities.

As possible template stars we chose the following: K3V, M0III, M0V, M4V, M5II, and M5III. The wavelength regions with emission lines were omitted from the fit and the optimal template was convolved with Gauss-Hermite expansions (van der Marel and Franx, 1993; Gerhard, 1993) up to h_4, minimising the difference between the galaxy spectrum and the template.

In addition to the stellar continuum, the non-stellar continuum is fitted via an additive Legendre polynomial of fourth order. This becomes important in the central region where the power-law continuum of the AGN dominates the flux distribution. After the subtraction of the stellar and non-stellar continuum we are left with a data cube of pure emission line spectra.

5.2.3 Extraction of the gas emission lines

The SINFONI Cen A spectra in the wavelength range $\lambda 1.43$-1.87μm and $\lambda 1.93$-2.47μm (the H- and K-band, respectively) exhibit a wealth of gas emission lines. High excitation lines such as [Si VI] and [Ca VIII], ionised gas emission lines ([Fe II], Brγ, [He I]), and several transitions of molecular hydrogen H_2 (Figure 5.2). In this paper we focus on the kinematic properties of some of the gas emission lines and show that they have quite different kinematics. While the high-excitation lines appear to be affected, or created, by Cen A's jet, the H_2 gas appears to be solely rotating. We construct a dynamical model to explain the kinematics of the strongest line of molecular hydrogen 1-0 S(1) H_2 at $\lambda = 2.122\,\mu$m and use this to

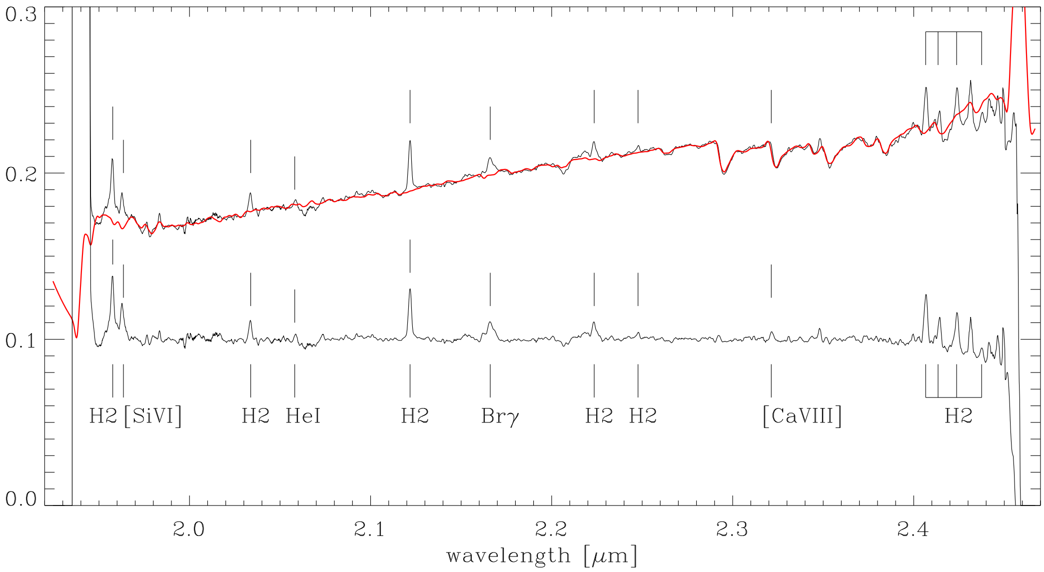

Figure 5.2 Total spectrum of the nucleus of Cen A in a square aperture of 0.″8 × 0.″8. The best-fit template composition is overplotted in red. The residual, or pure emission spectrum, is shown in the lower part. The gas emission lines are indicated. Note the strong CO absorption that is very well fitted by the stellar template.

measure the mass of the supermassive black hole at the centre of NGC 5128. Each gas emission line is fitted independently by a single Gaussian to derive its central wavelength, width and intensity. The fit is performed in IDL[2] using a non-linear least squares fit to the line and the errors are the 1-σ error estimates of the fit parameters.

To allow for the best possible extraction of the gas lines the extraction window is centred on the expected wavelength. Its width is optimised iteratively to fully cover the width of the line and to make sure the extraction window covers the same range on the left and right of the line peak. An initial estimate on the Gaussian fit parameters (amplitude, central position, and width) was derived from a smoothed spectrum at a central position in the velocity field, near the AGN, and applied as a starting value throughout the field.

We only consider the detection of the lines to be secure when their amplitude is a factor of 3 above the RMS scatter of the spectrum (A/N≥3). In this way we get an accurate fit to the lines over the entire field.

5.3 Gas measurements

From the parameters of the Gaussian fit - peak value, mean wavelength and width - we get the flux, the velocity and the velocity dispersion for each well-detected gas

---

[2] See http://www.rsinc.com

species in H- and K-band. Since the stellar and non-stellar continuum have been subtracted, the line-flux is directly measured as $\sqrt{2\pi}F_{\mathrm{peak}}\sigma$. For the velocity, we take the recession velocity of Cen A's stellar body ($v_{\mathrm{sys}} = 532 \pm 5$ km s^{-1} Marconi et al. 2001) as the reference and measure all line shifts with respect to this velocity.

5.3.1 Gas kinematics

Figures 5.3-5.6 show the maps of total flux, velocity, and velocity dispersion of the elements [Si VI], Brγ, [Fe II], and H_2. These line maps are presented to illustrate how the kinematics change when going from high- to low-excitation states. The highest excitation line, [Si VI], is dominated by a non-rotational component.
When comparing the velocity fields of [Si VI], [Fe II], and H_2, (middle panel in Figures 5.3-5.6) one notices that the velocity field of [Si VI] consists of two major components: rotational and translational motion. The velocity fields of [Fe II] and Brγ are dominated by rotation but are still distorted by a non-rotational component that is strongest to the lower right (south-west) of the field (blue component). These non-rotational motions in [Si VI], [Fe II], and Brγ are located close to the projected direction of the radio jet in Centaurus A (P.A.=51°Clarke et al. 1992; Tingay et al. 1998; Hardcastle et al. 2003). The measured values for the inclination angle of the jet vary between $50° < i < 80°$ (Tingay et al., 1998, from VLBI data) and $20° < i < 50°$ (Hardcastle et al., 2003, from VLA data), but without doubt the North-Eastern part is coming towards us. The direction of motion seen in [Si VI] (namely red-shifted in the jet and blue-shifted in the counter-jet) gives evidence for an inflow of material towards the nucleus.
This inflow motion could be associated with backflow of gas that was accelerated by Cen A's jet and after producing a bowshock is flowing back at the side of the jet cocoon. Although on much larger scales, this phenomenon is seen in jet simulations (e.g. Krause, 2005) and was proposed by Taylor et al. (1992) as a mechanism to produce the narrow line regions in Seyfert galaxies.

While the very high and medium ionisation lines [Si VI] and [Fe II] are kinematically strongly influenced by this jet induced motion, the velocity field of H_2 shows no distortion due to the jet. The rotation field is very smooth and symmetric. Striking is the twist of the major kinematic axis that is at a median P.A.=155°. However, the velocity fields in all gas species give evidence that at least part of the gas rotates in a nuclear gas disk. Moreover, the velocity dispersion maps of [Si VI], Brγ, [Fe II], and H_2 support the picture of an inclined nuclear gas disk. They all show disk-like structure in their high dispersion component, at a position angle of $125 \pm 25°$, and a declining dispersion profile outwards. The ionised gas species ([Si VI], [Fe II], and Brγ) show in addition a colder component (with $\sigma \sim 150$ km s^{-1}) that is elongated in the direction of the translational motion. H_2 has the lowest central velocity dispersion ($\sigma \sim 360$ km s^{-1}) and shows the most ordered structure both in the maps of velocity dispersion and mean velocity. Albeit the high velocity dispersion, it seems the molecular gas is well settled in a disk.

To visualise the difference in the velocity pattern of [Si VI] and H_2 Figure 5.7 shows the comparison of the H_2 and [Si VI] velocity fields (left and middle panel) masked with the [Si VI] flux map. The right panel shows the direct difference $v([\mathrm{Si\,VI}]) - v(\mathrm{H_2})$. Overplotted are the VLA contours of the radio jet (data kindly provided by M. Hardcastle). The non-rotational componenet of the [Si VI] velocity field becomes strongest SW of the nucleus, and can be identified with the innermost knot in the VLA radio jet. We clearly evidence jet-gas cloud interaction in the ionised gas species.

To compare the SINFONI 2D maps with the high-spatial resolution long-slit spectra presented in HN+06, we extracted velocity curves along the NaCo slit positions and overplot the NaCo data in Figure 5.8. The agreement is very good in most of the cases. The signal-to-noise ratio for the 70°.0 slit position in the NaCo observations is the lowest of the four P.A.s, and the seeing for the 82°.5 was the poorest. This might explain the deviation in the velocity curves at P.A.s 70°.0 and 82°.5.

5.3.2 Gas morphology

Looking at the flux maps of the gas species, one notices the very different morphologies in the high- and low-ionisation lines. The morphology of [Si VI] is dominated by an elongated structure that extends south-west of the nucleus, at a position angle of $\sim 33°$. This structure widens and ends in a blob or knot at $\sim 1" \simeq 17pc$ from the centre. The position of this knot is coincident with the innermost knot in the radio counterjet south-west of the nucleus (seen by Clarke et al. 1992 and denoted SJ1 by Hardcastle et al. 2003).

Overall, the morphology of Brγ and [Fe II] (Figures 5.4 and 5.5) resemble that of [Si VI] very closely, but overall the elongation is not as pronounced and the structure appears rounder.
For all gas species, the P.A. of the elongation is $\sim 33°$ which is the same as for the elongated structure detected in Paα by Schreier et al. (1998), that is centred on the nucleus and extended by $\pm 2"$. They interpret this as an inclined, ~40 pc diameter, thin nuclear disk of ionised gas rather than a jet-gas cloud interaction. However, our 2D data show that the gas moves along this elongated structure that extends around the jet axis. The direction of motion hints towards a backflow of jet material onto the accretion disk as mentioned above. While the major rotation axis is at a P.A.=155°.

In addition to this elongated structure, our high spatial resolution integral field data show evidence for a nuclear disk of ionised and molecular gas oriented ~perpendicular to the jet angular momentum vector. Looking at the central $0''.5 \times$

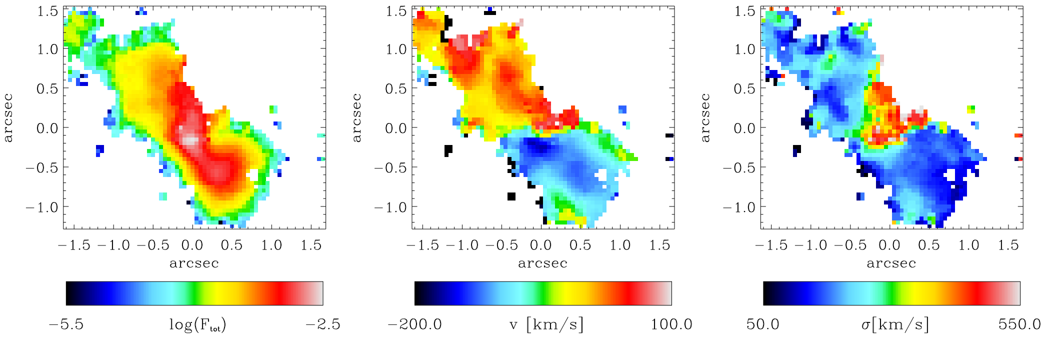

Figure 5.3 Flux, velocity, and velocity dispersion maps of [Si VI]. The flux map is in logarithmic scaling. The velocities and velocity dispersions are only plotted for the regions that are above the lower flux limit displayed in the left panel. The velocity dispersion is corrected for instrumental dispersion.

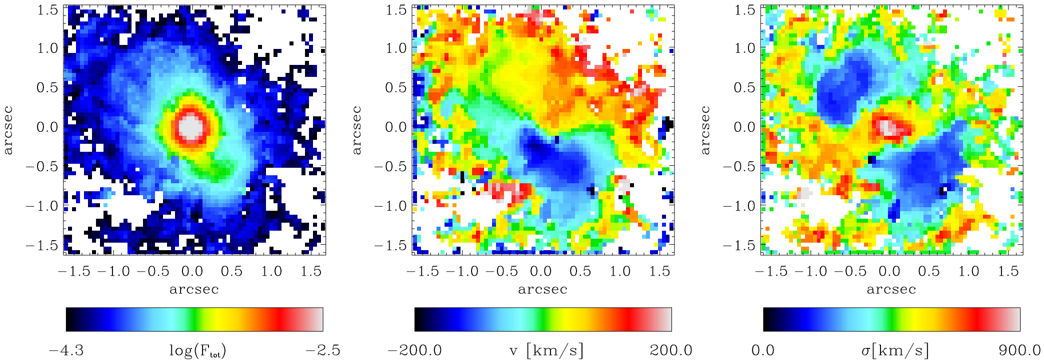

Figure 5.4 Flux, velocity, and velocity dispersion maps of Brγ. See caption of Fig. 5.3 for more details.

0″.5 of the H_2 flux map (Fig. 5.6), one notices a disk-like structure with a major axis of ∼ 140°. The same structure is visible in the Brγ and [Fe II] flux maps, although a bit rounder. Looking at the whole H_2 flux distribution, it appears very different from the ionised gas species, and the shells at the upper left and lower right are a dominant feature. These shells are reminiscent of the bowshock structures seen at larger scales in the outer regions of radio jets (e.g. Carilli et al., 1988, for Cyg A) and in smaller scales in Herbig-Haro objects (e.g. Reipurth et al., 2002). They are located at a (projected) position where the elongated structure in [Si VI], Brγ, and [Fe II] disappears. This is another hint towards the bowshock model of Taylor et al. (1992) where the shocked gas (here [Si VI], [Fe II], and Brγ) flows back towards the nuclear source along the shell.

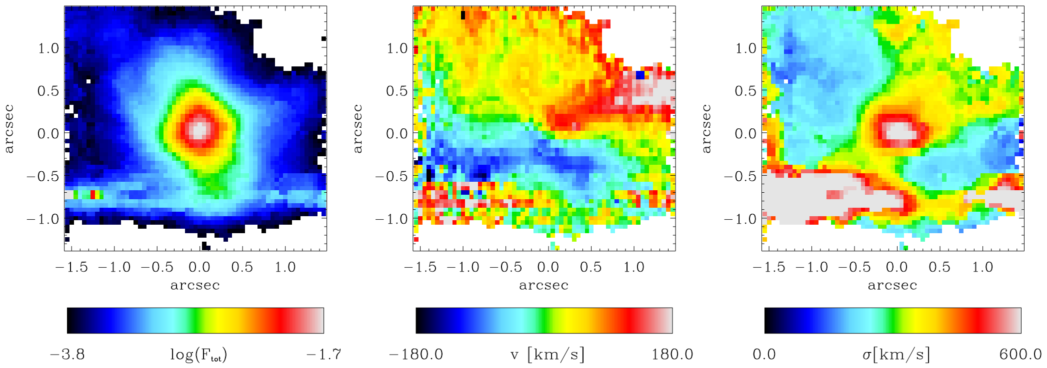

Figure 5.5 Flux, velocity, and velocity dispersion maps of [Fe II]. See caption of Fig. 5.3 for more details.

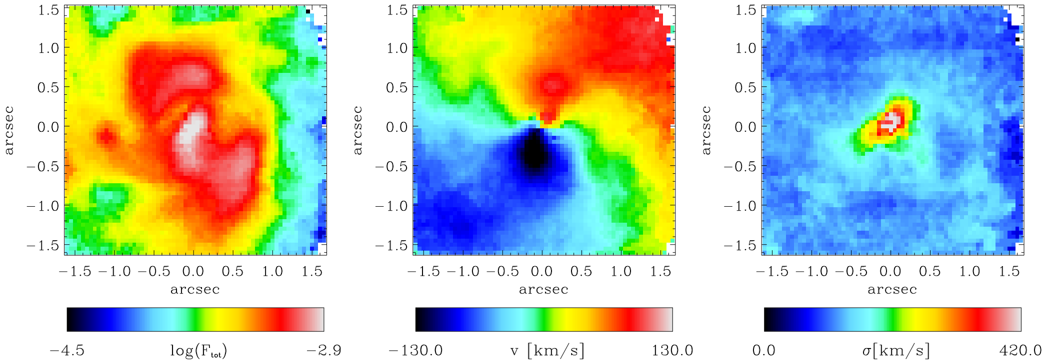

Figure 5.6 Flux, velocity, and velocity dispersion maps of H_2. See caption of Fig. 5.3 for more details.

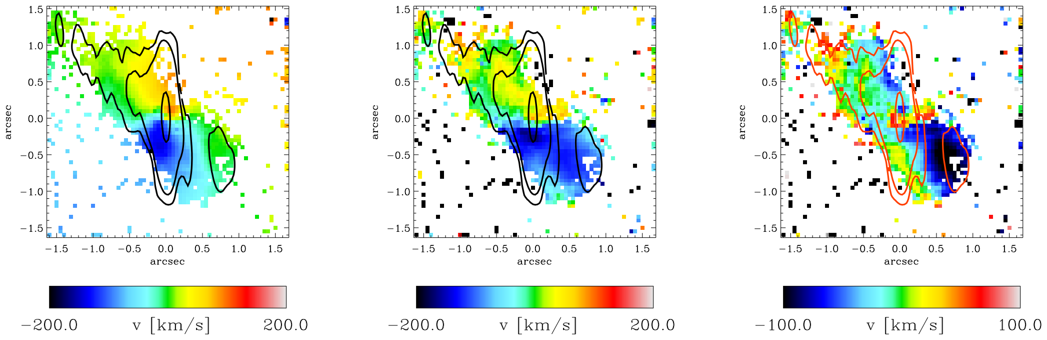

Figure 5.7 Comparison between the velocity fields of H_2 (left), [Si VI] (middle) and their difference (right), all masked with the [Si VI] flux map. The non-rotational velocity component in the [Si VI] velocity field becomes enhanced when subtracting the rotational motion (characterised as the H_2 velocity field). The blue component SW of the AGN marks the strongest translational velocity components. It matches the knot in the radio jet, overlain as contours (unpublished VLA data kindly provided by M. Hardcastle)

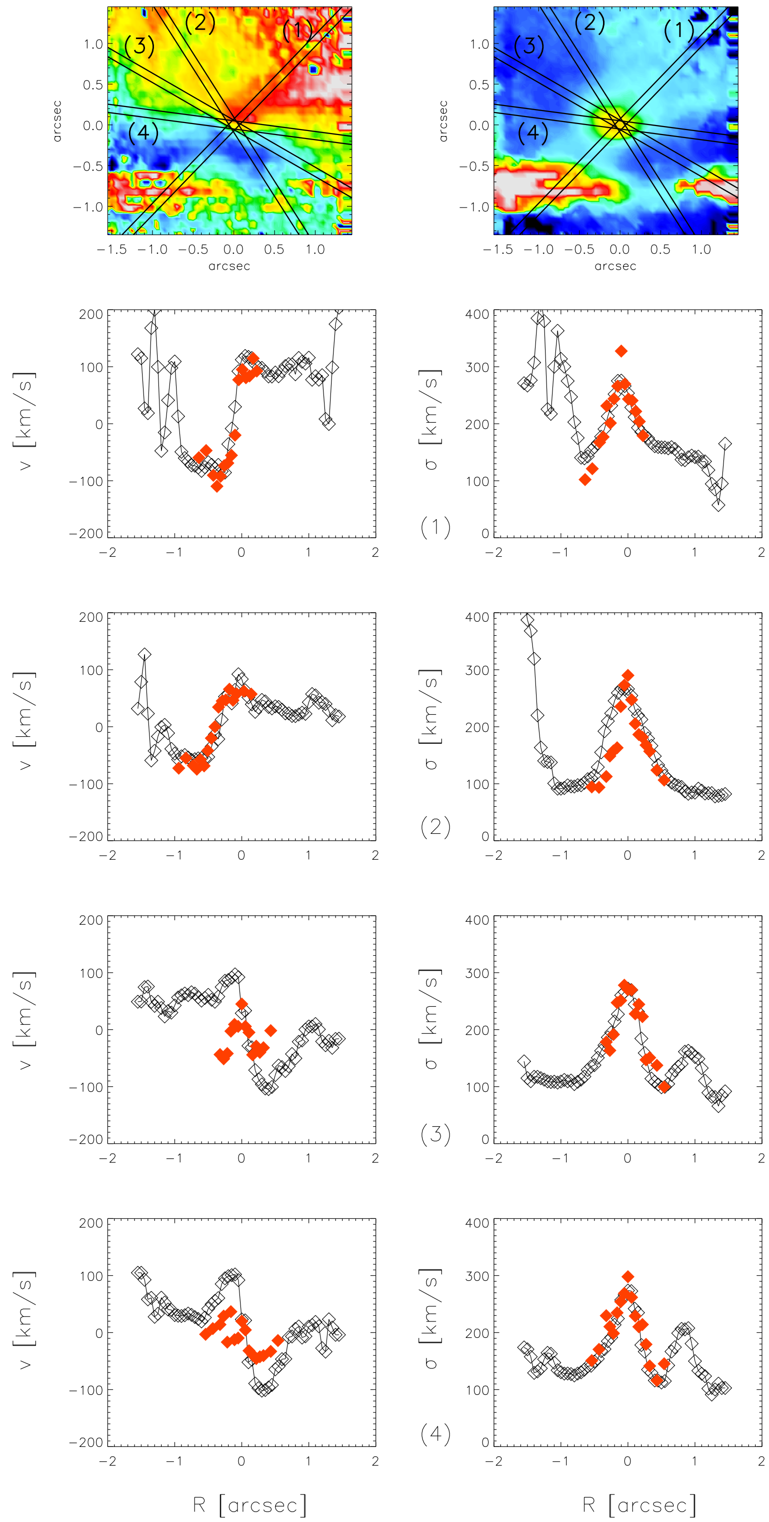

Figure 5.8 Comparison of the velocity and velocity dispersion between the NaCo (filled red diamonds) and SINFONI (open diamonds) [Fe II] data. The curves are extracted along the slit positions indicated in the 2D velocity fields. The position angles are denoted (1) -44°.0, (2) 32°.5, (3) 70°.0, (4) 82°.5 (measured counter-clockwise from North-South).

5.4 Gas dynamical modelling

5.4.1 Method

The dynamical model follows the approach of HN+06 and uses two-dimensional SINFONI gas kinematic maps as constraints. In brief: to explain the H_2 gas motions seen in the centre of Cen A we construct a kinematic model where we assume the gas moves in a thin disk solely under the gravitational influence of the surrounding stars and the expected central black hole. Then, the gravitational potential is given as $\Phi(r) = \Phi_\star(r) + \Phi_{\mathrm{BH}}(r)$. The stellar potential $\Phi_\star$ is taken from HN+06, where Naos-Conica, NICMOS, and 2MASS K-band images of NGC 5128 are used to construct a Multi-Gaussian Expansion (MGE) parameterisation to the surface brightness of this galaxy (Emsellem et al., 1994; Cappellari, 2002). The assumptions of spherical symmetry and constant stellar mass-to-light ratio ($\mathrm{M}/\mathrm{L_K} = (0.72 \pm 0.04)\ \mathrm{M}_\odot/\mathrm{L}_\odot$ (Silge et al., 2005); HN+06) lead to the three-dimensional mass model, that gives the stellar velocity contribution to the dynamical model.

Our dynamical model is based on the widely used approach to model the emission line profile of gas moving in a thin disk (Macchetto et al., 1997; van der Marel and van den Bosch, 1998; Bertola et al., 1998; Barth et al., 2001). In HN+06 we considered three conceptual modelling approaches: 1) a cold disk model that fully neglects the velocity dispersion, 2) a hot disk model that accounts for the high velocity dispersion of the gas, and 3) a spherical Jeans model that accounts for the high velocity dispersion but neglects the indicated disk geometry. We do not repeat the spherical Jeans model here, as the H_2 velocity maps clearly require a disk model. Since the observed velocity dispersion even of the H_2 gas at the nucleus of Cen A exceeds the mean rotation by more than a factor of two, we must account for the velocity dispersion in the dynamical model. We assume the gas disk to be geometrically flat but with an isotropic pressure and construct an axisymmetric Jeans model in hydrostatic equilibrium. In this case, the mean rotation velocity (azimuthal velocity) $\overline{v_\Phi}$ is given by the Jeans equation (Binney and Tremaine, 1987, Eq.4-64a)

$$\overline{v_\Phi}^2 = \frac{R}{\rho_g}\frac{\partial(\rho_g \sigma_R^2)}{\partial R} + R\frac{\partial \Phi}{\partial R}, \tag{5.2}$$

where R is the projected radius and σ_R is the radial velocity dispersion of the gas. We assume that the H_2 surface brightness of the gas disk Σ_g reflects the tracer gas density ρ_g (see section 5.4.3 for a discussion). Note that the model is not self-consistent, i.e. the contribution of the gas mass to the overall potential is neglected. Following Israel et al. (1990), the total mass of H_2 inside the central $\sim 10" \times 10"$ is $2 \times 10^7 \mathrm{M}_\odot$. Inside the field of view of our SINFONI observations we therefore expect $\mathrm{M}_{\mathrm{H}_2} \sim 2 \times 10^6 \mathrm{M}_\odot$, which is a factor of 30 to 100 smaller than the black hole mass measurements for Cen A (HN+06; Marconi et al. 2001), and therefore negligible.

To match the observations, the resulting velocity field can then be projected onto the plane of the sky given the inclination angle i, and the position angle (P.A.) of the projected major axis of the gas disk. For comparison with the data, the projected velocity field must also be broadened with the velocity dispersion and then weighted by the gas surface brightness, using the parameterisations given subsequently in Sections 5.4.2 and 5.4.3, respectively.

Finally, we simulate observations of the disk through the SINFONI instrument, i.e. we convolve with the SINFONI PSF and sample over the pixel size, to achieve the best possible match to the data. The model thus has three free parameters, the black hole mass $\mathrm{M_{BH}}$, the inclination angle of the disk i, and its projected P.A. ζ. The galaxy centre position on the detector and the stellar mass-to-light ratio are fixed beforehand, with $\mathrm{M/L_K} = (0.72 \pm 0.04)\ \mathrm{M_\odot/L_\odot}$ as described above. To measure the black hole mass in NGC 5128, we run models with different values for the free parameter and look for the best possible match to the data, minimising the χ^2.

For the modelling we use the IDL software[3] of HN+06, which accounts for the SINFONI PSF (as determined in Section 5.2.1), instrumental broadening, and the finite SINFONI pixel size, to generate a two-dimensional model spectrum with the same pixel scale as the observations. The extraction of the mean velocity and velocity dispersion from this synthetic data cube is carried out in exactly the same manner as for the observed data, by fitting single Gaussians to the individual spectra at each pixel.

5.4.2 Intrinsic gas velocity dispersion

The observed velocity dispersion of the [Fe II] and of molecular hydrogen $\mathrm{H_2}$ gas at the centre of NGC 5128 peaks at $\sim$ 300 km/s and exceeds the mean rotational velocity by more than a factor of two. The physical origin of this high velocity dispersion is not clear. Partially it might be explained by unresolved rotation (Marconi et al., 2001, 2006), or it might be due to local turbulent gas motions, as suggested by several authors for other galaxies (e.g. Barth et al., 2001; van der Marel and van den Bosch, 1998; Verdoes Kleijn et al., 2002).

Regardless of its physical cause, we consider the high velocity dispersion to contribute to the pressure support of the gas disk. Following the approach of HN+06 we include the velocity dispersion to the gas dynamical model via an isotropic pressure term in the Jeans equation. The rotational velocity therefore becomes sub-Keplerian. We find that the intrinsic velocity dispersion is well described by a double exponential profile of the form

$$\sigma_R = \sigma_0 e^{-r/r_0} + \sigma_1 e^{-r/r_1}, \tag{5.3}$$

and we fit the observed velocity dispersion profile for the best set of parameters (σ_0=140 km/s, $\sigma_1 = 65$ km/s, $r_0 = 0\overset{''}{.}25$, and $r_1 = 4\overset{''}{.}0$) to get the intrinsic dispersion profile.

---

[3] using Craig B. Markwardt's MPFIT package

5.4.3 Emission line surface brightness

For various aspects of the modelling, we need to know the intrinsic spatial emission line profile (assumed to be axisymmetric). But a direct deconvolution of the observed surface brightness is very difficult, since for adaptive optics observations the exact shape of the PSF is unknown and we would therefore introduce artifacts to the gas distribution that bias the velocity distribution inside the inner $0\farcs5$.
Furthermore, the gas morphology of H_2 is quite complex and it is not a priori clear how this complex morphology leads to such a smooth velocity field. On the other hand, the surface brightness does not necessarily resemble the real physical gas structure. The bulk mass in H_2 is most probably at very low temperatures ($T \sim 10-15$ K judging from CO observations Israel et al. 1990) and therefore not excited.
Figure 5.9 shows slices trough the data cube around the H_2 line. The width of the bins is 33 km/s. One sees material that is located near the nucleus and is present in several consecutive panels, meaning, that the material has a high velocity dispersion. In addition there is material that appears in shell-like structures only in one or two bins, hinting towards a lower velocity dispersion. The surface brightness of the H_2 gas seems to be highest along the jet direction for $0\farcs5 < r < 1\farcs3$ (see Figure 5.6). We actually see shell-like structures that might be due to shocked H_2 gas; this hypothesis is supported by the fact that the [Si VI] and Brγ gas distributions fit quite nicely into the shells seen in H_2.

Looking at the flux distribution of H_2 (Figure 5.6), in the radial range $r < 0\farcs4$ a elongated structure which might be reminiscent of a disk is visible with a major axis of P.A.=136°. Ellipse fits to this disk structure give a minor-to-major axis ratio of $q \sim 0.67$ which translates to an inclination angle of $\sim 48°$ given a circular thin disk configuration. The hypothesis of the central disk structure is also supported by the shape of the velocity dispersion field. Looking at the right panel of Figure 5.6 we see a disk-like structure with a major-axis position angle of $\sim 140°$ inside ~ 0.4".

Drawing on the qualitative description of the H_2 line distribution, and the conjecture that the gas moves in a disk, we model the emission line surface brightness in two parts: an exponential disk that dominates the inner 0.5" and a smoothed version of the observed H_2 flux distribution that resembles the detailed gas morphology in the region outside $0\farcs5$, where the PSF convolution is less critical. For the black hole mass modelling it is not important to add the second (larger) component, since the inner $< 0\farcs5$ are dominant. Nevertheless we add it to get a better feeling of the influence of the non-symmetric gas distribution on the appearance of the gas velocity field, since part of the small-scale structure in the velocity fields can be reproduced by a patchy gas surface brightness folded into the model (Barth et al., 2001).

We have tested the influence of the parametrisation of the exponential disk component on the resulting best-fit black hole mass, and find that a profile that

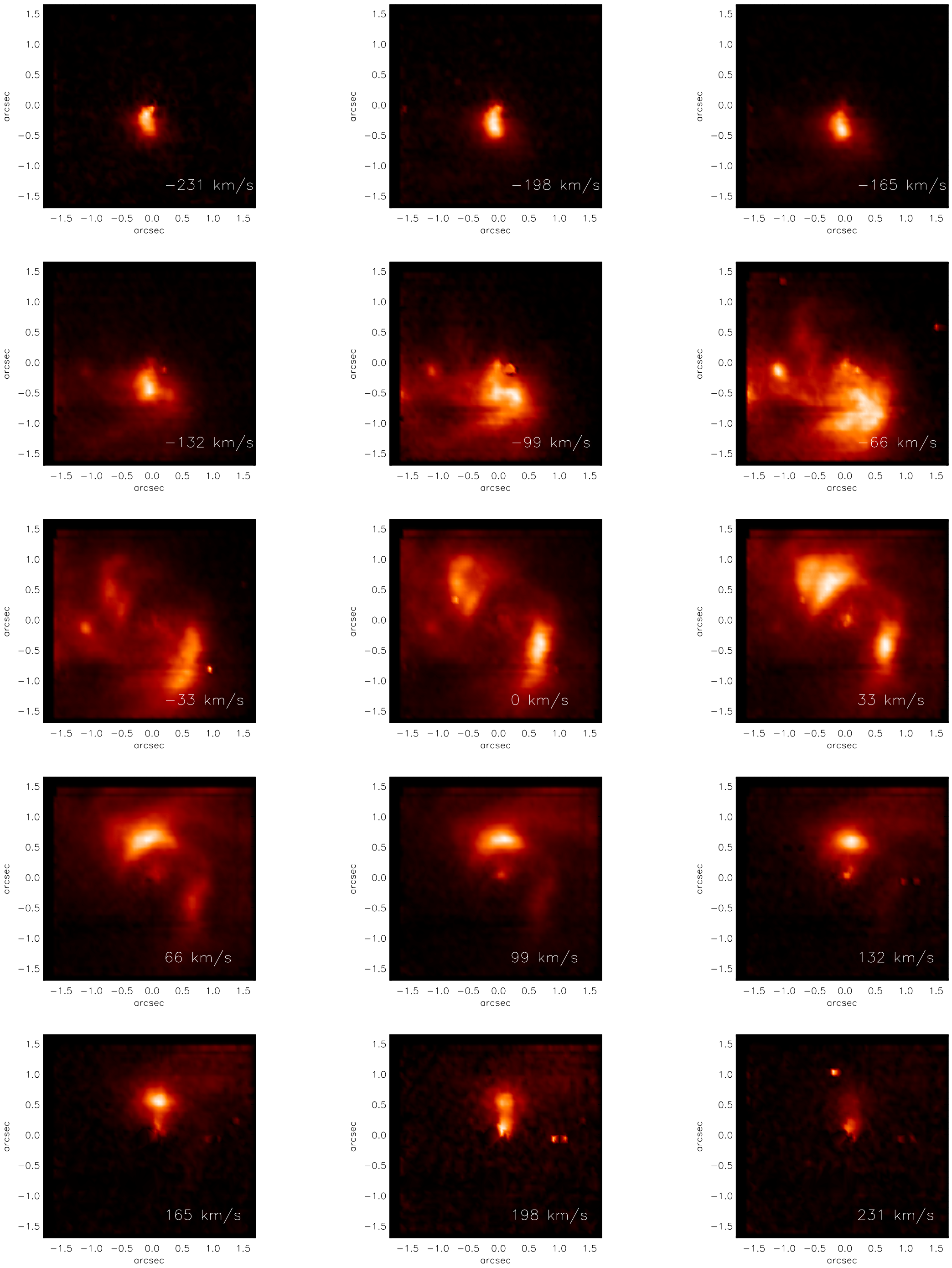

Figure 5.9 Slices through the K-band data in H_2 ($\lambda 2.121\mu$m). The middle panel shows the flux in the velocity bin that corresponds to the recession velocity of the overall galaxy (532km/s). The other bins slice the cube left and right to this zero position. The width of the bins is 33km/s

puts ∼12% more (less) flux inside the central $0\farcs5$ (but still fits the observed flux distribution well) results in a black hole mass that is less than 3% lower (higher). This result is in line with the extensive tests on the influence of the surface brightness parametrisation carried out by Marconi et al. (2006).

5.4.4 Tilted-ring model

The kinematics produced by a flat, or co-planar, thin-disk model are an oversimplification when compared to the observed data. The twists in the velocity field cannot be reproduced, and the velocity gradient is strictly declining from the peak at $\sim 0\farcs2$ outwards without being able to resemble the second and third peak at $0\farcs45$ and $1\farcs1$ (∼ 19pc). We therefore model the kinematics via a tilted-ring model (Begeman, 1987) as it was done before on scales of $r \sim 3'$ by Quillen et al. (1992) and Nicholson et al. (1992) who modelled the CO(2-1) and Hα velocity fields in Cen A, respectively.

The difference to the flat thin-disk model is that the inclination angle and position angle of the gas disk are a function of radius. The orbits of the gas at each radius remain circular, but neighboring orbits are not necessarily in the same plane. The gas-disk geometry changes from co-planar to warped.

We work in polar coordinates and use discrete radial steps where the model is to be calculated. The model is linearly interpolated between the discrete points on the model grid. The gas disk is made up of concentric rings. Each ring is represented by three parameters: its radius, R, inclination angle i, and azimuthal angle ζ (relative to the projected major axis). When projected along the line-of-sight, the rings become ellipses. The flattening, q, of the major and minor axes is related to the inclination angle i via $\cos(i) = q$. The flattening defines an ellipse on the sky of ellipticity $\epsilon = 1 - q$. If the gas is assumed to move on circular orbits along the rings, the projected velocity can be described by the simple cosine form

$$v(R,\zeta) = v_{sys}(R) + v_c \sin(i)\cos(\zeta). \tag{5.4}$$

where v_c denotes the circular velocity on a given ring of radius R, while v_{sys} gives the systemic velocity of the entire galaxy. This method of expanding the full gas velocity field in a set of tilted rings goes back to the work of (Schoenmakers et al., 1997). Here, we are using the method of Krajnović et al. (2006a), called kinemetry, to determine the set of best-suited ellipses along which the velocity field is best described by equation (5.4). The parameters of the 27 tilted rings are plotted in Figure 5.10 and listed in Table 5.1, while Figure 5.11 shows the fitted circular velocity map, using these parameters. Note that the parameters of the tilted-ring model vary smoothly with radius, although we do not restrict the kinemetry routine to smooth functions $i(R)$ and $\zeta(R)$.

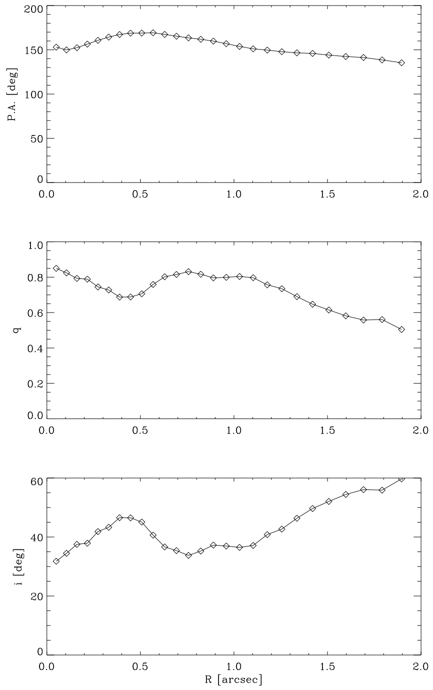

Figure 5.10 Disk parameters of the kinemetry fit as a function of projected radius. The inclination angle i is derived from the flattening q ($i = \arccos(q)$)

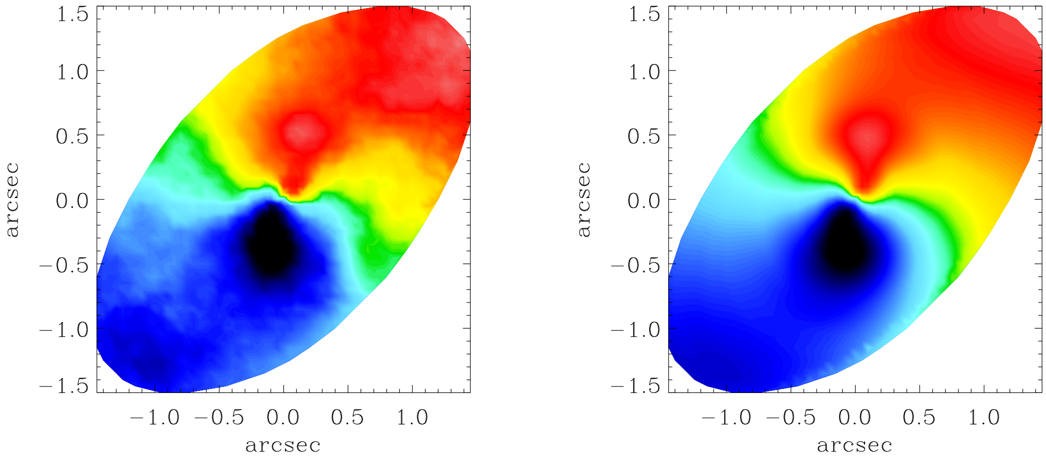

Figure 5.11 Kinemetry model (right panel) in comparison to the H_2 velocity field (left panel). The ellipse shows the flattening of the largest circle.

Table 5.1 Parameters of the tilted ring model

R [″]	P.A. [°]	q	i [°]	v [km s^{-1}]
0.05	153.0	0.85	31.8	55.
0.10	149.9	0.82	34.5	106.
0.16	152.4	0.79	37.5	112.
0.22	156.4	0.79	37.9	107.
0.27	160.7	0.74	41.8	110.
0.33	164.4	0.73	43.3	110.
0.39	167.3	0.69	46.6	113.
0.45	168.8	0.69	46.5	115.
0.51	168.9	0.71	45.1	109.
0.57	169.2	0.76	40.6	103.
0.63	167.4	0.80	36.6	96.
0.69	165.4	0.82	35.4	89.
0.76	163.5	0.83	33.8	82.
0.82	161.9	0.82	35.2	79.
0.89	159.8	0.80	37.2	76.
0.96	156.9	0.80	36.9	76.
1.03	153.8	0.80	36.5	75.
1.10	151.1	0.80	37.1	75.
1.18	149.7	0.76	40.8	76.
1.26	147.9	0.74	42.7	77.
1.34	146.6	0.69	46.4	80.
1.42	145.9	0.65	49.7	83.
1.51	144.1	0.61	52.1	85.
1.60	142.4	0.58	54.4	87.
1.69	141.3	0.56	56.1	88.
1.79	138.6	0.56	55.9	90.
1.90	135.4	0.50	59.7	89.

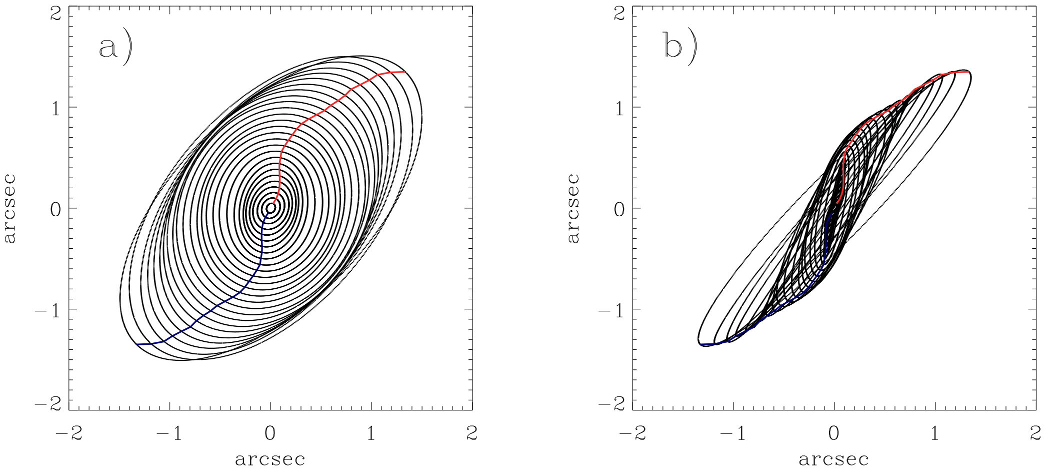

Figure 5.12 The tilted-ring model to the nuclear gas disks seen at (a) the original orientation as fitted by kinemetry and (b) rotated by 45° to make the warp more visible. The red and blue lines are the overlaid line-of-nodes for the receding and approaching side, respectively.

5.5 Results

We are modelling the H_2 gas kinematics in the central 1″ (∼ 17pc) of NGC 5128 with a warped disk model in the potential of the stars and the central black hole. The central black hole mass as well as the overall inclination angle of the gas disk are varied to find the best-fit to the observed velocity and velocity dispersion maps.

5.5.1 Structure of the H_2 disk

The rotational velocity field seen in molecular hydrogen shows beautiful symmetry about the centre despite the twist that alters the projected orientation of the kinematic major axis by ±14° about a mean value of ∼ 155° (see Table 5.1). Especially for the central values, the orientation of the H_2 gas disk is consistent with an orthogonal disk-jet picture, as the radio jet in Cen A is located at a position angle of 51° (Tingay et al., 1998).

In addition to the twist in position angle there is a superimposed variation of inclination angle that causes the maximum of the projected rotational velocity to vary by ± 30 km/s (around a mean value of 90 km/s (cf. Table 5.1)).

The structure of the gas disk as fitted by the tilted-ring model is presented in Figure 5.12. The left panel (a) shows the original fit from kinemetry. In panel (b) the disk is rotated by 45° to an almost edge-on view, to make the warp clearly visible. The position angle twist is indicated by the red and blue lines for the receding and approaching side, respectively.

Our SINFONI integral field data allow us to constrain the inclination angle of the gas disk very well. Its mean value is 42°, which is in very good agreement with the best-fitting inclination angle measured by HN+06 from their NaCo long-slit data (45°). The inclination angle is also in agreement with the value derived by Hardcastle et al. (2003) from VLA data ($20° < i < 50°$), it is however somewhat smaller than the value from VLBI data derived by Tingay et al. (1998) ($50° < i < 80°$).

The central H_2 gas kinematics are well resembled via the tilted-ring model while a co-planar disk model would not be able to reproduce the twist in the rotational velocity field and would therefore represent an oversimplification of the kinematic structure.

The warp of the larger scale disk (> 10") was probably caused by the merger event, that occurred a few times 10^8 years ago (Quillen et al., 1993; Peng et al., 2002). It is not a priori clear whether the warp in the innermost arcsecond is connected to this larger scale warp that creates the prominent appearance of the dust disk in Cen A (Quillen et al., 2006). For the nuclear gas disk on scales $\lesssim 1\overset{''}{.}2$ ($\lesssim$ 20pc) self-induced warping of the accretion disk (Pringle, 1996) might be the driving mechanism. Our model is not intended to explain the origin of the warp, but is rather meant as a geometric model to resemble the observed velocity field.

5.5.2 Importance of the inclination angle

The best-fit black hole mass in gas dynamical models depends very strongly on the assumed inclination angle of the modelled gas disk ($M_{BH} \propto \sin(i)$). Any uncertainty in the disk inclination angle will directly propagate to the uncertainty in the black hole mass.

Our tilted-ring model fitted by kinemetry fixes the overall shape of the gas disk in the model. However, we allow for overall variations in the inclination angle, not to overconstrain the model. That means the position angles for the tilted-rings remain fixed, as well as their relative orientation. What is varied, is their global inclination.

In that way we make use of the geometrical information that is contained in the velocity field (using kinemetry), but at the same time give our dynamical model the freedom to find the best inclination angle given the general assumptions of the model.

5.5.3 Best-fit model and black hole mass

The best-fitting black hole mass in our tilted-ring model to the H_2 kinematics is $M_{BH} = (7.0 \pm 1.0) \times 10^7 M_\odot$ for a median inclination of $\sim 27°$. This is the minimum in the $\Delta\chi^2$ distribution, shown in Figure 5.14. The associated best-fit model velocity and velocity dispersion maps are shown in comparison to the data in Figure 5.15. Figure 5.13 shows a comparison of the model and the data for the case of no central point mass. Here, the gravitational potential is made up only by the stars. The mass-to-light ratio is 0.72 $M/L_{\odot,K}$ (HN+06). It is obvious that this is no good fit in the central $0\overset{''}{.}5 \times 0\overset{''}{.}5$. The modelled rotation only catches up with the data outside $\sim 0\overset{''}{.}75$, where the stars clearly dominate the gravitational potential. The case for no black hole is ruled out to over 5σ.

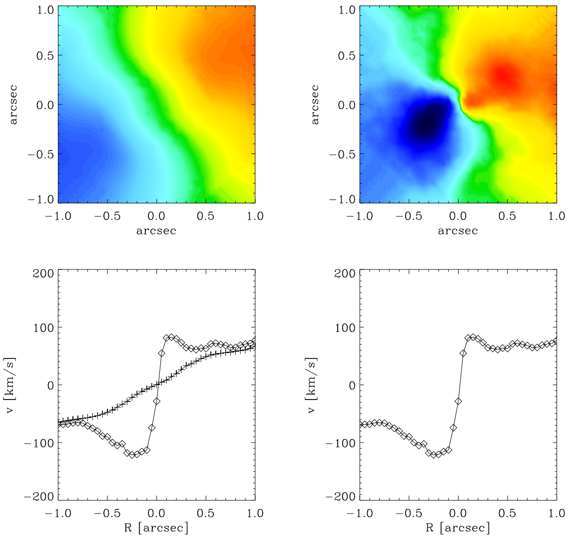

Figure 5.13 Comparison of data (right) and model (left) for the case of zero black hole mass and the stellar potential derived by HN+06. The bottom panels show the velocity curves extracted along the virtual slit indicated in the top panels. The model velocity curve (crosses) is in reasonable agreement with the data (diamonds) outside 0.″7.

There are various factors that influence the black hole mass in our dynamical model and we have done a substantial number of test to scrutinise their impact on the best-fit result.

As mentioned in Section 5.5.1 the assumed geometry of the disk (warped vs. flat) has a small influence on the black hole mass. The same holds true for the parametrisation of the surface brightness. We modelled the kinematics for three different parametrisations of the disks surface brightness profiles, with all three being a reasonable fit to the data. We found that the black hole mass does change by less than 3% depending on the assumed surface brightness profile of the inner gasdisk. This result is in agreement with the detailed analysis of Marconi et al. (2006).

Obviously, also the contribution of the stellar potential to the total gravitational potential influences the resulting best-fit black hole mass. We used the two extreme values 0.72 $M/L_{\odot,K}$ and 0.53 $M/L_{\odot,K}$ derived by Silge et al. (2005) through stellar dynamical models at different inclination angles. For the latter value, the best-fitting black hole mass increases by $\sim 8\%$ compared to the best-fit value of $M_{BH} = 7.0 \times 10^7 M_\odot$ (for 0.72 $M/L_{\odot,K}$). But the uncertainty introduced by the inclination angle is much larger than this.

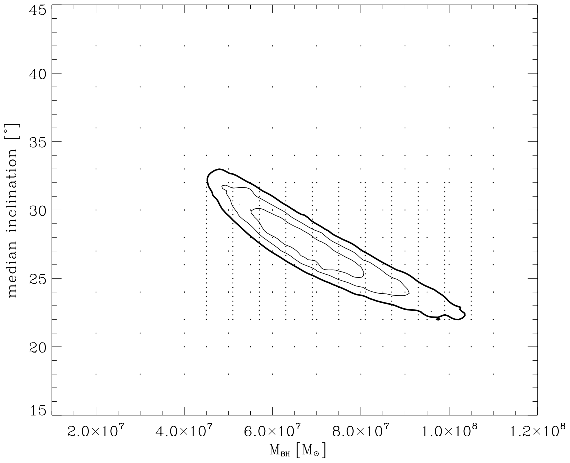

Figure 5.14 Delta χ^2 contours for dynamical models of the H_2 gas as a function of inclination angle and black hole mass. The best fit model, judging from the minimum χ^2 is at a black hole mass of $7.0 \times 10^7 M_\odot$ and a median disk inclination of 27°. The contours indicate the 1σ, 2σ, and 3σ confidence levels, respectively.

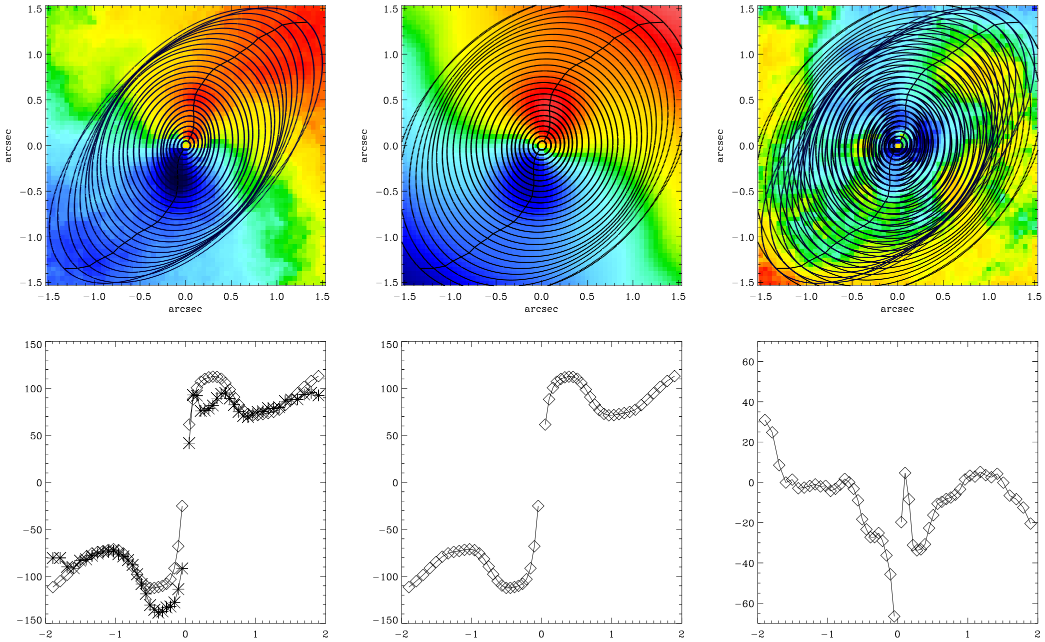

Figure 5.15 Best-fitting dynamical model (top, middle) with a black hole mass of $7.0 \times 10^7 M_\odot$ and a median disk inclination of 27° in comparison to the data (top left). The residual (data-model) is shown in the right panel. The velocity curves in the bottom panels are extracted along the line-of-nodes (overplotted to the velocity maps), and represent the peak velocity curves.

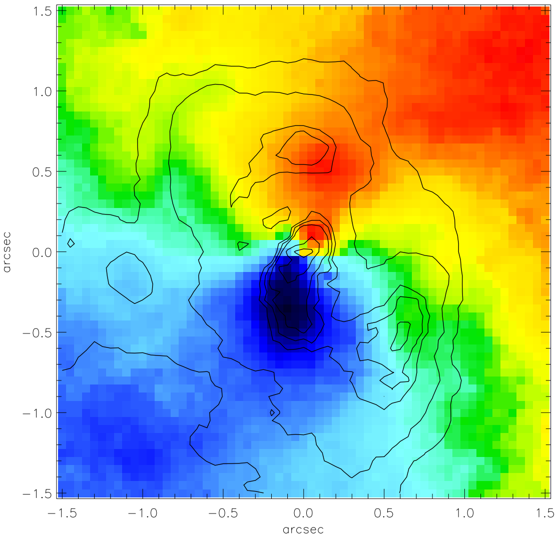

Figure 5.16 The H_2 flux contours are overplotted to the H_2 velocity map. The velocity field is asymmetric in the sense that the blue dip has a higher absolute value than the red peak. This asymmetry is also seen in the flux contours.

5.5.4 Asymmetries in the H_2 velocity field

The overall shape of the H_2 velocity field appears to be point-symmetric about the position of the AGN (the peak in the H_2 surface brightness). This symmetry is proven and resembled by the smooth kinemetry fit.

However, taking a closer look at the peak velocities in the field, it is striking, that the peak velocity in the blue dip at $(x, y) = (-0\farcs2, -0\farcs5)$ exceeds the one in the corresponding red peak ($(x, y) = (0\farcs2, 0\farcs5)$) by ~ 30 km/s (corresponding to $\sim 30\%$ of the peak velocity).

The reason for this asymmetry is not merely an overall velocity shift, since that would affect the whole field. This can be ruled out by the fact that the absolute values of the velocities are in excellent agreement for radii larger than $\sim 0\farcs8$.

It is instructive to overplot the iso-flux contours to the velocity field (see Figure 5.16), since one clearly sees that the asymmetry in the velocity field is also present in the flux distribution. This leads us to speculate that the gas density is not the same throughout the disk. A higher density leads to both an increase flux and to a higher net rotation. The density might be increased by gas that is streaming towards the central disk. This might be of similar origin as the non-rotational motions observed in [Fe II], Brγ, and [Si VI] but is not as obvious in molecular hydrogen. The asymmetry is also present in the Brγ and [Si VI] velocity maps, being strongest in [Si VI]. What we observe here, might be the fuelling process of the nuclear disk.

Our gas dynamical model is by construction symmetric, and therefore not able to reproduce asymmetries in the velocity structure. For determining the best-fit black hole mass, we have minimised the difference of the symmetric model to the

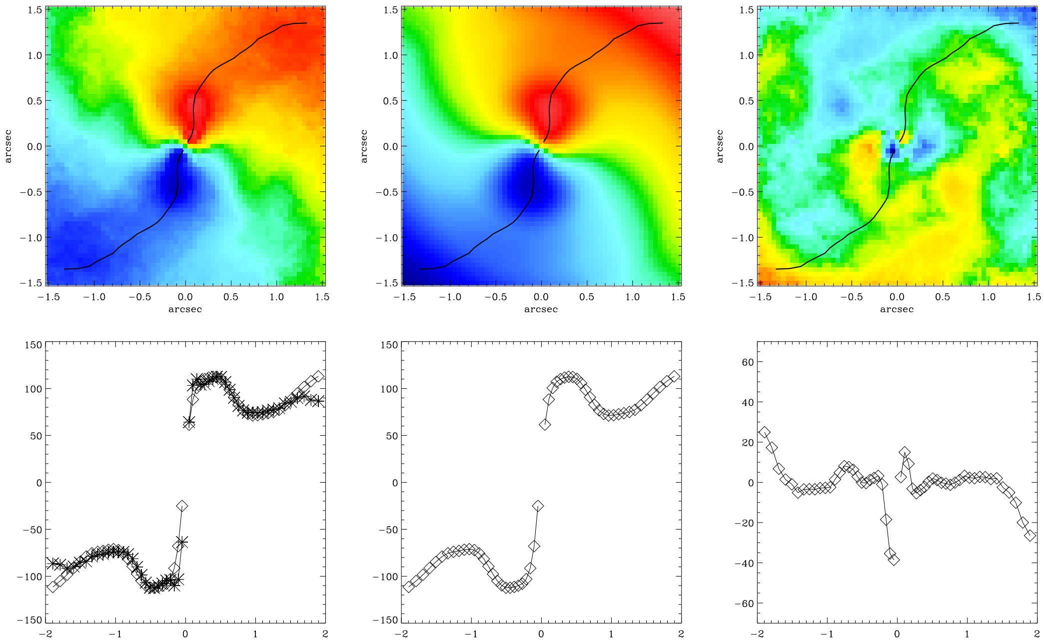

Figure 5.17 The symmetrised velocity map (top left) in comparison to the model (top middle panel). The residual (data-model) is shown in the right panel. The velocity curves in the bottom panels are extracted along the line-of-nodes (overplotted to the velocity maps), and therefore represent the peak velocity curves. The agreement is very good along the line-of-nodes.

asymmetric data, looking for the best compromise. After having gained the best-fit model (to the original data) we are free to compare this to a symmetrised version of the H_2 velocity field, $v_{\rm sym}(x,y) = (v(x,y) - v(-x,-y))/2$.. The agreement, as shown in Figure 5.17, is astonishing.

5.6 Discussion

With our high resolution 2D data, it is almost possible to determine the black hole mass in Centaurus A without any dynamical model, by just using the concept of the radius of influence of the black hole. This is the region where the mass of the enclosed stars equals the mass of the supermassive black hole. It is expressed by

$$\mathrm{r_{BH}} = \frac{\mathrm{GM_{BH}}}{\sigma_*^2}, \tag{5.5}$$

where $\mathrm{M_{BH}}$ is the mass and $\mathrm{r_{BH}}$ is the radius of influence of the black hole, G is the gravitational constant and σ_* is the velocity dispersion of the stellar spheroid. Judging from the velocity field, this is the point of minimum rotation, where the black hole stops to dominate the gravitational potential, before the stars take over. For our H_2 velocity this is at ∼ 1” as seen in Figure 5.15 (left panel). For Cen A we have the following numbers: $\sigma_* = 138$ km/s (Silge et al., 2005), at D= 3.5 Mpc $\mathrm{r_{BH}} \sim 1$" ∼17 pc, and therefore we get $\mathrm{M_{BH}} \sim 7.5 \times 10^7 \mathrm{M}_\odot$.

The best-fit black hole mass derived through modelling of the $\mathrm{H_2}$ kinematics, $\mathrm{M_{BH}} = (7.0 \pm 3.0) \times 10^7 \mathrm{M}_\odot$ at $i = 27°$, is in excellent agreement to the mass derived by HN+06 ($(6.1^{+0.6}_{-0.8}) \times 10^7 \mathrm{M}_\odot$ at $i = 45°$) using high spatial resolution kinematics of [Fe II] derived from AO-assisted Naos-Conica long slit data (FWHM= $0\farcs11$). The dynamical model they used is in principle identical to the one described above, except the fact that we cover the velocity field in two dimensions and they modelled only four slit positions.

Concerning the disk geometry, HN+06 excluded disk inclination angles below 45° due to the jet inclination derived by Tingay et al. (1998), who give $50° < i < 80°$. However, following the analysis of Hardcastle et al. (2003), who use jet-counterjet ratios and apparent motions in the jet, the jet inclination is most likely in the range $20° < i < 50°$. HN+06 state that if they were to allow and inclination angle of $i = 25°$ with respect to the line-of-sight, their best-fit black hole mass is $1.2 \times 10^8 \mathrm{M}_\odot$. This is somewhat larger than the value we measure. But one has to take into account, that the modelled gas species are not the same for the two studies. While the molecular gas has a well-ordered rotation field, the 2D velocity field of [Fe II] (Fig. 5.5) clearly exhibits two components: inflow and rotation. This superposition could not be seen in the long-slit data and was not accounted for in the model of HN+06. They modelled the total [Fe II] kinematics under the assumption of gas rotating in a flat, thin disk.

The agreement of our modelling results with the recent analysis of (Krajnović et al., 2006b) is comforting: they modelled integral-field Paβ kinematics and derived $\mathrm{M_{BH}} = 8.25^{+2.25}_{-4.25} \times 10^7 \mathrm{M}_\odot$ at $i = 25°$. The resolution of their seeing limited data is $0\farcs5 - 0\farcs6$, i.e. a factor of $\sim 4 - 5$ larger than ours, but good enough to resolve the radius of influence of the black hole in Cen A.

This decrease in black hole mass compared to recent measurements by Marconi et al. (2001), $\mathrm{M_{BH}} = 2.0^{+3.0}_{-1.4} \times 10^8 \mathrm{M}_\odot$, Silge et al. (2005), $1.8^{+0.4}_{-0.4} \times 10^8 \mathrm{M}_\odot$ for i=45°, and the agreement with the mass determinations of Marconi et al. (2006), HN+06, and Krajnović et al. (2006b) bring Centaurus A very close to the $\mathrm{M_{BH}}$-σ relation, and do not make it appear a dramatic outlier (Ferrarese and Merritt, 2000; Gebhardt et al., 2000).

5.7 Conclusions

This work presents observations of the nearby active elliptical galaxy NGC 5128 (Cen A) with the adaptive-optics assisted integral field spectrograph SINFONI at the VLT. Our K-band data used to measure the black hole mass in Cen A have a spatial resolution of $0\farcs12$ and an estimated Strehl ratio of $\sim 17\%$. The field of view is $3'' \times 3''$.
In our H- and K-band data we detect the following emission lines: [Fe II], [Si VI], [He I], Brγ, [Ca VIII], and several vibrational transitions of molecular hydrogen, H_2 (the strongest is 1-0 S(1) at 2.12μm).

- Analysing the velocity fields of [Si VI], Brγ, [Fe II], and the strongest H_2 line, we find that the surface brightness and also the gas motion of the gas species is increasingly influenced (or produced) by the jet when going from low to high excitation lines. The velocity fields of [Si VI], Brγ, and [Fe II] clearly exhibit two components: 1) rotational motion at a major angle of $\sim 150°$, consistent with an orthogonal disk-jet picture, and 2) non-rotational motion along the direction of the jet, that is consistent with a back-flow of gas along the side of the jet's cocoon. This non-rotational component is strongest for [Si VI].

- The surface brightness of H_2 shows a central gas disk at a position angle of P.A.$\sim 136°$ and a minor-to-major axis ratio of 0.67. The bright spots NE and SW of the nuclear disk remind of the lobes seen on much larger scales in jet-gas interactions.

- The overall velocity field of H_2 shows beautiful point-symmetry about the unresolved nucleus. However, the H_2 peak velocities are asymmetric inside the central $0\farcs7$. This asymmetry is also seen in the surface brightness map of H_2, and might be explained by denser gas, that leads to both an increase in flux and to a higher net rotation. The density could be increased by gas that is streaming towards the central disk. This might be similar to the non-rotational motions observed in [Fe II], Brγ, and [Si VI] but is not as obvious in molecular hydrogen. It is possible that we evidence the fuelling process of the nuclear disk.
  Another influence of the jet on the velocity field might be the twists in the zero velocity curve (at the positions where the lobes appear in the surface brightness map of H_2). The rotational major axis (line-of-nodes) runs from SE to NW, with the SE side blue- and the NW side redshifted with respect to the nucleus. It follows the shape of an 'S'. The velocity field is reminiscent of a warped disk. We believe that the major part of the H_2 gas is well settled in the total gravitational potential $\Phi_\star + \Phi_{\rm BH}$, as judging from its smooth velocity fields, and is therefore a good tracer of the central black hole mass.

- Under the assumption of gas moving on circular orbits, we fit the geometry of the gas disk with a set of tilted rings, using kinemetry (Krajnović et al., 2006a). The mean P.A. is 155° with twists of ±14°. The median inclination angle is $\sim 42^\circ \pm 12^\circ$.

- We construct a tilted-ring model for the central H_2 gas motions, in the combined potential of the stars and the black hole. We account for the velocity dispersion via a pressure term in the isotropic, axisymmetric Jeans' equation. The geometry of the disk is fixed via the kinemetry fit to the velocity field, but we allow the overall inclination angle to vary. Our best-fit model has a mean inclination angle of $27^\circ \pm 5^\circ$, and a black hole mass of $M_{BH} = (7.0 \pm 1.5) \times 10^7 M_\odot$. We find that the inclination angle, derived through the kinemetry fit is not able to reproduce the overall velocity field. We conclude that the optimal choice would be to simultaneously fit the disk geometry and the black hole mass.
  As our dynamical model is per construction symmetric about the centre, it fails to reproduce the asymmetry in the H_2 data. When symmetrising the velocity field, the agreement of data and model is excellent.
- Our black hole mass measurement is consistent with previous gas measurements, and somewhat smaller than the stellar dynamical estimate.
- Our black hole mass determination concludes that Cen A's offset to the $M_{BH} - \sigma$ is less than a factor 2.5 and it is therefore no dramatic outlier to this relation.

6. Circumnuclear star formation in Centaurus A?

6.1 Introduction

It is now widely believed that the creation and growth of massive black holes is physically connected to the formation of bulges and elliptical galaxies. The remarkably tight correlations between the central black hole mass and bulge properties (e.g. velocity dispersion or bulge mass, Ferrarese and Merritt, 2000; Gebhardt et al., 2000; Häring and Rix, 2004) provide powerful evidence for this connection. The host galaxies of AGN frequently show signatures of post-starburst, and young stellar populations (see review by Heckman, 2004). This indicates that the nuclear star formation activity and the AGN both use the same fuel - the circumnuclear molecular gas (Schinnerer et al., 2001). However, the physical connection between star formation and AGN activity is still not well understood. The energy liberated by black hole accretion can either trigger star formation (e.g., by dynamically compressing gas clouds through radio jets) or suppress it (e.g., by blowing away the gas through AGN feedback). To put constraints on the time sequence of black hole and galaxy growth, it is very important to measure the ongoing star formation rate in AGN host galaxies (see e.g. Ho, 2005).

At a distance modulus of 27.5, individual bright young stars, and even giants of intermediate age populations (Harris et al., 1999; Harris and Harris, 2000; Rejkuba et al., 2002) can be detected by Naos-Conica in Centaurus A. The radio-map of Cen A shows a jet down to the smallest scales (1”-2”) at a P.A.= 51° (Tingay et al., 1998). Rejkuba et al. (2002) find young blue stars aligned with the jet over a distance of $\sim 9 - 19$ kpc ($\sim 9' - 19'$) from Cen A’s nucleus.

In this chapter, we want to explore how the AGN, its radiation and outflows affect the very central star formation. How many young stars are in the inner 200 pc and how old are they? Did they form as a consequence of the merger at nearly one instant, or are they part of a prolonged nuclear star formation?

6.2 The J, H, K images

Near infrared observations were performed in 2003 June 14 (J band), 2004 April 1 (K band), and 2005 January 31 (H band), with Naos-Conica (NaCo) (Lenzen et al., 1998; Rousset et al., 1998) at the Yepun unit (UT4) of the ESO Very Large Telescope (VLT). The seeing during the observations was very good for all runs, in the range $0\farcs3 - 0\farcs8$ as measured by the seeing monitor in V-band. The J-, H-, and K-band images are presented in Figure 6.1.

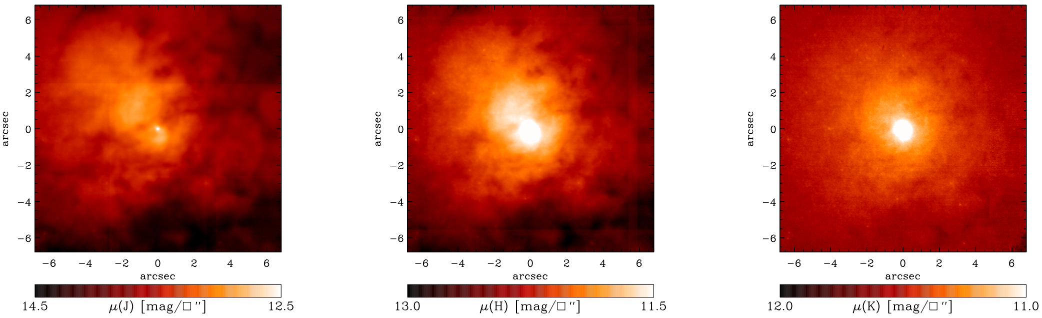

Figure 6.1 J-, H-, and K-band images of the central 13" × 13" region of Cen A (from left to right). The images are calibrated and the surface brightness is given in mag/□″, as displayed by the colourbar. The bright, unresolved source at the centre of the image is the AGN. It is visible in all bands and becomes dominant in K-band. Dust extinction is strongest in J-band.

There are no potential reference stars bright enough ($m_K \lesssim 14$ mag) for the wavefront correction at a distance of $\lesssim 30$" to the nucleus, necessary for a good quality of correction at the nucleus. Therefore, we directly guided on the nucleus itself using the unique IR wavefront sensor (WFS) implemented in Naos. This strategy provides us the best possible wavefront correction in the vicinity of the active galactic nucleus (AGN). During the observations the atmospheric conditions were stable and the performance of the IR WFS was steadily very good. For observations in J- and H-band we used the K-dichroic, i.e. all the nuclear K-band light for wavefront correction. While observing in K-band itself the only possibility to achieve a good performance of the WFS was to send 90% of the light to Naos and only 10% to Conica (i.e. use the N90C10 dichroic).
To remove bad pixels and cosmics we jittered the field on several positions on the detector. The on-chip exposure time was 60 s in J-, 20 s in H-, and 120 s in K-band and the total exposure time 20 min in J-band, 13 min in H-, and 40 min in K-band. For the flux calibration (and at the same time for background subtraction) a separate PSF star was observed directly before and after the nucleus of Cen A with the same WFS setup and exposure time. This star was chosen from the 2MASS point source catalogue (Cutri et al., 2003) to be far away enough to guarantee a clear sky background and to match Cen A's nucleus as closely as possible: in angular

proximity, magnitude and colour. As already discussed in the previous chapter, it is not necessary to take a separate PSF star for the assessment of the image quality. It is actually favourable to measure the PSF on the unresolved nucleus in the science frame.

The data were reduced using standard data reduction tasks in IRAF and using the ESO eclipse software to combine the jittered frames. The frames were flat-fielded, sky and dark subtracted, and bad pixels were removed.

The nucleus is unresolved at all wavelengths with a size (full width half maximum FWHM) of $0.''1$ in J-, $0.''088$ in H-, and $0.''059$ in K-band. This sets the quality for our AO correction. In K-band we reach the diffraction limit of the VLT. For the following analysis it is not crucial to know the exact shape of the PSF, that is why we do not investigate this further (see chapters 4 and 5 for a more detailed analysis of the PSF).

The flux values given in Table 6.1 are extracted in circular apertures of two times the resolution width, that makes $0.''2$, $0.''17$, and $0.''12$ diameter in J, H and K, respectively.

Table 6.1 Magnitudes of the nucleus in J, H, and K

Filter	FWHM	aperture	mag
J	$0.''10$	$0.''20$	15.2
H	$0.''088$	$0.''17$	13.45
K	$0.''059$	$0.''12$	10.6

6.3 Colour maps

The calibrated images are used to construct colour maps of the central $\sim 13" \times 13"$ region, presented in Figure 6.2. The images are scaled in a way that darker areas are redder, or in other words, brighter in the longer wavelength filter. The nucleus is dark in all three panels, indicating that it becomes brightest in K-band (see Fig. 6.1). The reason for this is both due to the fact that longer wavelengths become less extinct, and that the AGN has an intrinsically red colour, with a peak at $\sim 5\,\mu$m as seen from the spectral energy distribution (Meisenheimer et al., 2007).

The structures are enhanced by the overlain contours. The constriction of brighter colours and the elongation of darker colours close to the nucleus is the imprint of Cen A's dust lane that lies in the NW-SE direction. The light that passes through this dust layer is therefore scattered and absorbed. The entirety of scattering and absorption is called extinction. The amount of extinction is wavelength-dependent,

such that shorter wavelength get more extinct. The wavelength dependency is given by the ‘extinction law’. It is an empirical quantity, giving the extinction A(λ) (for a certain wavelength λ) relative to the extinction in V-band A(V) (which is arbitrarily chosen as reference) (see e.g. Mathis, 1990, for a review).
Judging from the J-K colour map, which spans the longest wavelength range, the extinction is highest towards the SW.

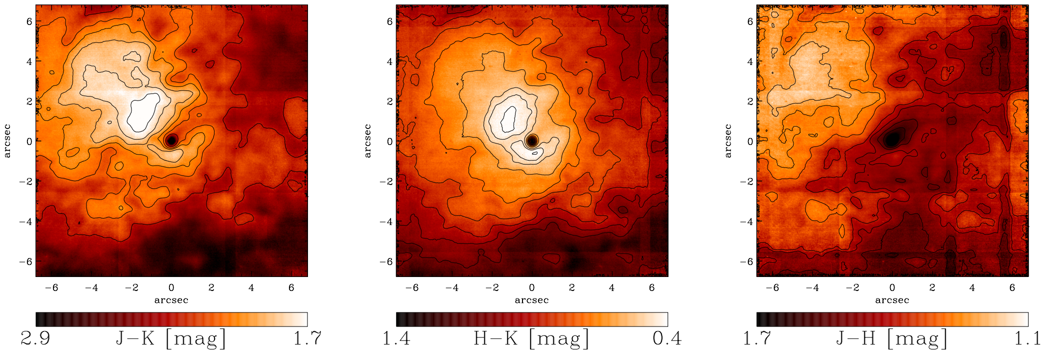

Figure 6.2 J-K, H-K, and J-H colourmaps of the same region as the images in Figure 6.1 (the central 13” × 13” around the AGN). The images are displayed in a way that darker areas are redder, i.e. brighter in longer wavelengths. These areas can be associated with the foreground dust layer, that spans across Cen A’s nucleus. The stripes in the images are due to the jitter pattern in J-band.

6.4 Dust maps - Extinction correction

In order to get the intrinsic colours and light distributions throughout the entire field of view, we perform a dust correction, also called de-reddening, of the images. Hereby, the main assumptions are that i) the dust sits in a foreground screen, ii) Cen A has an intrinsic colour similar to elliptical galaxies, and iii) no significant colour gradients are present throughout the field of view.

We briefly present a simple, zero-order estimate to correct for reddening which is derived from the colour in two bands at λ_1 and λ_2 as:

$$M^{\circ}_{\lambda_1} = M_{\lambda_1} - A(\lambda_1) = M_{\lambda_1} - \frac{R(\lambda_1)}{R(\lambda_1) - R(\lambda_2)} E(\lambda_1 - \lambda_2) \tag{6.1}$$

where $M^{\circ}_{\lambda_1}$ and M_{λ_1} are the intrinsic and reddened magnitudes at the effective wavelength λ_1, $R(\lambda)$ is the extinction curve, i.e. $A(\lambda) = R(\lambda)E(B-V)$, and $E(\lambda_1 - \lambda_2) = A(\lambda_1) - A(\lambda_2)$. $E(\lambda_1 - \lambda_2)$ can be derived from the colour $M_{\lambda_1} - M_{\lambda_2}$ as:

$$E(\lambda_1 - \lambda_2) = (M_{\lambda_1} - M_{\lambda_2}) - (M^{\circ}_{\lambda_1} - M^{\circ}_{\lambda_2}) \tag{6.2}$$

where we assume an intrinsic colour, $M^{\circ}_{\lambda_1} - M^{\circ}_{\lambda_2}$, constant over the entire field of view.

Different point spread functions (PSFs) are taken into account by convolving each image with the PSF of the other. We have adopted the reddening curve by Cardelli et al. (1989), according to which $R(V) = 3.20$, $R(J) = 0.87$, $R(H) = 0.58$, and $R(K) = 0.35$. Using the above formalism, we construct an E(B-V) map for the nuclear region by combining the J- and K-band, and H- and K-band images, respectively. We assume an intrinsic colour $(H-K)_0 = 0.20$ mag and $(J-H)_0 = 0.75$ mag which is an average value for both spiral bulges and elliptical galaxies with a standard deviation of only 0.1 magnitudes (e.g. Impey et al., 1986; Hunt et al., 1997). The reference extinction map is then derived via $A(V) = R(V)E(B-V)$.

To qualitatively verify the accuracy of the correction procedure, we apply the reddening correction to the J-band image. Figure 6.3 shows the J-band image, the J-band extinction map A(J) derived from $(J-H)$, and the reddening corrected J_0 image (from left to right). The corrected image is seen to be mostly smooth, similar to the K-band image which is obviously little affected by reddening. The correction fails only in a region of high extinction below the nucleus (i.e. the fold of the molecular disk, see Quillen et al. (1993)) where A(V) reaches values as high as ~ 15 mag.

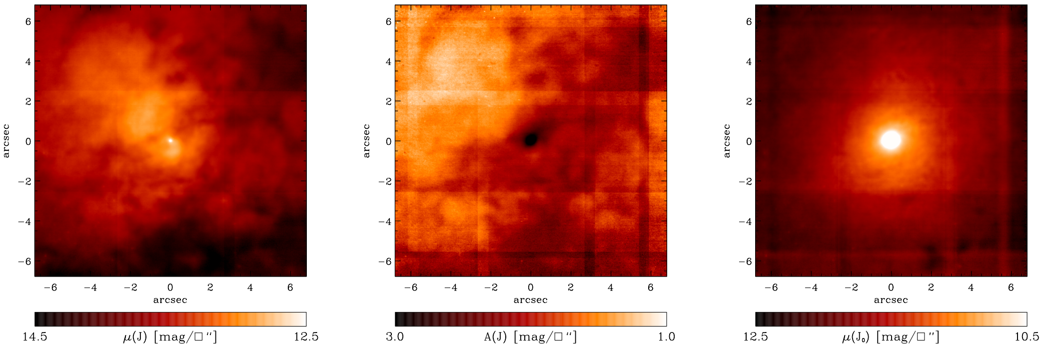

Figure 6.3 From left to right: observed J-band surface brightness, constructed J-band extinction map, A(J), and dust-corrected J-band surface brightness. The corrected image appears mostly smooth and symmetric.

The extinction map in V-band is constructed from the $(J-K)$ colour map and displayed in Figure 6.4. The extinction in the regions immediately surrounding the nucleus is $A(V) \sim 12-13$ mag, somewhat higher than the estimate of $A(V) \sim 7$ mag given by (Schreier et al. (1996)), but in excellent agreement with the value of ~ 14 mag deduced by Meisenheimer et al. (2007) from mid-infrared observations of the innermost parsec of Cen A. The extinction generally decreases from south to north, perpendicular to the dust lane, reaching values as low as $A(V) \sim 4$ mag.

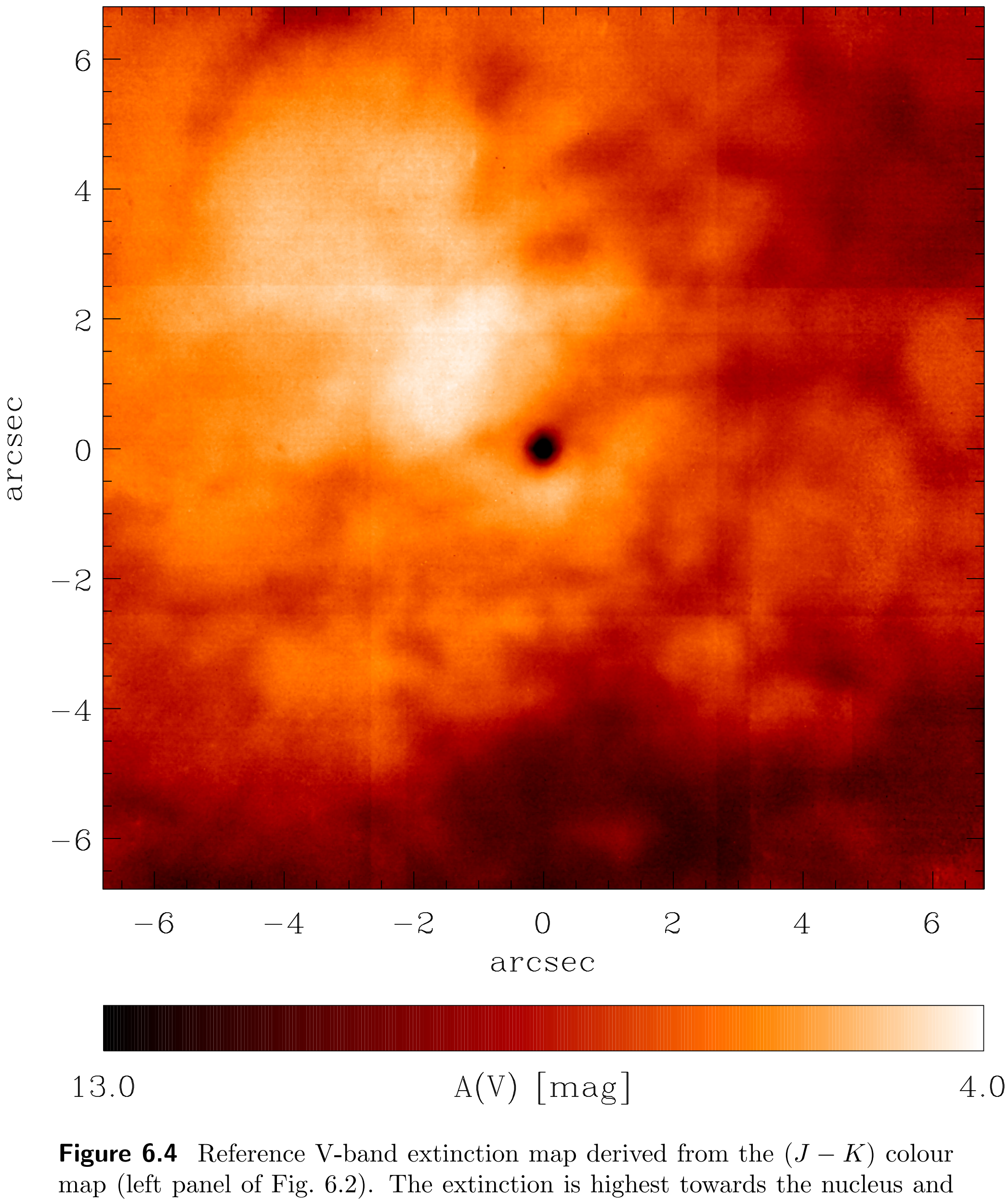

Figure 6.4 Reference V-band extinction map derived from the $(J-K)$ colour map (left panel of Fig. 6.2). The extinction is highest towards the nucleus and reaches values of $A(V) \sim 15$ mag in the dust lane SW of the nucleus.

6.5 Central star formation

In our medium depth K-band image we detect individual ‘clumps’ at a distance of 2 to 7 arcsecond from the nucleus (indicated by circles in Figure 6.5). To unveil the nature of these objects we measure their sizes, magnitudes and intrinsic colours - taking into account the reddening by the foreground dust layer, as derived in the previous section.

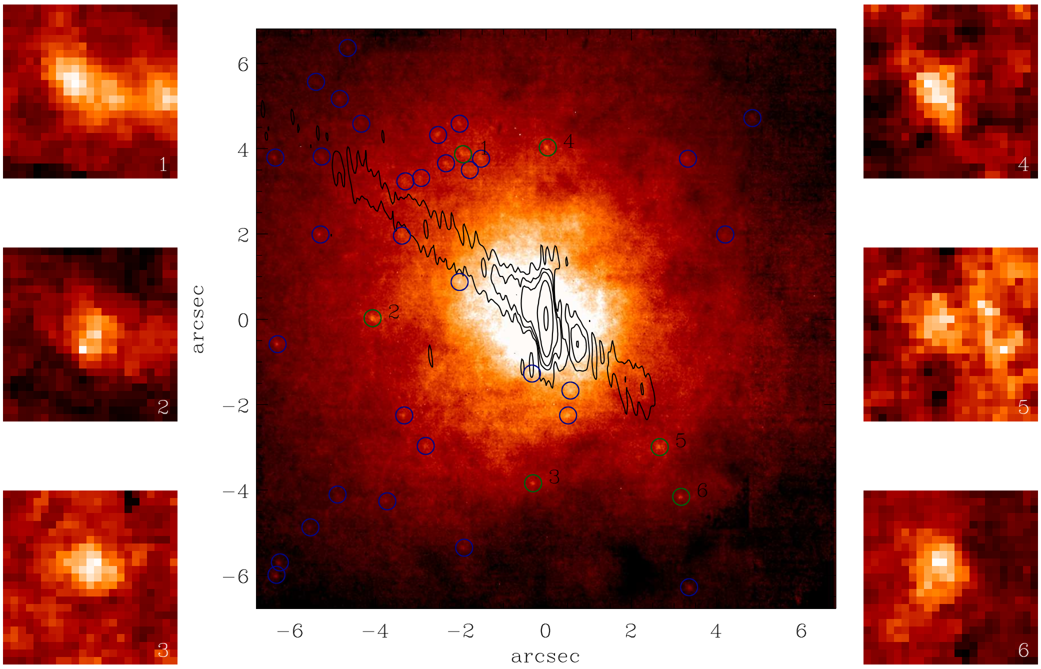

Figure 6.5 K-band image in logarithmic scaling. Indicated by circles are the stars, or star clusters that were identified by eye. The additional panels on the side give a zoom into the image for 6 objects indicated by the green circles and the according numbers. Overlain are the VLA image contours of the radio jet (Hardcastle private communication).

6.5.1 Sizes and magnitudes of the clumps

Figure 6.5 shows the K-band image in logarithmic scaling and the stars or star clusters that were identified by eye, are indicated by circles. The insets to the left and to the right zoom into 6 regions around the clumps indicated by green circles and the according numbers. The objects’ positions were identified in the K-band image, and they were re-identified at the same positions in the aligned H- and J-band images (were the alignment was performed relative to the position of the AGN).

To enhance the contrast of the sources and minimise the influence of the "background light" on the photometric measurements, the underlying galaxy light was subtracted via a smooth ellipse model (using the IRAF tasks *ellipse* and *bmodel*). The objects have a typical FWHM of $\sim 5-7$ pix in K-band, judging from Gaussian fits to the object in the background subtracted fields. This corresponds to $\sim 0\farcs7 - 0\farcs9$ or $\sim 1.1-1.5$ pc at a distance of 3.5 Mpc. Some of them show clumpy structures and seem to be marginally resolved.

To derive the intrinsic magnitudes and colours of the stars or star clusters, identified in the J-, H- and K-band images we extract their photon counts in a circular aperture centred on the de-reddened and background subtracted images. The aperture size was chosen as 2*FWHM of the objects. The typical intrinsic K-band magnitudes are in the range $K_0 = 20 - 16$.

6.5.2 Colour magnitude diagrams

The K_0 vs. $(H-K)_0$ colour magnitude diagram is shown in Figure 6.6 (left panel). There is a trend that brighter objects tend to be redder. For comparison, the right panel shows the colour-magnitude diagram of the Arches cluster (Stolte et al., 2005). It is corrected for differential reddening of the cluster stars, but not for the foreground extinction of $A(V) \sim 25$ mag, which translates to $E(H-K) \sim 1.8$ (using the extinction law presented in Section 6.4) and brings the intrinsic median colour of Arches to $(H-K)_0 \sim 0$.

It is important to note that the apparent K-band magnitudes are the same for the individual stars in Arches and for our clumps, although the distance modulus for the Arches cluster is ~ 14.5 and that for Cen A ~ 27.5 (for a distance of 8 kpc and 3.5 Mpc, respectively). The luminosity of the clumps is therefore a factor $\sim 1.5 \times 10^5$ higher than that of a star of the same apparent magnitude in the Arches cluster. On the other hand, this argument holds for all wavelengths and so, we may actually compare the intrinsic colours in the two plots, which are in comparable ranges of $-1 < (H-K)_0 < 0.5$.

The absolute K-band magnitude, M_K, is plotted vs. the intrinsic colour, $(J-K)_0$, in Figure 6.7 (left panel). For comparison the right panel shows the same diagram for ~ 500 bulge stars in M31 (Davidge et al., 2005). The solid lines are the RGB sequences for the globular clusters 47 Tuc and NGC 6528. The dashed lines show sequences for $M_{\rm bol}$ = -4 and -5, which were calculated using the bolometric corrections for Galactic bulge giants (see Davidge et al., 2005, for details).

Again, the range of the intrinsic colour $0.5 < (J-K)_0 < 2.5$ agrees well for the two plots, but the absolute magnitudes are on average ~ 3 mag brighter for our clumps than for individual stars in M31. The brightest supergiants in the bulge of M31 do not exceed $M_K = -8.5$, whereas the brightest object in our analysis has a magnitude $M_K \sim -12$, which corresponds to $\sim 1.3 \times 10^6 L_\odot$. Comparing the objects at similar absolute magnitudes of $M_K \sim -8$, one finds that the supergiants in M31 are on average redder by ~ 1 mag.

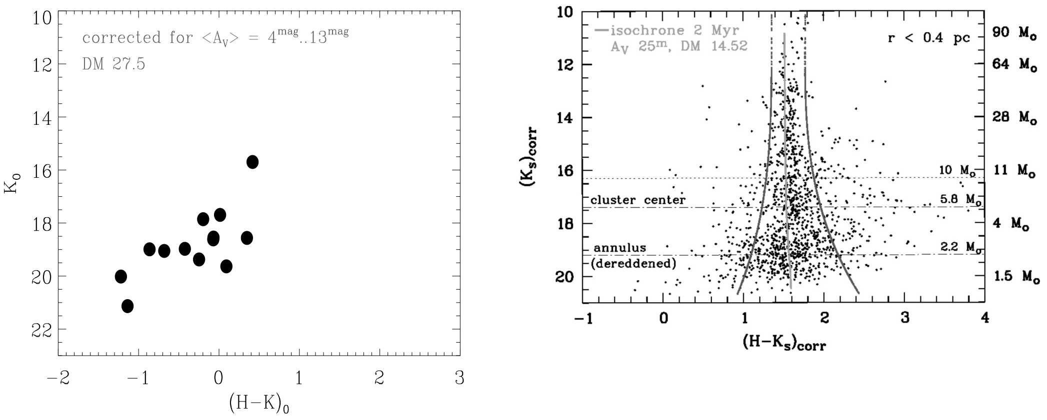

Figure 6.6 Colour-magnitude-diagram of K_0 vs. $(H-K)_0$ for the star clumps identified in the H- and K-band images (left panel). For comparison the colour-magnitude diagram of the Arches cluster is shown (Stolte et al., 2005) (right panel, not corrected for foreground extinction $E(H-K)\sim 1.8$). Note that the colours are plotted vs. apparent magnitudes. The difference in distance modulus of Cen A and the Arches cluster is ~ 13. The K-band luminosity of the clumps exceeds that of individual stars in the Arches cluster by $\sim 1.5\times 10^5$.

6.5.3 Individual stars or clusters?

Judging from the analysis of the size and brightness of the identified clumps, the most likely interpretation of their nature are star clusters. They are marginally resolved with sizes in the range $\sim 0\farcs7-0\farcs9$ corresponding to $\sim 1.1-1.5$ pc at a distance of 3.5 Mpc. Their overwhelmingly large luminosities of $\sim 3.0\times10^4-1.3\times 10^6\mathrm{L}_\odot$ make it very difficult to argue for individual stars. Although the "fainter" ones at $M_K\sim -6.5$ and -7.5 mag match the absolute magnitude of supergiants in the bulge of M31 (Davidge et al., 2005) and also young supergiants found in the halo of Cen A ($M_V=-7$, Rejkuba et al. 2002), and could well be of this type. However, their intrinsic $(J-K)_0$ colours differ by $\gtrsim 1$ mag, suggesting that our clumps are too blue for being asymptotic giant branch stars.

The comparison to the colour-magnitude diagram of the Arches cluster (Figure 6.6 taken from Stolte et al. 2005), and the excellent agreement of the spanned colour range (after correcting the Arches cluster for foreground extinction of $A(V)\sim$ 25 mag, $E(H-K)\sim 1.8$), leads us to speculate that we indeed observe young starburst clusters. With a distant modulus of 14.5, a typical member of the Arches cluster ($m_{K_0}\sim 13$) has a total magnitude of $M_K\sim -1.5$. Taking the absolute magnitude of the sun in K-band ($M_{K,\odot}=3.3$, Allen 1976), one derives a K-band luminosity of $\sim 100\,\mathrm{L}_\odot$. To make up the luminosity observed in our (presumable) star clusters we need typically $\sim 500-6500$ stars, which is in very good agreement with the star counts found in young clusters (e.g. ~2100 in NGC 3603, and ~1400 in the Arches cluster Stolte 2003).

It is difficult to derive the age of the clusters, since we do not resolve their stellar

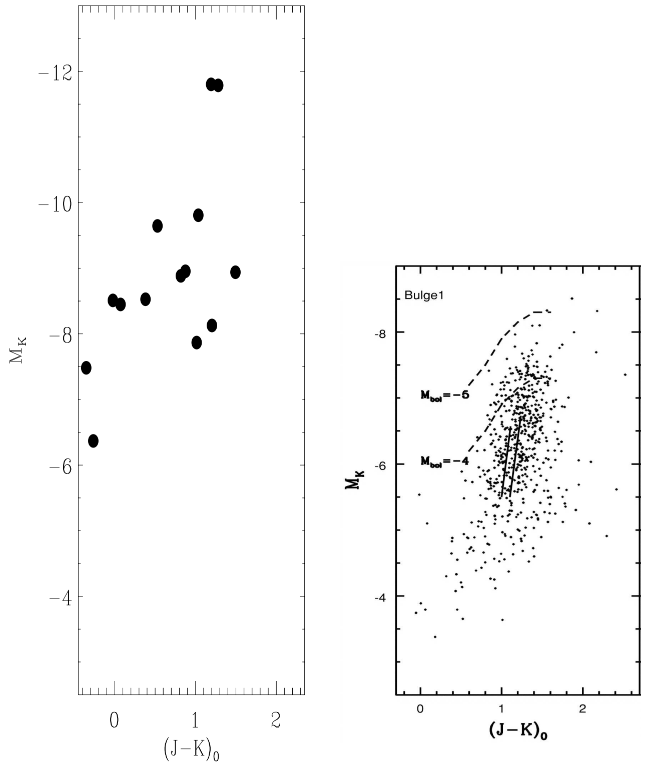

Figure 6.7 $[M_K\ (J-K)_0]$ colour-magnitude diagrams, for the objects of our study (left) and $\sim$ 500 bulge stars in M31 (right, taken from Davidge et al. 2005). Note that the objects in the left panel are $\sim$ 3 mag brighter.

populations. If we were to assume that they are indeed comparable in nature to the young massive clusters close to the Galactic centre (as NGC 3603 and the Arches cluster), their ages are in the range $\sim 1-5$ Myr.

According to the analysis of the recent halo star formation in Cen A at a distance of $\gtrsim 9'$ ($\sim$ 9 kpc) from the nucleus (Rejkuba et al., 2002), the brightest stars in the blue main sequence (extending to magnitudes of $M_V = -7$) are lying along the 10^7-yr-old isochrone.

We conclude that in both cases - either being young star clusters or supergiants - these luminous red objects have formed fairly recently, in an estimated timescale of $\sim 1 \times 10^6$ to $\sim 1 \times 10^7$ yrs. Their formation is thus not immediately linked to the merger event of a spiral galaxy with NGC 5128 that occurred approximately 10^8 yrs ago (Quillen et al., 1993; Peng et al., 2002). However, young star clusters are not common in elliptical galaxies and may be an implicate consequence of the merger of Cen A with a spiral galaxy, that provided ample gas supply for recurring star formation.

6.6 The influence of the jet

Rejkuba et al. (2002) find an alignment of young blue stars with the radio jet in Cen A over > 10 kpc (at a distance of $\gtrsim 9' \approx 9$ kpc from the nucleus). They conclude that the jet triggered star formation in the halo of NGC 5128, when hitting dense clouds of neutral gas left in the halo by the previous accretion event (Schiminovich et al., 1994; Charmandaris et al., 2000).

The distribution of our star clusters appears to be slightly more crowded towards the North-East, close to the projected direction of the radio jet (compare Figure 6.5). The histogram in Figure 6.8 shows the number of clumps inside a wedge of a certain opening angle around the jet, spaced by 10°. This histogram shows two peaks. The highest fraction of clumps are found very close to the jet (at $0° - 10°$) and perpendicular to it (at $80° - 90°$).

This could indicate that the clumps are either associated with the jet or the dust lane (the molecular gas disk) that lies approximately perpendicular to the jet (see Figure 6.9). However, the current selection of the objects was done by eye, and is biased towards the brightest clumps and therefore not complete. The influence of the jet on the formation of these objects is tantalising but at present the analysis is rather inconclusive.

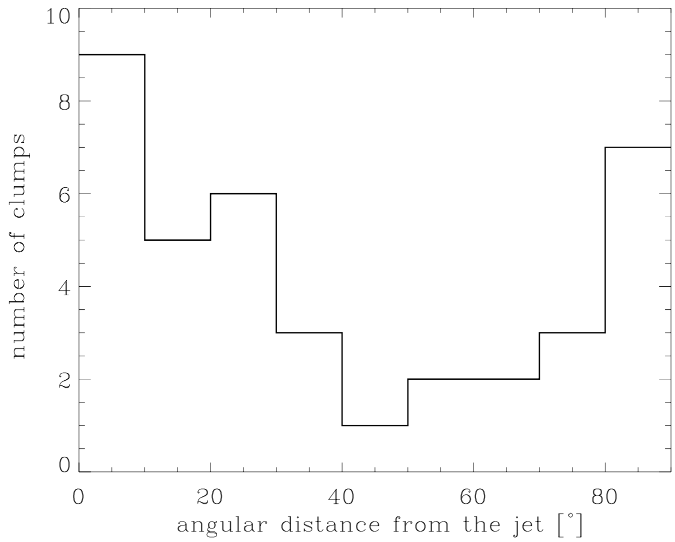

Figure 6.8 The number of detected clumps is plotted vs the distance to the radio jet (in steps of ±10°).

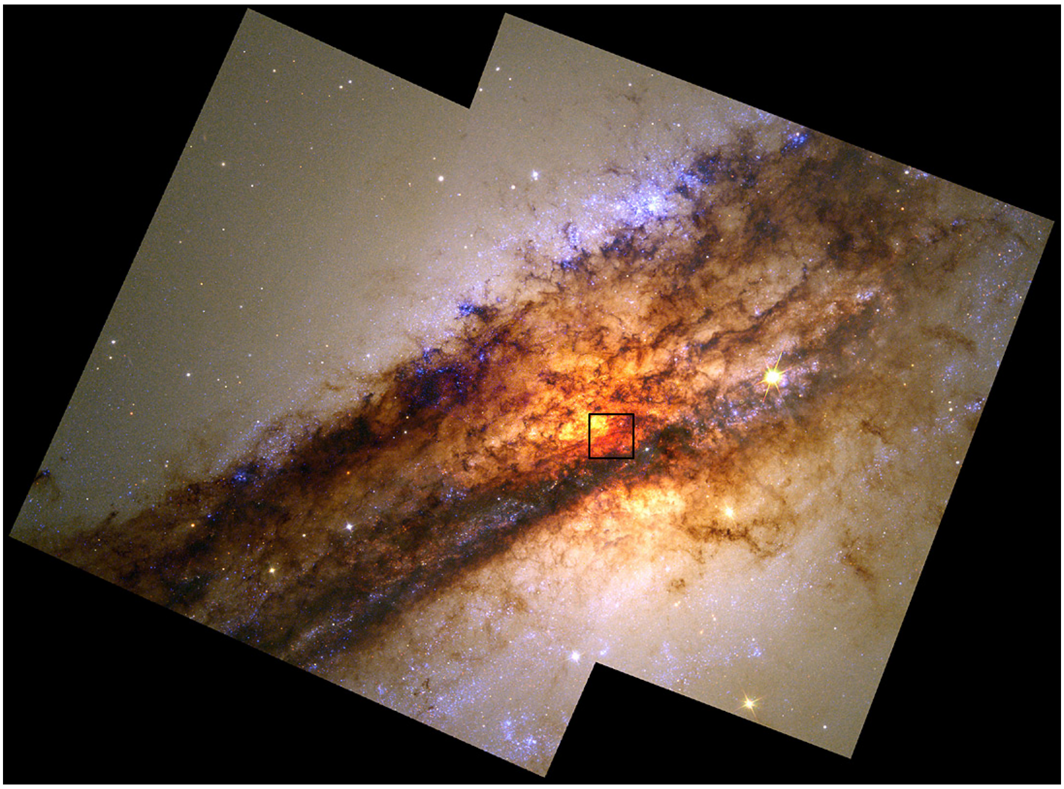

Figure 6.9 True colour RGB image (Red = F814W, Green = F555W, and Blue = F336W) taken with the HST/WFPC2 (Marconi et al., 2000). The box indicates our NaCo field of view. Note that the nucleus is not visible up to I-band (F814W).

6.7 Summary and Discussion

The central $\sim 13" \times 13"$ around the nucleus of Cen A are heavily extinct by the prominent dust lane that crosses the galaxy's centre. The amount of extinction in this region is in the range $4-13$ mag, according to the extinction map (Fig. 6.4). This extinction map was used to obtain the intrinsic light distribution in the J-, H- and K-band. Using these intrinsic images, the magnitudes of (presumable) star clusters were measured in J_0, H_0, and K_0, and their intrinsic colours were derived. The main assumptions that underly our simple, zero-order extinction correction are that i) the dust is located in a foreground screen, ii) Cen A has an intrinsic colour similar to elliptical galaxies, and iii) no significant colour gradients are present throughout the field of view. These are very strong assumptions, that might not be fulfilled for the detected objects. Indeed, these objects might suffer from additional, differential reddening (due to embedded stars). To improve on the extinction correction, we would have to de-redden each cluster - and for resolved clusters each star - individually. As it is done for the resolved stellar populations in nearby star clusters, by shifting the stars back onto the main sequence along the reddening vector.

With the photometric data that we have at hand, it is difficult to make a conclusive statement about the nature of the detected clumps. They appear to be marginally resolved and are consistent with young star clusters, given their near-infrared colours and luminosities. To improve our analysis, it would be necessary to get deeper images at the best possible spatial resolution. This would enable us to resolve the fainter stars in the (presumable) star clusters and improve on the photometric measurements. However, the lack of possible reference stars for adaptive optics observations in the vicinity of Cen A, forces us to guide on the nucleus in K-band (using the IR WFS). This ensures the best-possible wavefront correction close to the nucleus, but makes K-band observations very expensive (as 90% of the light are consumed by the wavefront correction). This problem will be overcome with the advent of the laser guide star facility (LGSF) available with Naos-Conica.

The current state of analysis leads us to conclude that we detect young star clusters in the central $R < 7$" region around the active galactic nucleus of Cen A. Their intrinsic colours are in the range $-1 < (H - K)_0 < 0.5$, in good agreement with the young starburst clusters close to the Galactic centre (Stolte, 2003; Stolte et al., 2005).

The abundance of identified clusters seems to be highest towards the projected position of the radio jet. This finding hints towards jet induced star formation on scales of ~ 70 pc, as observed for young halo stars in Cen A on much larger scales ($\sim 9 - 19$ kpc Rejkuba et al. 2002).

7. Conclusions

At a distance of less than 4 Mpc, Centaurus A is the nearest recent merger, the nearest massive elliptical and the nearest radio galaxy. It's nucleus is a unique laboratory to study in great detail the connection between merging, massive black holes, AGN activity, and jet- and merger induced star formation.

We use the adaptive-optics (AO) assisted instruments Naos-Conica and SINFONI at the VLT to obtain near-infrared data at unprecedented spatial resolution, making this work a pilot study in several ways.

Using these data we perform rigorous kinematical modelling of the [Fe II] and H_2 gas motion inside the central $\sim 1" \times 1"$ (corresponding to $\sim 17\mathrm{pc} \times 17\mathrm{pc}$). We demonstrate that black hole mass modelling can be done with AO data.
We show that it is possible to reach the diffraction limit of an 8m class telescope while guiding on the AGN in a heavily obscured galaxy. Our K-band imaging data have a spatial resolution of $0\farcs06$ ($\sim$ 1pc) measured as the FWHM of the unresolved nuclear point source, outperforming the HST by a factor of 4 in near-infrared wavelengths.

The radius of influence of Cen A's black hole is well resolved. The best possible measure on $r_{\mathrm{BH}} \sim 1"$ comes from the H_2 SINFONI data, that clearly show the dominating region of the black hole. The very clean and symmetric H_2 velocity field makes Cen A appear like a textbook example of a nuclear gas disk, and enables us to determine the black hole mass almost without any dynamical model. The radius where the rotational velocity reaches a minimum corresponds to the radius which encloses as much stellar mass as black hole mass. These simple considerations lead to $M_{\mathrm{BH}} \sim 7.5 \times 10^7 M_\odot$.
However, a dynamical model is still useful to show that the observations are generally consistent with the model assumptions (also as an example for other galaxies), and is moreover important to quantify errors.

We construct a detailed gas dynamical model under the assumption that the gas moves in a disk under the influence of the combined potential of the stars and the central black hole. We carefully account for the complex AO-PSF. Our gas

kinematical data are best modelled via a hot-disk model, that includes the high gas velocity dispersion via a pressure term in the axisymmetric, isotropic Jeans' equation.
We demonstrate how important the gas physics is, even in light of high resolution data, and that integral-field-unit data are crucial to identify non-gravitational motions in the gas velocity field.

The imaging spectroscopy data give additional evidence for a warped disk structure. This warped disk has a median inclination angle of $\sim 27° \pm 5°$ and its mean position angle is 155° with twists of $\pm 14°$. This is in agreement with an orthogonal jet-disk picture.

The IFU data exhibit a wealth of information on different gas species. We find that depending on their ionisation level, different gas species display different flux distributions and velocity structures. High-excitation lines are strongly influenced - possibly created - by the jet. As judging from the comparison of [Si VI] and H_2 velocity fields, we clearly see interactions of the jet with gas clouds in the case of [Si VI]. The position of its maximum interaction is coincident with a knot in the radio jet.

While it has traditionally been believed that the narrow-line region (NLR) clouds are photoionised by the central source, our high spatial resolution integral field unit data indicate that NLR clouds may instead be predominantly shock-excited by energetic thermal and non-thermal mass outflows from the central object. Strong dynamical interactions between the emission-line gas and radio-emitting ejecta can be explained if the NLR is formed from shells of ambient interstellar medium swept up and compressed by the supersonic expansion of hot gas heated by interactions with the advancing radio jet.

The influence of the radio jet becomes less clear, if not negligible, for low-ionisation species and especially molecular hydrogen gas, which seems to be well settled in a disk. We safely use their kinematics as a tracer for the nuclear potential.
From our Naos-Conica long-slit [FeII] velocity curves at 4 position angles, and from the 2D H_2 velocity field extracted from the SINFONI data we get consistent M_{BH} values with the best-fit of $M_{BH} = (7.0 \pm 3.0) \times 10^7 M_\odot$. With this revised value of M_{BH} from high-resolution gas dynamical studies, the former offset of Cen A to the $M_{BH} - \sigma$ relation is greatly reduced, almost including the predicted value inside the 3σ error bar (see Figure 7.1).
Under the same modelling assumptions as Marconi et al. (2001) (i.e. ignoring the high velocity dispersion of the gas) we get $M_{BH} \sim 4 \times 10^7 M_\odot$, which is a factor 5 lower than their value, and in excellent agreement with the $M_{BH} - \sigma$ relation.

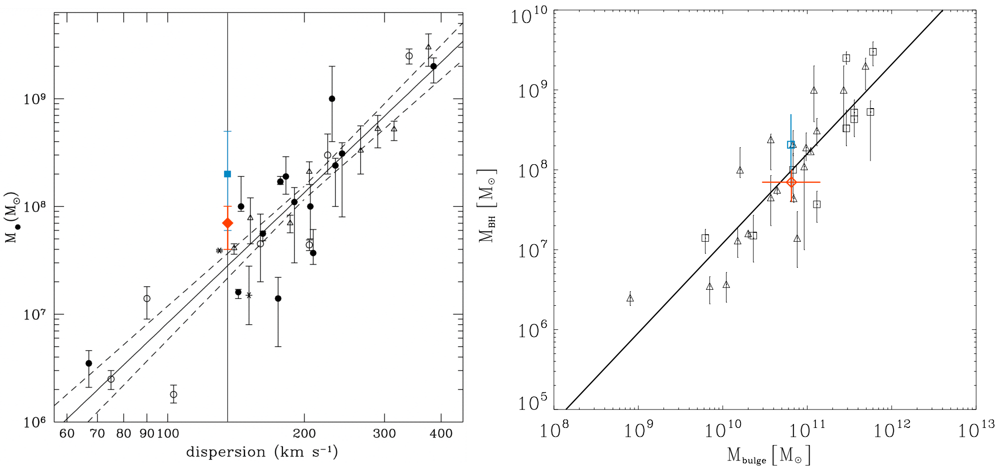

Figure 7.1 Position of Cen A on the $\mathrm{M_{BH}}$–σ and $\mathrm{M_{BH}} - \mathrm{M_{bulge}}$ relation, with the mass determination derived by Marconi et al. (2001) (blue square) and the result of this thesis (red diamond). Cen A's offset to the $\mathrm{M_{BH}}$–σ relation is greatly reduced (right panel, adopted from Tremaine et al. 2002). Cen A is in perfect agreement with the $\mathrm{M_{BH}} - \mathrm{M_{bulge}}$ relation (Häring and Rix, 2004).

As shown for comparison in Figure 7.1, Cen A was, and still is, in perfect agreement with the relation of black hole mass and bulge mass.

The JHK images reveal the presence of marginally resolved stellar clusters with typical sizes of ~ 1.5 pc in the central < 7" region around the active galactic nucleus of Cen A. Their intrinsic colours are in the range $-1 < (H - K)_0 < 0.5$, in good agreement with the young starburst clusters close to the Galactic centre, which have ages in the range $1 - 5$ Myr.
The abundance of identified clusters seems to be higher close to the projected position of the radio jet. This finding hints towards jet induced star formation on scales of ~ 70 pc, as observed before for young halo stars in Cen A on much larger scales ($\sim 9 - 19$ kpc).

8. Outlook

In this chapter I want to glance at some results that have not been laid out in this thesis but result from collaborative work.

8.1 SINFONI stellar kinematics and modelling[1]

The stellar kinematics, extracted from the SINFONI data, are presented in Figure 8.1. The mean velocity, v, (upper left panel) shows counter-rotation with respect to the H_2 gas, however, the zero velocity curves do not seem to be well aligned. The decoupling of angular momenta of gas and stars in (elliptical) galaxies gives evidence for the acquisition of external material by these galaxies later in their history (e.g. Bertola et al., 1988). This is perfectly in line with the overall appearance of Centaurus A, having undergone a recent merger event.

We will construct general dynamical models for the stellar kinematics using the axisymmetric Schwarzschild orbital-superposition method (e.g. Rix et al., 1997) optimised for 2D-binned integral-field data (e.g. Cappellari et al., 2004). The full line-of-sight velocity distribution will be used to constrain the models and break degeneracy between the mass and the orbital anisotropy in the dynamical models. Integral-field kinematics allows the constraints on the black hole mass, derived from dynamical models, to be significantly tightened compared to long-slit observations. The new data will thus provide a very stringent comparison between the black hole mass derived from the stellar and gas kinematics. This comparison of a black hole mass determination with two independent methods is quite important as only a couple of them have been performed, and in half of the cases with negative results (e.g. Cappellari et al., 2002).

---

[1] presented in Cappellari et al. in prep.

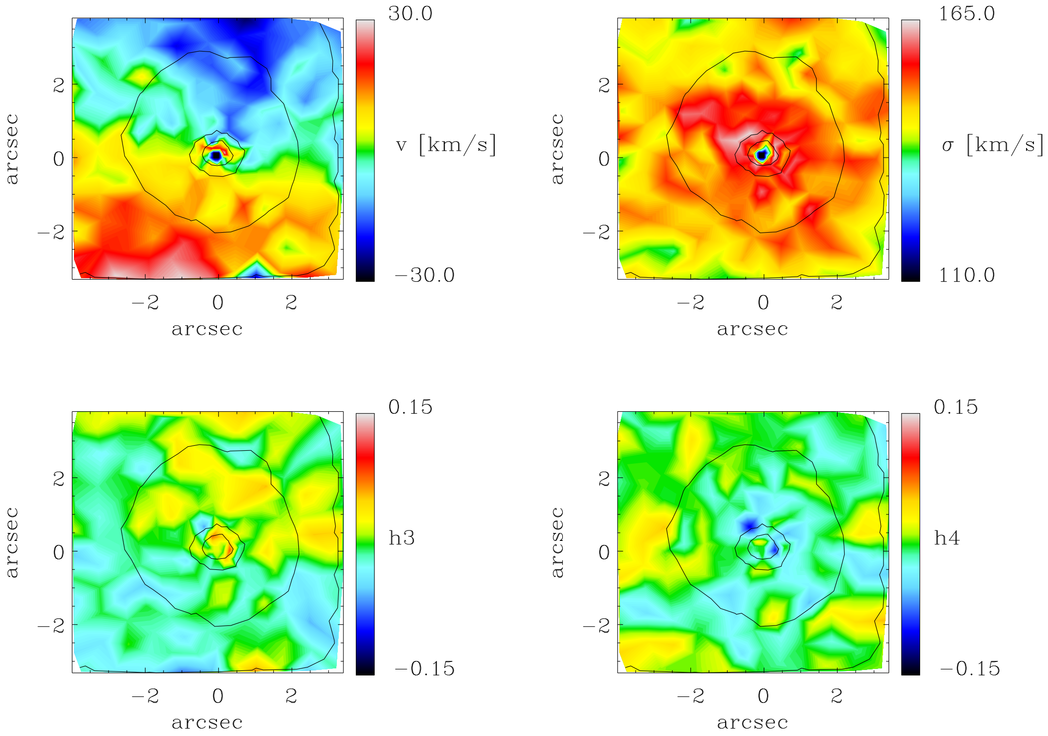

Figure 8.1 The stellar kinematics (given as the velocity v, velocity dispersion σ, and the higher order Gauss-Hermite coefficients, h_3 and h_4) extracted from the $8'' \times 8''$ data cube. Note that the stars counter-rotate wrt the H_2 gas. Yet, the symmetry axes are not well aligned

8.2 Resolving the innermost parsec of Cen A at mid-infrared wavelengths[2]

The spectral energy distribution of Cen A's nucleus can be explained by a synchrotron spectrum plus an additional component from hot dust, contributing to the mid-infrared radiation. The strong synchrotron core of Centaurus A can be explained as the result of an exceptionally strong interaction of the jet with its surroundings on sub-parsec scales, which might be connected with the fact, that Centaurus A is in an intermediate state between high accretion efficiency (standard accretion disk) and the much less efficient Advection Dominated Accretion Flows (ADAF). The existence of such objects challenges the concept of unified schemes which simply rely on orientation.

With mid-infrared interferometric observations obtained with MIDI at the VLT, it was possible to resolve an extended dust structure at a P.A.$=127° \pm 9°$,

---

[2] presented in Meisenheimer et al. 2007

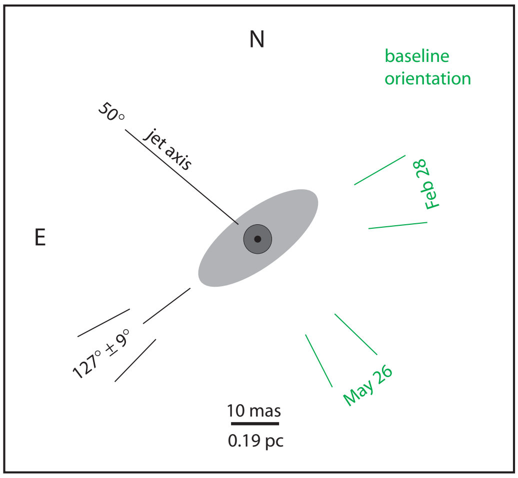

Figure 8.2 Sketch of the model for the mid-infrared emission from the inner parsec of Cen A as observed with MIDI. We identify the unresolved point source of < 6 mas FWHM (dark grey) with the VLBI core (FWHM $= 0.5 \pm 0.1$ mas, indicated as a black dot). It is surrounded by an elongated structure of dust emission (light grey) the major axis of which is oriented along P.A.$=127° \pm 9°$ as inferred from the orthogonal baselines observed. From the visibilities a major axis length of about 30 mas is derived. Note that the major axis orientation is consistent with being perpendicular to the radio jet axis

suggestive to be a disk of dust at a temperature of ~ 240 K. Its appearance is sketched in Figure 8.2. The orientation of the disk is in perfect agreement with an orthogonal disk-jet picture. The position angle of its major axis agrees well with the orientation of our ‘larger’ scale disk in molecular hydrogen.

Bibliography

C. W. Allen. *Astrophysical Quantities.* Astrophysical Quantities, London: Athlone (3rd edition), 1976, 1976.

W. Baade and R. Minkowski. On the Indentification of Radio Sources. *ApJ*, 119: 215, 1954.

A. J. Barth, M. Sarzi, H.-W. Rix, L. C. Ho, A. V. Filippenko, and W. L. W. Sargent. Evidence for a Supermassive Black Hole in the S0 Galaxy NGC 3245. *ApJ*, 555:685–708, 2001.

K. G. Begeman. *Ph.D. Thesis*, 1987.

E. F. Bell, C. Papovich, C. Wolf, E. Le Floc'h, J. A. R. Caldwell, M. Barden, E. Egami, D. H. McIntosh, K. Meisenheimer, P. G. Pérez-González, G. H. Rieke, M. J. Rieke, J. R. Rigby, and H.-W. Rix. Toward an Understanding of the Rapid Decline of the Cosmic Star Formation Rate. *ApJ*, 625:23–36, 2005.

E. F. Bell, S. Phleps, R. S. Somerville, C. Wolf, A. Borch, and K. Meisenheimer. The Merger Rate of Massive Galaxies. *ApJ*, 652:270–276, 2006.

F. Bertola, L. M. Buson, and W. W. Zeilinger. Counter-rotation in dust-lane ellipticals and the implications for accretion events in galaxies. *Nature*, 335:705, 1988.

F. Bertola, M. Cappellari, J. G. Funes, E. M. Corsini, A. Pizzella, and J. C. Vega Beltrán. Circumnuclear Keplerian Disks in Galaxies. *ApJ*, 509:L93–L96, 1998.

J. Binney and M. Merrifield. *Galactic astronomy.* Galactic astronomy / James Binney and Michael Merrifield. Princeton, NJ : Princeton University Press, 1998. (Princeton series in astrophysics) QB857 .B522 1998 ($35.00), 1998.

J. Binney and S. Tremaine. *Galactic dynamics.* Princeton, NJ, Princeton University Press, 1987, 747 p., 1987.

H. Bonnet, R. Abuter, A. Baker, W. Bornemann, A. Brown, R. Castillo, R. Conzelmann, R. Damster, R. Davies, B. Delabre, R. Donaldson, C. Dumas, F. Eisenhauer, E. Elswijk, E. Fedrigo, G. Finger, H. Gemperlein, R. Genzel, A. Gilbert,

G. Gillet, A. Goldbrunner, M. Horrobin, R. Ter Horst, S. Huber, N. Hubin, C. Iserlohe, A. Kaufer, M. Kissler-Patig, J. Kragt, G. Kroes, M. Lehnert, W. Lieb, J. Liske, J.-L. Lizon, D. Lutz, A. Modigliani, G. Monnet, N. Nesvadba, J. Patig, J. Pragt, J. Reunanen, C. Röhrle, S. Rossi, R. Schmutzer, T. Schoenmaker, J. Schreiber, S. Stroebele, T. Szeifert, L. Tacconi, M. Tecza, N. Thatte, S. Tordo, P. van der Werf, and H. Weisz. First Light of SINFONI at the VLT. *The Messenger*, 117:17, 2004.

H. Bonnet, S. Ströbele, F. Biancat-Marchet, J. Brynnel, R. D. Conzelmann, B. Delabre, R. Donaldson, J. Farinato, E. Fedrigo, N. N. Hubin, M. E. Kasper, and M. Kissler-Patig. Implementation of MACAO for SINFONI at the VLT, in NGS and LGS modes. In P. L. Wizinowich and D. Bonaccini, editors, *Adaptive Optical System Technologies II. Edited by Wizinowich, Peter L.; Bonaccini, Domenico. Proceedings of the SPIE, Volume 4839, pp. 329-343 (2003).*, pages 329–343, 2003.

B. J. Boyle, T. Shanks, S. M. Croom, R. J. Smith, L. Miller, N. Loaring, and C. Heymans. The 2dF QSO Redshift Survey - I. The optical luminosity function of quasi-stellar objects. *MNRAS*, 317:1014–1022, 2000.

M. Cappellari. Efficient multi-Gaussian expansion of galaxies. *MNRAS*, 333:400–410, 2002.

M. Cappellari, R. Bacon, M. Bureau, M. C. Damen, R. L. Davies, P. T. de Zeeuw, E. Emsellem, J. Falcón-Barroso, D. Krajnović, H. Kuntschner, R. M. McDermid, R. F. Peletier, M. Sarzi, R. C. E. van den Bosch, and G. van de Ven. The SAURON project - IV. The mass-to-light ratio, the virial mass estimator and the Fundamental Plane of elliptical and lenticular galaxies. *MNRAS*, 366:1126–1150, 2006.

M. Cappellari and E. Emsellem. Parametric Recovery of Line-of-Sight Velocity Distributions from Absorption-Line Spectra of Galaxies via Penalized Likelihood. *PASP*, 116:138–147, 2004.

M. Cappellari, R. C. E. van den Bosch, E. K. Verolme, R. Bacon, M. Bureau, Y. Copin, R. L. Davies, E. Emsellem, D. Krajnovic, H. Kuntschner, R. McDermid, B. W. Miller, R. F. Peletier, and P. T. de Zeeuw. Dynamical Modeling of SAURON Galaxies. In L. C. Ho, editor, *Coevolution of Black Holes and Galaxies*, 2004.

M. Cappellari, E. K. Verolme, R. P. van der Marel, G. A. V. Kleijn, G. D. Illingworth, M. Franx, C. M. Carollo, and P. T. de Zeeuw. The Counterrotating Core and the Black Hole Mass of IC 1459. *ApJ*, 578:787–805, 2002.

J. A. Cardelli, G. C. Clayton, and J. S. Mathis. The relationship between infrared, optical, and ultraviolet extinction. *ApJ*, 345:245–256, 1989.

C. L. Carilli, R. A. Perley, and J. H. Dreher. Discovery of the bow shock of Cygnus A. *ApJ*, 334:L73–L76, 1988.

F. H. Chaffee, C. B. Foltz, P. C. Hewett, P. A. Francis, R. J. Weymann, S. L. Morris, S. F. Anderson, and G. M. MacAlpine. The large, bright QSO survey. IV - QSOs in two equatorial fields. *AJ*, 102:461–487, 1991.

V. Charmandaris, F. Combes, and J. M. van der Hulst. First detection of molecular gas in the shells of CenA. *A&A*, 356:L1–L4, 2000.

D. A. Clarke, J. O. Burns, and M. L. Norman. VLA observations of the inner lobes of Centaurus A. *ApJ*, 395:444–452, 1992.

N. Cretton and E. Emsellem. On the reliability of the black hole mass and mass-to-light ratio determinations with Schwarzschild models. *MNRAS*, 347:L31–L35, 2004.

R. M. Cutri, M. F. Skrutskie, S. van Dyk, C. A. Beichman, J. M. Carpenter, T. Chester, L. Cambresy, T. Evans, J. Fowler, J. Gizis, E. Howard, J. Huchra, T. Jarrett, E. L. Kopan, J. D. Kirkpatrick, R. M. Light, K. A. Marsh, H. McCallon, S. Schneider, R. Stiening, M. Sykes, M. Weinberg, W. A. Wheaton, S. Wheelock, and N. Zacarias. *2MASS All Sky Catalog of point sources.* The IRSA 2MASS All-Sky Point Source Catalog, NASA/IPAC Infrared Science Archive. http://irsa.ipac.caltech.edu/applications/Gator/, 2003.

T. J. Davidge, K. A. G. Olsen, R. Blum, A. W. Stephens, and F. Rigaut. Deep ALTAIR+NIRI Imaging of the Disk and Bulge of M31. *AJ*, 129:201–219, 2005.

T. Di Matteo, V. Springel, and L. Hernquist. Energy input from quasars regulates the growth and activity of black holes and their host galaxies. *Nature*, 433: 604–607, 2005.

F. Eisenhauer, R. Abuter, K. Bickert, F. Biancat-Marchet, H. Bonnet, J. Brynnel, R. D. Conzelmann, B. Delabre, R. Donaldson, J. Farinato, E. Fedrigo, R. Genzel, N. N. Hubin, C. Iserlohe, M. E. Kasper, M. Kissler-Patig, G. J. Monnet, C. Roehrle, J. Schreiber, S. Stroebele, M. Tecza, N. A. Thatte, and H. Weisz. SINFONI - Integral field spectroscopy at 50 milli-arcsecond resolution with the ESO VLT. In M. Iye and A. F. M. Moorwood, editors, *Instrument Design and Performance for Optical/Infrared Ground-based Telescopes. Edited by Iye, Masanori; Moorwood, Alan F. M. Proceedings of the SPIE, Volume 4841, pp. 1548-1561 (2003).*, pages 1548–1561, 2003a.

F. Eisenhauer, M. Tecza, N. Thatte, R. Genzel, R. Abuter, C. Iserlohe, J. Schreiber, S. Huber, C. Roehrle, M. Horrobin, A. Schegerer, A. J. Baker, R. Bender, R. Davies, M. Lehnert, D. Lutz, N. Nesvadba, T. Ott, S. Seitz,

R. Schoedel, L. J. Tacconi, H. Bonnet, R. Castillo, R. Conzelmann, R. Donaldson, G. Finger, G. Gillet, N. Hubin, M. Kissler-Patig, J.-L. Lizon, G. Monnet, and S. Stroebele. The Universe in 3D: First Observations with SPIFFI, the Infrared Integral Field Spectrometer for the VLT. *The Messenger*, 113:17–25, 2003b.

E. Emsellem, G. Monnet, and R. Bacon. The multi-gaussian expansion method: a tool for building realistic photometric and kinematical models of stellar systems I. The formalism. *A&A*, 285:723–738, 1994.

B. L. Fanaroff and J. M. Riley. The morphology of extragalactic radio sources of high and low luminosity. *MNRAS*, 167:31P–36P, 1974.

L. Ferrarese and H. Ford. Supermassive Black Holes in Galactic Nuclei: Past, Present and Future Research. *Space Science Reviews*, 116:523–624, 2005.

L. Ferrarese and D. Merritt. A Fundamental Relation between Supermassive Black Holes and Their Host Galaxies. *ApJ*, 539:L9–L12, 2000.

K. Gebhardt, R. Bender, G. Bower, A. Dressler, S. M. Faber, A. V. Filippenko, R. Green, C. Grillmair, L. C. Ho, J. Kormendy, T. R. Lauer, J. Magorrian, J. Pinkney, D. Richstone, and S. Tremaine. A Relationship between Nuclear Black Hole Mass and Galaxy Velocity Dispersion. *ApJ*, 539:L13–L16, 2000.

R. Genzel, R. Schödel, T. Ott, F. Eisenhauer, R. Hofmann, M. Lehnert, A. Eckart, T. Alexander, A. Sternberg, R. Lenzen, Y. Clénet, F. Lacombe, D. Rouan, A. Renzini, and L. E. Tacconi-Garman. The Stellar Cusp around the Supermassive Black Hole in the Galactic Center. *ApJ*, 594:812–832, 2003.

O. E. Gerhard. Line-of-sight velocity profiles in spherical galaxies: breaking the degeneracy between anisotropy and mass. *MNRAS*, 265:213, 1993.

G. L. Granato, G. De Zotti, L. Silva, A. Bressan, and L. Danese. A Physical Model for the Coevolution of QSOs and Their Spheroidal Hosts. *ApJ*, 600: 580–594, 2004.

M. J. Hardcastle, D. M. Worrall, R. P. Kraft, W. R. Forman, C. Jones, and S. S. Murray. Radio and X-Ray Observations of the Jet in Centaurus A. *ApJ*, 593: 169–183, 2003.

N. Häring and H.-W. Rix. On the Black Hole Mass-Bulge Mass Relation. *ApJ*, 604:L89–L92, 2004.

N. Häring-Neumayer, M. Cappellari, H.-W. Rix, M. Hartung, M. A. Prieto, K. Meisenheimer, and R. Lenzen. VLT Diffraction-limited Imaging and Spectroscopy in the NIR: Weighing the Black Hole in Centaurus A with NACO. *ApJ*, 643:226–237, 2006.

G. L. H. Harris and W. E. Harris. The Halo Stars in NGC 5128. II. An Outer Halo Field and a New Metallicity Distribution. *AJ*, 120:2423–2436, 2000.

G. L. H. Harris, W. E. Harris, and G. B. Poole. The Metallicity Distribution in the Halo Stars of NGC 5128: Implications for Galaxy Formation. *AJ*, 117:855–867, 1999.

J. Hartmann. Bemerkungen über den Bau und die Justierung von Spektrographen. *Zeitschrift für Instrumentenkunde*, 24:1, 1900.

T. M. Heckman. Star Formation in Active Galaxies: A Spectroscopic Perspective. In L. C. Ho, editor, *Coevolution of Black Holes and Galaxies*, pages 358–+, 2004.

P. C. Hewett, C. B. Foltz, and F. H. Chaffee. The evolution of bright, optically selected QSOs. *ApJ*, 406:L43–L46, 1993.

L. C. Ho. AGNs and Starbursts: What Is the Real Connection? *ArXiv Astrophysics e-prints*, 2005.

A. M. Hopkins and J. F. Beacom. On the Normalization of the Cosmic Star Formation History. *ApJ*, 651:142–154, November 2006.

P. F. Hopkins, L. Hernquist, T. J. Cox, T. Di Matteo, B. Robertson, and V. Springel. A Unified, Merger-driven Model of the Origin of Starbursts, Quasars, the Cosmic X-Ray Background, Supermassive Black Holes, and Galaxy Spheroids. *ApJS*, 163:1–49, 2006a.

P. F. Hopkins, R. S. Somerville, L. Hernquist, T. J. Cox, B. Robertson, and Y. Li. The Relation between Quasar and Merging Galaxy Luminosity Functions and the Merger-driven Star Formation History of the Universe. *ApJ*, 652:864–888, 2006b.

F. Hoyle and W. A. Fowler. Nature of Strong Radio Sources. *Nature*, 197:533, 1963.

X. Hui, H. C. Ford, R. Ciardullo, and G. H. Jacoby. The planetary nebula system and dynamics of NGC 5128. I - Planetary nebulae as standard candles. *ApJ*, 414:463–473, 1993.

L. K. Hunt, M. A. Malkan, M. Salvati, N. Mandolesi, E. Palazzi, and R. Wade. The Disks of Galaxies with Seyfert and Starburst Nuclei. I. Near-Infrared Colors and Color Gradients. *ApJS*, 108:229, 1997.

C. D. Impey, C. G. Wynn-Williams, and E. E. Becklin. Infrared studies of elliptical galaxies. I - an optically selected sample. *ApJ*, 309:572–592, 1986.

F. P. Israel. Centaurus A - NGC 5128. *A&A Rev.*, 8:237–278, 1998.

F. P. Israel, E. F. van Dishoeck, F. Baas, J. Koornneef, J. H. Black, and T. de Graauw. H2 emission and CO absorption in Centaurus A - Evidence for a circumnuclear molecular disk. *A&A*, 227:342–350, 1990.

W. Jaffe, K. Meisenheimer, H. J. A. Röttgering, C. Leinert, A. Richichi, O. Chesneau, D. Fraix-Burnet, A. Glazenborg-Kluttig, G.-L. Granato, U. Graser, B. Heijligers, R. Köhler, F. Malbet, G. K. Miley, F. Paresce, J.-W. Pel, G. Perrin, F. Przygodda, M. Schoeller, H. Sol, L. B. F. M. Waters, G. Weigelt, J. Woillez, and P. T. de Zeeuw. The central dusty torus in the active nucleus of NGC 1068. *Nature*, 429:47–49, 2004.

T. H. Jarrett, T. Chester, R. Cutri, S. E. Schneider, and J. P. Huchra. The 2MASS Large Galaxy Atlas. *AJ*, 125:525–554, 2003.

M. Karovska, M. Marengo, M. Elvis, G. G. Fazio, J. L. Hora, P. M. Hinz, W. F. Hoffmann, M. Meyer, and E. Mamajek. Spatially Resolved Circumnuclear Dust in Centaurus A. *ApJ*, 598:L91–L94, 2003.

E. Y. Khachikian and D. W. Weedman. An atlas of Seyfert galaxies. *ApJ*, 192: 581–589, 1974.

J. Kormendy and D. Richstone. Inward Bound—The Search For Supermassive Black Holes In Galactic Nuclei. *ARA&A*, 33:581, 1995.

D. Krajnović, M. Cappellari, P. T. de Zeeuw, and Y. Copin. Kinemetry: a generalization of photometry to the higher moments of the line-of-sight velocity distribution. *MNRAS*, 366:787–802, 2006a.

D. Krajnović, R. Sharp, and N. Thatte. Integral-field spectroscopy of Centaurus A nucleus. *MNRAS*, 2006b.

M. Krause. Very light jets II: Bipolar large scale simulations in King atmospheres. *A&A*, 431:45–64, 2005.

J. H. Krolik. *Active galactic nuclei : from the central black hole to the galactic environment.* Princeton University Press, 1999.

L. L. Leeuw, T. G. Hawarden, H. E. Matthews, E. I. Robson, and A. Eckart. Deep Submillimeter Imaging of Dust Structures in Centaurus A. *ApJ*, 565:131–139, 2002.

R. Lenzen, R. Hofmann, P. Bizenberger, and A. Tusche. CONICA: the high-resolution near-infrared camera for the ESO VLT. In A. M. Fowler, editor, *Proc. SPIE Vol. 3354, p. 606-614, Infrared Astronomical Instrumentation, Albert M. Fowler; Ed.*, pages 606–614, 1998.

D. Lynden-Bell. Galactic Nuclei as Collapsed Old Quasars. *Nature*, 223:690, 1969.

F. Macchetto, A. Marconi, D. J. Axon, A. Capetti, W. Sparks, and P. Crane. The Supermassive Black Hole of M87 and the Kinematics of Its Associated Gaseous Disk. *ApJ*, 489:579, 1997.

W. Maciejewski and J. Binney. Kinematics from spectroscopy with a wide slit: detecting black holes in galaxy centres. *MNRAS*, 323:831–838, 2001.

P. Madau, H. C. Ferguson, M. E. Dickinson, M. Giavalisco, C. C. Steidel, and A. Fruchter. High-redshift galaxies in the Hubble Deep Field: colour selection and star formation history to z˜4. *MNRAS*, 283:1388–1404, 1996.

D. F. Malin, P. J. Quinn, and J. A. Graham. Shell structure in NGC 5128. *ApJ*, 272:L5–L7, 1983.

A. Marconi, D. J. Axon, A. Capetti, W. Maciejewski, J. Atkinson, D. Batcheldor, J. Binney, C. M. Carollo, L. Dressel, H. Ford, J. Gerssen, M. A. Hughes, D. Macchetto, M. R. Merrifield, C. Scarlata, W. Sparks, M. Stiavelli, Z. Tsvetanov, and R. P. van der Marel. Is There Really a Black Hole at the Center of NGC 4041? Constraints from Gas Kinematics. *ApJ*, 586:868–890, 2003.

A. Marconi, A. Capetti, D. J. Axon, A. Koekemoer, D. Macchetto, and E. J. Schreier. Peering through the Dust: Evidence for a Supermassive Black Hole at the Nucleus of Centaurus A from VLT Infrared Spectroscopy. *ApJ*, 549:915–937, 2001.

A. Marconi, G. Pastorini, F. Pacini, D. J. Axon, A. Capetti, D. Macchetto, A. M. Koekemoer, and E. J. Schreier. The supermassive black hole in Centaurus A: a benchmark for gas kinematical measurements. *A&A*, 448:921–953, 2006.

A. Marconi, G. Risaliti, R. Gilli, L. K. Hunt, R. Maiolino, and M. Salvati. Local supermassive black holes, relics of active galactic nuclei and the X-ray background. *MNRAS*, 351:169–185, 2004.

A. Marconi, E. J. Schreier, A. Koekemoer, A. Capetti, D. Axon, D. Macchetto, and N. Caon. Unveiling the Active Nucleus of Centaurus A. *ApJ*, 528:276–291, 2000.

A. Mathieu and H. Dejonghe. Triaxial dynamical models of elliptical galaxies using Stackel potentials. *MNRAS*, 303:455–465, 1999.

J. S. Mathis. Interstellar dust and extinction. *ARA&A*, 28:37–70, 1990.

K. Meisenheimer, K. Tristram, W. Jaffe, D. Raban, H. Röttgering, W. D. Cotton, U. Graser, T. Henning, Ch. Leinert, B. Lopez, G. Perrin, F. Israel, N. Neumayer, A. Prieto, and L. B. F. M. Waters. Resolving the innermost parsec of Centaurus A at mid-infrared wavelengths. *A&A*, 2007.

N. Menci, A. Cavaliere, A. Fontana, E. Giallongo, F. Poli, and V. Vittorini. Quasar Evolution Driven by Galaxy Encounters in Hierarchical Structures. *ApJ*, 587: L63–L66, 2003.

I. F. Mirabel, O. Laurent, D. B. Sanders, M. Sauvage, M. Tagger, V. Charmandaris, L. Vigroux, P. Gallais, C. Cesarsky, and D. L. Block. A barred spiral at the centre of the giant elliptical radio galaxy Centaurus A. *A&A*, 341:667–674, 1999.

G. Monnet, R. Bacon, and E. Emsellem. Modelling the stellar intensity and radial velocity fields in triaxial galaxies by sums of Gaussian functions. *A&A*, 253: 366–373, 1992.

R. A. Nicholson, J. Bland-Hawthorn, and K. Taylor. The structure and dynamics of the gaseous and stellar components in Centaurus A. *ApJ*, 387:503–521, 1992.

D. E. Osterbrock and G. J. Ferland. *Astrophysics of gaseous nebulae and active galactic nuclei.* Astrophysics of gaseous nebulae and active galactic nuclei, 2nd. ed. by D.E. Osterbrock and G.J. Ferland. Sausalito, CA: University Science Books, 2006, 2006.

E. W. Peng, H. C. Ford, K. C. Freeman, and R. L. White. A Young Blue Tidal Stream in NGC 5128. *AJ*, 124:3144–3156, 2002.

M. A. Prieto and K. Meisenheimer. The parsec-scale region of active galactic nuclei in the IR. In T. Storchi-Bergmann, L. C. Ho, and H. R. Schmitt, editors, *IAU Symposium*, pages 57–60, 2004.

J. E. Pringle. Self-induced warping of accretion discs. *MNRAS*, 281:357–361, 1996.

A. C. Quillen, M. H. Brookes, J. Keene, D. Stern, C. R. Lawrence, and M. W. Werner. Spitzer Observations of the Dusty Warped Disk of Centaurus A. *ApJ*, 645:1092–1101, 2006.

A. C. Quillen, P. T. de Zeeuw, E. S. Phinney, and T. G. Phillips. The kinematics of the molecular gas in Centaurus A. *ApJ*, 391:121–136, 1992.

A. C. Quillen, J. R. Graham, and J. A. Frogel. The warped disk of Centaurus A in the near-infrared. *ApJ*, 412:550–567, 1993.

M. J. Rees. George DARWIN Lecture 1976 - Quasars and young galaxies. *QJRAS*, 18:429–442, 1977.

B. Reipurth, S. Heathcote, J. Morse, P. Hartigan, and J. Bally. Hubble Space Telescope Images of the HH 34 Jet and Bow Shock: Structure and Proper Motions. *AJ*, 123:362–381, 2002.

M. Rejkuba. The distance to the giant elliptical galaxy NGC 5128. *A&A*, 413: 903–912, 2004.

M. Rejkuba, D. Minniti, F. Courbin, and D. R. Silva. Radio-Optical Alignment and Recent Star Formation Associated with Ionized Filaments in the Halo of NGC 5128 (Centaurus A). *ApJ*, 564:688–695, 2002.

H.-W. Rix, P. T. de Zeeuw, N. Cretton, R. P. van der Marel, and C. M. Carollo. Dynamical Modeling of Velocity Profiles: The Dark Halo around the Elliptical Galaxy NGC 2434. *ApJ*, 488:702, 1997.

I. Robson. *Active galactic nuclei.* Wiley-Praxis Series in Astronomy and Astrophysics, New York, NY: Wiley, Chichester: Praxis Publishing, —c1996, 1996.

F. Roddier. Curvature sensing and compensation: a new concept in adaptive optics. *Appl. Opt.*, 27:1223–1225, 1988.

G. Rousset, F. Lacombe, P. Puget, N. N. Hubin, E. Gendron, J.-M. Conan, P. Y. Kern, P.-Y. Madec, D. Rabaud, D. Mouillet, A.-M. Lagrange, and F. J. Rigaut. Design of the Nasmyth adaptive optics system (NAOS) of the VLT. In D. Bonaccini and R. K. Tyson, editors, *Proc. SPIE Vol. 3353, p. 508-516, Adaptive Optical System Technologies, Domenico Bonaccini; Robert K. Tyson; Eds.*, pages 508–516, 1998.

D. B. Sanders and I. F. Mirabel. Luminous Infrared Galaxies. *ARA&A*, 34:749–+, 1996.

D. B. Sanders, B. T. Soifer, J. H. Elias, B. F. Madore, K. Matthews, G. Neugebauer, and N. Z. Scoville. Ultraluminous infrared galaxies and the origin of quasars. *ApJ*, 325:74–91, 1988.

D. Schiminovich, J. H. van Gorkom, J. M. van der Hulst, and S. Kasow. Discovery of Neutral Hydrogen Associated with the Diffuse Shells of NGC 5128 (Centaurus A). *ApJ*, 423:L101+, 1994.

E. Schinnerer, A. Eckart, and L. J. Tacconi. The Nuclear Stellar Cluster in the Seyfert 1 Galaxy NGC 3227: High Angular Resolution Near-Infrared Imaging and Spectroscopy. *ApJ*, 549:254–273, 2001.

M. Schmidt. 3C 273: a star-like object with large red-shift. *Nature*, 197:1040–1040, 1963.

M. Schmidt, D. P. Schneider, and J. E. Gunn. Spectrscopic CCD Surveys for Quasars at Large Redshift.IV.Evolution of the Luminosity Function from Quasars Detected by Their Lyman-Alpha Emission. *AJ*, 110:68, 1995.

R. Schödel, T. Ott, R. Genzel, R. Hofmann, M. Lehnert, A. Eckart, N. Mouawad, T. Alexander, M. J. Reid, R. Lenzen, M. Hartung, F. Lacombe, D. Rouan, E. Gendron, G. Rousset, A.-M. Lagrange, W. Brandner, N. Ageorges, C. Lidman, A. F. M. Moorwood, J. Spyromilio, N. Hubin, and K. M. Menten. A star in a 15.2-year orbit around the supermassive black hole at the centre of the Milky Way. *Nature*, 419:694–696, 2002.

R. H. M. Schoenmakers, M. Franx, and P. T. de Zeeuw. Measuring non-axisymmetry in spiral galaxies. *MNRAS*, 292:349, 1997.

E. J. Schreier, A. Capetti, F. Macchetto, W. B. Sparks, and H. J. Ford. Hubble Space Telescope Imaging and Polarimetry of NGC 5128 (Centaurus A). *ApJ*, 459:535, 1996.

E. J. Schreier, A. Marconi, D. J. Axon, N. Caon, D. Macchetto, A. Capetti, J. H. Hough, S. Young, and C. Packham. Evidence for a 20pc Disk at the Nucleus of Centaurus A. *ApJ*, 499:L143+, 1998.

N. Z. Scoville, D. B. Sanders, A. I. Sargent, B. T. Soifer, S. L. Scott, and K. Y. Lo. Millimeter interferometry of the molecular gas in ARP 20. *ApJ*, 311:L47–L50, 1986.

C. K. Seyfert. Nuclear Emission in Spiral Nebulae. *ApJ*, 97:28, 1943.

R. B. Shack and B. C. Platt. Production and use of a Lenticular Hartmann-Screen. *J. Opt. Soc. Am. A*, 61:656, 1971.

K. L. Shapiro, M. Cappellari, T. de Zeeuw, R. M. McDermid, K. Gebhardt, R. C. E. van den Bosch, and T. S. Statler. The black hole in NGC 3379: a comparison of gas and stellar dynamical mass measurements with HST and integral-field data. *MNRAS*, 370:559–579, 2006.

J. D. Silge, K. Gebhardt, M. Bergmann, and D. Richstone. Gemini Near Infrared Spectrograph Observations of the Central Supermassive Black Hole in Centaurus A. *AJ*, 130:406–417, 2005.

B. T. Soifer, G. Neugebauer, and J. R. Houck. The IRAS view of the extragalactic sky. *ARA&A*, 25:187–230, 1987.

V. Springel, T. Di Matteo, and L. Hernquist. Modelling feedback from stars and black holes in galaxy mergers. *MNRAS*, 361:776–794, 2005.

A. Stolte. Mass functions and mass segregation in young starburst clusters. *Ph.D. Thesis*, 2003.

A. Stolte, W. Brandner, E. K. Grebel, R. Lenzen, and A.-M. Lagrange. The Arches Cluster: Evidence for a Truncated Mass Function? *ApJ*, 628:L113–L117, 2005.

A. Strehl. Über Luftschlieren und Zonenfehler. *Zeitschrift für Instrumentenkunde*, 22:214, 1902.

D. Taylor, J. E. Dyson, and D. J. Axon. Bowshocks and the formation of the narrow-line region of Seyfert galaxies. *MNRAS*, 255:351–368, 1992.

S. J. Tingay, D. L. Jauncey, J. E. Reynolds, A. K. Tzioumis, E. A. King, R. A. Preston, D. L. Jones, D. W. Murphy, D. L. Meier, T. D. van Ommen, P. M. McCulloch, S. P. Ellingsen, M. E. Costa, P. G. Edwards, J. E. J. Lovell, G. D. Nicolson, J. F. H. Quick, A. J. Kemball, V. Migenes, P. Harbison, P. A. Jones, G. L. White, R. G. Gough, R. H. Ferris, M. W. Sinclair, and R. W. Clay. The Subparsec-Scale Structure and Evolution of Centaurus A: The Nearest Active Radio Galaxy. *AJ*, 115:960–974, 1998.

J. L. Tonry, A. Dressler, J. P. Blakeslee, E. A. Ajhar, A. B. Fletcher, G. A. Luppino, M. R. Metzger, and C. B. Moore. The SBF Survey of Galaxy Distances. IV. SBF Magnitudes, Colors, and Distances. *ApJ*, 546:681–693, 2001.

A. Toomre. Mergers and Some Consequences. In B. M. Tinsley and R. B. Larson, editors, *Evolution of Galaxies and Stellar Populations*, pages 401–+, 1977.

A. Toomre and J. Toomre. Galactic Bridges and Tails. *ApJ*, 178:623–666, 1972.

S. Tremaine, K. Gebhardt, R. Bender, G. Bower, A. Dressler, S. M. Faber, A. V. Filippenko, R. Green, C. Grillmair, L. C. Ho, J. Kormendy, T. R. Lauer, J. Magorrian, J. Pinkney, and D. Richstone. The Slope of the Black Hole Mass versus Velocity Dispersion Correlation. *ApJ*, 574:740–753, 2002.

S. Tremaine, D. O. Richstone, Y.-I. Byun, A. Dressler, S. M. Faber, C. Grillmair, J. Kormendy, and T. R. Lauer. A family of models for spherical stellar systems. *AJ*, 107:634–644, 1994.

C. M. Urry and P. Padovani. Unified Schemes for Radio-Loud Active Galactic Nuclei. *PASP*, 107:803, 1995.

M. Valluri, D. Merritt, and E. Emsellem. Difficulties with Recovering the Masses of Supermassive Black Holes from Stellar Kinematical Data. *ApJ*, 602:66–92, 2004.

R. P. van der Marel, P. T. de Zeeuw, and H.-W. Rix. Improved Evidence for a Black Hole in M32 from HST/FOS Spectra. I. Observations. *ApJ*, 488:119, 1997.

R. P. van der Marel and M. Franx. A new method for the identification of non-Gaussian line profiles in elliptical galaxies. *ApJ*, 407:525–539, 1993.

R. P. van der Marel and F. C. van den Bosch. Evidence for a $3 \times 10^8 M_\odot$ Black Hole in NGC 7052 from Hubble Space Telescope Observations of the Nuclear Gas Disk. *AJ*, 116:2220–2236, 1998.

G. A. Verdoes Kleijn, R. P. van der Marel, C. M. Carollo, and P. T. de Zeeuw. The Black Hole in IC 1459 from Hubble Space Telescope Observations of the Ionized Gas Disk. *AJ*, 120:1221–1237, 2000.

G. A. Verdoes Kleijn, R. P. van der Marel, P. T. de Zeeuw, J. Noel-Storr, and S. A. Baum. Gas Kinematics and the Black Hole Mass at the Center of the Radio Galaxy NGC 4335. *AJ*, 124:2524–2542, 2002.

Q. Yu and S. Tremaine. Observational constraints on growth of massive black holes. *MNRAS*, 335:965–976, 2002.

Acknowledgements

It is a pleasure to thank the people that helped in one way or another to realise this thesis:

Hans-Walter Rix who made this work possible and supported me in many ways during the past years. I am deeply grateful for his encouragement, his trust and especially his tolerance and support while I was working mainly from home during the first few months after the birth of my daughter.

Prof. Dr. Max Camenzind for being my co-referee and for interesting discussions about jets.

This work would have not been possible without the support and help of my collaborators. I would like to thank Michele Cappellari, Markus Hartung, Klaus Meisenheimer, Konrad Tristram, Chien Peng, Almudena Prieto, Juha Reunanen, Tim de Zeeuw, Paul van der Werf and Ric Davies.

I acknowledge the hospitality of the Sterrewacht in Leiden, in particular the group of Tim de Zeeuw, where parts of the analysis of this thesis have been pursued.

I am grateful for the support of the Christiane-Nüsslein-Volhard Foundation.

It is my pleasure to thank my past and present room-mates, Laura, Jakob, Jens, Johny, Boris, Marco and Jaron, for far too many things as to list them all.

I was very happy to get to know many nice people during my time as a PhD student, and some of them became true friends. Thanks!

Thanks to all colleagues at MPIA who create such a nice working environment and atmosphere.

Many thanks to the System Administrators at MPIA for their great support.

I thank the daycare “Die Wichtel” for giving me the good feeling that our daughter is in good hands.

I am grateful for the support of my friends, especially Sabine and Kathrin, for many valuable hours of ‘Johanna-sitting’.

I would like to thank my family for their encouragement and support and for simply always being there.

Thank you, Johanna, for giving me a ‘short vacation’ every evening, and for being such a wonderful person.

My dearest thanks go to my love, Dirk, for this wonderful and fulfilled life that we share.

Erklärung

Ich versichere, dass ich diese Arbeit selbständig verfasst und keine anderen als die angegebenen Quellen und Hilfsmittel benutzt habe.

Heidelberg, den ____________________

(Nadine Neumayer)